Universität Bremen

In vivo study of the role of the chaperone HSP110 in amyloid beta (Aβ) aggregation

Dissertation zur Erlangung des akademischen Grades des Doctor rerum naturalium (Dr. rer. nat.)

eingereicht im Fachbereich 02 Biologie/Chemie der Universität Bremen

vorgelegt von
Sabrina Montresor

April 2024

Reviewer 1: Prof. Dr. Janine Kirstein

Reviewer 2: Prof. Dr. Olivia Masseck

Date of defense: 19th June 2024

Table of Contents

Summary

Protein misfolding and aggregation are characteristic events in most neurodegenerative diseases. To prevent proteotoxicity, the cell has evolved a protein homeostasis (proteostasis) network comprised of molecular chaperones and proteolytic pathways. Molecular chaperones can regulate protein folding by e.g. prevention of protein aggregation, refolding of proteins and protein disaggregation. Molecular chaperones can be used as targets for pharmacological intervention against neurodegenerative diseases. HSP110 is a poorly characterised molecular chaperone and its functional spectrum is not yet fully elucidated. Nevertheless, HSP110 has recently been implicated in various neurodegenerative diseases, including Alzheimer´s disease (AD). Aggregation of the amyloid beta peptide (Aβ) is one of the hallmarks of AD. *In vitro* studies have shown that human HSP110 can inhibit $A\beta_{1-42}$ fibril formation either alone or in combination with HSC70 and a J-domain protein. However, the beneficial versus detrimental implications of HSP110 in neurodegenerative physiological contexts are still under debate.

Therefore, I investigated the effect of HSP-110 and its interplay with $A\beta_{1-42}$ *in vivo* using *C. elegans* as a model organism. I generated a novel *C. elegans* model that overexpressed *hsp-110* pan-neuronally and I also depleted *hsp-110* by RNAi-mediated knockdown. I analyzed the role of HSP-110 in $A\beta_{1-42}$ aggregation using a pan-neuronal Aβ *C. elegans* model. In addition, I performed transcriptomic and proteomic analyses of pan-neuronal and muscular Aβ *C. elegans* strains to reveal global changes in gene expression and protein levels in these AD models. I could show that *hsp-110* overexpression exacerbated $A\beta_{1-42}$ aggregation *in vivo*. Conversely, *hsp-110* depletion reduced $A\beta_{1-42}$ aggregation significantly in the IL2 neurons, which mark the onset of $A\beta_{1-42}$ aggregation in *C. elegans.* Moreover, HSP-110 is a modulator of the autophagy pathway, with overexpression of *hsp-110* impairing and depletion of *hsp-110* inducing autophagy. HSP-110 appears to regulate multiple nodes of the proteostasis network and further studies are necessary to fully unravel the effect on $A\beta_{1-42}$. In addition, I gained a preliminary understanding of the biological changes associated with $A\beta_{1-42}$ aggregation in *C. elegans* using transcriptomic and proteomic analyses. Surprisingly, of the molecular chaperones, only small HSPs showed an increased abundance.

Zusammenfassung

Proteinfehlfaltung und -aggregation sind charakteristisch für die meisten neurodegenerativen Erkrankungen. Um Proteotoxizität zu verhindern, hat die Zelle ein Netzwerk zur Proteinhomöostase (Proteostase) entwickelt, das aus molekularen Chaperonen und proteolytischen Systemen besteht. Molekulare Chaperone können die Proteinaggregation durch verschiedene Aktivitäten modulieren wie beispielsweise durch die Unterdrückung der Proteinaggregation, der Rückfaltung von Proteinen oder der Proteindisaggregation. Molekulare Chaperone könnten als Zielmoleküle für pharmakologische Therapien gegen neurodegenerative Erkrankungen genutzt werden. HSP110 ist ein bisher noch wenig charakterisiertes molekulares Chaperon, und sein Funktionsspektrum ist noch nicht vollständig geklärt. Dennoch wurde HSP110 mit verschiedenen neurodegenerativen Erkrankungen in Verbindung gebracht, darunter auch mit der Alzheimer Erkrankung. Die Aggregation des Amyloid-Beta-Peptids (Aβ) ist eines der Charakteristika der Alzheimer Erkrankung. *In vitro*-Studien haben gezeigt, dass humanes HSP110 die Bildung von $A\beta_{1-42}$-Fibrillen entweder allein oder in Kombination mit HSC70- und J-Domänen-Proteinen unterdrücken kann. Die positiven als auch negativen Effekte von HSP110 in der Pathophysiologie von neurodegenerativen Erkrankungen werden jedoch noch diskutiert.

Daher untersuchte ich die Wirkung von HSP-110 und sein Zusammenspiel mit $A\beta_{1-42}$ *in vivo* mit *C. elegans* als Modellorganismus. Ich habe ein neues *C. elegans*-Modell entwickelt, in dem *hsp-110* pan-neuronal überexprimiert wird und ich habe mittels RNAi die *hsp-110* Expression unterdrückt. Mit beiden Strategien analysierte ich die Rolle von *hsp-110* auf die $A\beta_{1-42}$-Aggregation unter Verwendung eines pan-neuronalen Aβ-*C. elegans*-Modells. Parallel dazu habe ich transkriptomische und proteomische Analysen von Aβ-*C. elegans*-Stämmen durchgeführt, um die durch $A\beta_{1-42}$ induzierten globalen Veränderungen auf die Genexpression und den Proteingehalt zu untersuchen. Ich konnte zeigen, dass eine Überexpression von *hsp-110* die $A\beta_{1-42}$-Aggregation *in vivo* verstärkt. Eine Depletion von *hsp-110* reduzierte die $A\beta_{1-42}$ Aggregation in den IL2-Neuronen, die den Beginn der Aβ-Aggregation in *C. elegans* markieren. HSP-110 moduliert auch die Autophagie, wobei eine Überexpression von *hsp-110* die Autophagie beeinträchtig und eine *hsp-110* Depletion die Autophagie aktiviert. HSP-110 scheint daher mehrere Kontrollpunkte des Proteostase-Netzwerks

zu regulieren, und weitere Studien sind erforderlich, um die Auswirkungen auf $A\beta_{1-42}$ vollständig zu entschlüsseln. Darüber hinaus konnte ich ein mit Transkriptom- und Proteomstudien zeigen, dass von den molekularen Chaperonen nur die kleinen Hitzeschockproteine in $A\beta_{1-42}$ Modellen induziert werden.

Authorship Disclaimer

The work presented here was performed under the supervision of Prof. Dr. Janine Kirstein and within her group at the University of Bremen.
Parts of the presented projects were conducted in collaboration with colleagues from my working group or collaborators from other research institutes. The contribution of my colleagues and external collaborators has been mentioned in the results section and is also reported below.

Dr. Maria Lucia Pigazzini injected the plasmid pPD95_77::*rgef-1p::hsp-110::gfp* into N2 wildtype *C. elegans*. Sudarson Baskaran performed one biological replicate of the N2 wild type lifespan. Mira Sleiman performed one biological replicate of nAβ *eri-1* control RNAi lifespan
Govinda Adhikari performed two biological replicates of *n hsp-110 I* progeny and two biological replicates of nmScarlet *n hsp-110 I* progeny. The Sawarkar lab (MPI Freiburg & Cambridge University, UK) performed the RNA sequencing and the bioinformatic analysis for the transcriptomic study of nAβ and mAβ *C. elegans* strains. The Savitski lab (EMBL, Heidelberg) performed the protein extraction, mass spectrometry and the bioinformatic analysis for the proteomic study of nAβ and mAβ *C. elegans* strains.

Portions of the text resemble or may replicate the original text of my submitted manuscript entitled “HSP110 is a modulator of amyloid beta (Aβ) aggregation and proteotoxicity “, which is currently under revision.

Furthermore, I would also like to mention the B.Sc. and M.Sc students who contributed to some of the experiments presented in this work as assistants. Lukas Basilicata, Luca Secker, Natascha Jacob, Yara Ehlert, Anushree Kelkar, Gurleen Kaur Kalsi, Niraj Kulkarni, Shatakshi Morchhale, Tom Daniel, Philip Zimmer and Paul Spellerberg contributed with some lifespan, progeny and western blot experiments.

1 Introduction

Proteinopathies are diseases associated with abnormal protein conformations. For most proteins, the acquisition of a native conformation is essential for the biological function. When proteins adopt non-native structures, they can lose their physiological function and / or gain a potentially anomalous function and could become prone to aggregation. Neurodegenerative diseases, such Alzheimer´s disease (AD), are characterized by protein misfolding and aggregation in the brain, and therefore considered proteinopathies. Neurodegenerative diseases are a major burden for society and understanding the underlying molecular mechanisms and their pathophysiology is important for the development of early diagnostic tools and therapeutic interventions (Sweeney et al., 2017).

1.1 Alzheimer´s disease

Alzheimer´s disease is a devastating neurodegenerative disorder primarily affecting the brain. It is defined by the accumulation of amyloid plaques and neurofibrillary tangles (NFTs). Progressive neuronal and synapse degeneration induce brain atrophy and lead to cognitive dysfunctions, with memory loss being the most common symptom (Knopman et al., 2021). Ultimately, death occurs eight to ten years after diagnosis (Brookmeyer et al., 2002). Although the disease has been known for over a hundred years, the exact molecular mechanism underlying neuronal cell death has not been fully elucidated. Alzheimer´s disease is the most common cause of dementia, accounting for 60-70% of all cases. According to the World Health Organization (WHO), dementia affects over 55 million people worldwide and the incidence is expected to rise to 139 million by 2050. In Europe, about 10 million people are estimated to suffer from dementia and the number is predicted to double by 2050. The major risk factor for AD is aging and the number of AD patients is expected to rise due to the longer life expectancy. The increasing incidence and the lack of effective treatments pose a heavy economic burden on the healthcare system and society. Therefore, a better understanding of the causes and underlying mechanism are vital for developing treatments (World Alzheimer Report 2023; Nasreddine et al. 2023).

It was in 1907 that the psychiatrist and neuropathologist Alois Alzheimer reported for the first time the pathological features of this disease by analysing the post-mortem brain of the patient Auguste Deter. Alois Alzheimer observed brain atrophy and identified two main pathological alterations, later referred to as amyloid plaques and NFTs (Alzheimer 1907). While amyloid plaques are located in the extracellular space and consist of aggregated amyloid beta peptide (Aβ), NFTs are intraneuronal and are constituted of aggregated and abnormally hyperphosphorylated Tau protein (Glenner and Wong, 1984; Kosik et al., 1986). Interestingly, protein aggregation is a feature shared by many other neurodegenerative diseases such as Huntington's disease (HD), Parkinson´s disease (PD) and Amyotrophic lateral sclerosis (ALS) with respectively aggregation of mutant huntingtin (HTT), α-synuclein (α-syn) and superoxide dismutase 1 (SOD1) (Ross and Poirier, 2004). Alzheimer´s disease can be classified into two groups, a familiar early-onset and a sporadic late-onset. The familiar early-onset type is a rare condition accounting for less than 5% of all AD cases. It is caused by genetic mutations of genes encoding for the amyloid precursor protein (APP), presenilin 1 (PSEN1) and presenilin 2 (PSEN2) that are predominantly responsible for this form. Symptoms manifest in individuals younger than 65 years old. Conversely, the sporadic late-onset type accounts for the majority of all cases (> 95%) and it is most common in individuals older than 65 years. More than 600 gene variants have been associated with elevated risk of developing late-onset AD, that are however not considered causative of the disease. For instance, variants of the apolipoprotein E (APOE) gene, involved in lipid transport, is the strongest genetic risk factor identified (Hashimoto et al., 2012; Raulin et al., 2022). The late-onset form is considered a multifactorial disease, caused by a combination of genetic and environmental factors and several risk factors have been associated with it. Age is the most important risk factor identified and after the age of 65, the risk of developing AD doubles every five years. Additionally, medical conditions as diabetes, heart diseases and depression contribute to higher risk. Furthermore, lifestyle factors such as unhealthy diet, physical inactivity, obesity, smoking and air pollution also increase the risk. Gender has also been observed to play a crucial role, with women twice as likely to develop AD compared to men, but the reason is still unknown. Although the early-onset and the late-onset forms have different causes and prevalence, they share the same pathological and clinical features (Knopman et al. 2021; Hampel et al. 2021; World Alzheimer Report 2023).

1.1.1 The amyloid beta (Aβ) peptide

Several theories have emerged to explain AD etiology and the best known is the amyloid beta hypothesis. This theory proposes that Aβ deposition is the causative agent of AD and triggers a cascade of pathological events including Tau accumulation and neuronal death (Hardy J. and Higgins G., 1992). The identification of mutations in APP, PSEN1 and PSEN2 genes in early-onset AD supported this theory. Besides the amyloid cascade, alternative theories have been proposed such as the oxidative hypothesis, the glutamatergic and the cholinergic hypotheses among others (Hampel et al., 2021, 2019; Liu et al., 2019; Maragos et al., 1987). All these theories are still under debate as the etiology of late onset AD remains unclear.

The Aβ peptide is generated by the cleavage of the APP precursor, a transmembrane protein enriched in neurons and particularly at the synaptic level. Studies in mice suggested neuronal and synaptic functions for APP, but the physiological role is still not well understood (Müller et al., 2017). APP is cleaved by proteases in an amyloidogenic (Fig. 1.1 a) or in a non-amyloidogenic pathway (Fig. 1.1 b). In the amyloidogenic pathway, APP is sequentially cleaved by the β-secretase (e.g. BACE1) and the γ-secretase (PSEN1 and PSEN2 are components of the γ-secretase complex) leading to Aβ production. Aβ is a small 4 kDa peptide that occurs in different lengths, the most abundant is $Aβ_{1-40}$ (Fig. 1.1 c). Despite being less abundant, the $Aβ_{1-42}$ aggregates faster and is the major species in amyloid plaques (LaFerla et al., 2007; Tan and Gleeson, 2019). Soluble monomeric Aβ has been considered to possess biological functions, indeed picomolar concentrations of this peptide is found also in healthy brain (Brothers et al., 2018; Puzzo et al., 2008). A dysregulation between production and clearance of Aβ may trigger its deposition in the brain of AD patients. Alternatively, APP is processed in a non-amyloidogenic pathway by α- and γ-secretases and does not generate Aβ (Hampel et al., 2021).

Although amyloid plaques are found in the extracellular space, evidence from post-mortem AD human brains and murine models have suggested that Aβ accumulates also within neurons (Gouras et al., 2000; Wirths et al., 2001). Interestingly, $Aβ_{1-42}$ is more abundant than $Aβ_{1-40}$ in the intracellular space and $Aβ_{1-42}$ accumulates intraneuronally before the appearance of senile plaques, suggesting that it might be an early event in AD pathology (LaFerla et al., 2007). It is still debated whether intracellular Aβ derives from reuptake from the extracellular pool or is produced

intracellularly by e.g. a failure of the secretory pathway (Nilsson et al., 2013). Most likely it is a combination of the two mechanisms. Indeed, Aβ can interact with various molecules and potential re-uptake transporters have been identified (e.g. nicotinic acetylcholine receptor, lipoprotein receptor). At the same time, APP localizes not only in the plasma membrane but also in the Golgi, endoplasmic reticulum (ER), mitochondria, lysosome and endosome. Therefore, based on APP localization and processing, Aβ could be released intra or extracellularly (LaFerla et al., 2007).

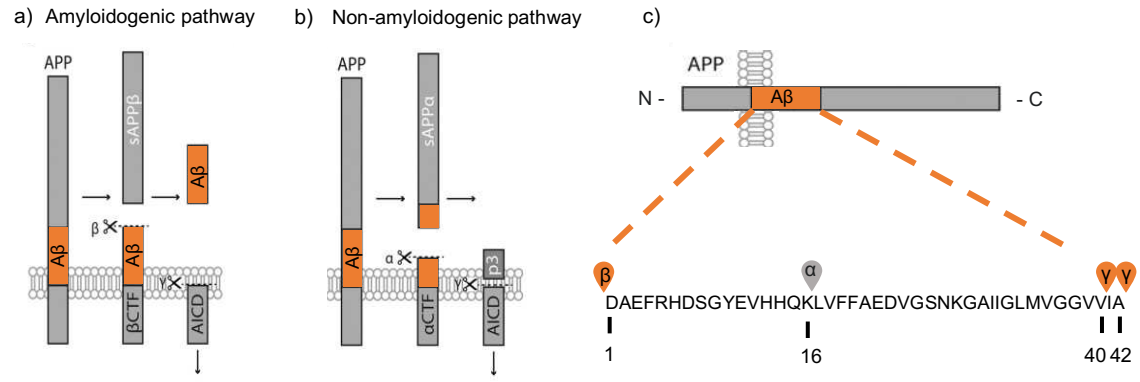

Figure 1. 1: Schematic representation of the cleavage of APP

a) APP is a large transmembrane protein that generates the Aβ peptide (orange) by the amyloidogenic pathway. The sequential endoproteolytic cleavage by the β and γ-secretases generates the Aβ peptide, the APP intracellular domain (AICD) and the soluble APP β protein (sAPPβ). Figure adapted from (Bergström et al., 2016).

b) The amyloid precursor protein can be processed in a non-amyloidogenic pathway through the α- and γ-secretases cleavage. This pathway generates the AICD, the p3 and the soluble APP α protein (sAPPα) fragments. The Aβ peptide (orange) is not produced because the α-secretase cleaves within the Aβ sequence. Figure adapted from (Bergström et al., 2016).

c) The Aβ sequence and the cleavage sites of α-, β-, and γ-secretases are displayed. The most common peptides found in the plaques are $Aβ_{1-40}$ and $Aβ_{1-42}$. Figure adapted from (Tan and Gleeson, 2019).

The aggregation of Aβ into amyloid plaques is one of the hallmarks of AD together with the accumulation of hyperphosphorylated Tau into NFTs. Tau is a microtubule-associated protein involved in microtubule stability. In pathological conditions, Tau is hyperphosphorylated and detaches from microtubules, thus impairing microtubule stability and inducing Tau aggregation (Ballatore et al., 2007). Additional pathological

alterations identified in AD brains are oxidative damage, mitochondrial dysfunction and inflammation (Hampel et al., 2021; Zhang et al., 2023).

1.1.2 Amyloid beta fibrilization

The exact Aβ fibrilization pathway remains elusive and two mechanisms have been proposed for fibril formation: the conformational conversion (Fu et al., 2015) and the nucleated polymerization (Cohen et al., 2013).

According to the conformational conversion mechanism, Aβ spontaneously aggregates into various intermediate assemblies ultimately leading to amyloid fibril formation (Fig. 1.2 a). Monomeric Aβ can aggregate into globular oligomeric species, which are defined as the smallest aggregates. Oligomers are soluble and remain in solution even after high-speed centrifugation (Chen et al., 2017; Hampel et al., 2021). The structure of oligomers is not well defined but the preparation of oligomers *in vitro* suggested the presence of β-sheets (Yu et al., 2009). Oligomers are heterogenous low molecular weight assemblies, ranging from dimers to dodecamers (Hampel et al., 2021). Protofibrils are additional intermediate species characterized by a higher molecular weight. They are still soluble and eventually convert into insoluble amyloid fibrils (Walsh et al., 1997).

Based on the second mechanism, the fibrilization is a nucleation-dependent process represented by a sigmoidal kinetic (Fig. 1.2 b). The initial lag phase indicates the primary nucleation events, which consist in the formation of a nucleus (or seed) from monomers. A nucleus is the smallest aggregate where the addition, rather than the loss, of a monomer unit is energetically favoured. Nuclei are the building blocks for fibril elongation. Therefore, once formed, the fibril growth can be detected as an exponential fibril elongation phase. When the final plateau is reached, fibril growth and disassembly are in equilibrium. Additionally, a nucleus can also be generated by secondary nucleation on the surface of already formed fibrils. Fibrils can undergo also depolymerization and fragmentation events. Fragmentation is also considered a secondary nucleation process, as the released fragments can be seeds for further aggregation. Secondary nucleation shortens the initial lag phase and accelerate fibrilization (Cohen et al., 2013; Linse, 2019; Törnquist et al., 2018).

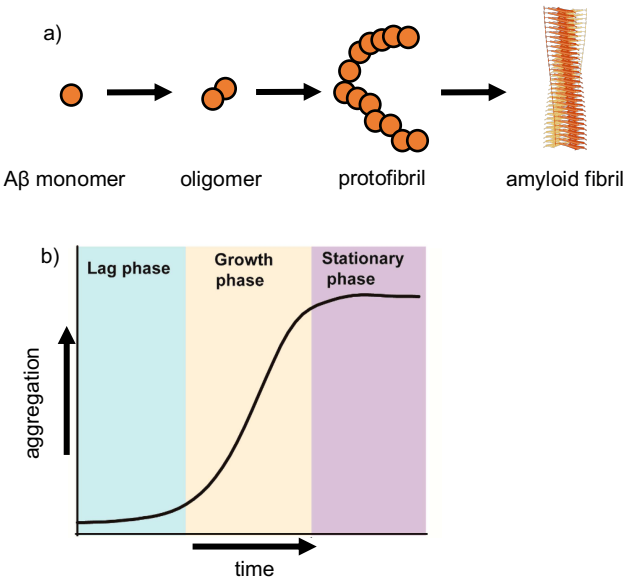

Figure 1. 2: Aβ fibrilization

a) Aβ aggregates into insoluble highly organized amyloid fibrils that exhibit cross-β structure, during fibrilization various conformational aggregates are generated (e.g. oligomers and protofibrils). Figure generated with BioRender.

b) The kinetic of Aβ aggregation is divided into three stages: a lag phase for nuclei assembly, a growth phase in which fibrils elongate and a stationary phase. Figure from (Huang and Liu, 2020).

Amyloid fibrils are insoluble, highly stable and ordered filamentous structures that assemble into a characteristic cross-β sheet pattern (Antzutkin et al., 2002). The structure of $Aβ_{1-42}$ fibrils generated *in vitro* and *ex vivo* have been solved by cryo-electron microscopy (cryo-EM) (Gremer et al., 2017; Yang et al., 2022). These studies revealed that fibrils were predominantly composed of two S-shape protofilaments intertwining around each other. $Aβ_{1-42}$ fibrils extracted from post-mortem brain of late-onset AD patients, showed that five β-strands in each protofilament are oriented perpendicular to the fibril axis. The core of the fibril spans between residues 9-42 and the β-strands stack on top of each other along the fibril axis.

The extension of amyloid plaques does not correlate well with disease pathology. An increasing number of publications suggest that oligomers are the toxic species leading to neurodegeneration (Haass & Selkoe 2007; Chen et al. 2017; Zhang et al. 2023). For instance, Aβ oligomers have shown to interact with membranes and damage their integrity (Yasumoto et al., 2019), impair synaptic plasticity (Shankar et al., 2008;

Townsend et al., 2006), affect signalling pathways (Lambert et al., 1998) and induce mitochondrial dysfunctions (X. Wang et al., 2009). Additionally, oligomers are soluble and could propagate more easily and spread faster to affect the whole brain.

1.1.3 Alzheimer´s disease staging

It is postulated that AD progresses along a continuum between three stages: preclinical, mild cognitive impairment and dementia (Jack et al., 2018) (Fig. 1.3). Preclinical AD begins decades before the onset of the first symptoms. Individuals show normal cognitive functions but already accumulate Aβ and hyperphosphorylated Tau. Abnormal Aβ deposition is considered the earliest biomarker, suggesting that Aβ plays a central and upstream role in AD. Later in this phase, signs of neurodegeneration become also evident. This stage is considered the most promising for therapeutic intervention (Jack et al., 2018; Sperling et al., 2011). The mild cognitive impairment (MCI) phase is characterized by brain structure alteration and decline in cognitive functions, with the onset of early clinical symptoms. Individuals experience memory lapses, difficulties in finding the right words or in making judgment, however these impairments do not interfere significantly with daily activities (Albert et al., 2011). AD progresses to the dementia stage, which is further subdivided into mild, moderate and severe dementia. Cognitive decline is characterized by a significant impairment in memory, language, thinking and behavioural changes affecting independence and daily tasks. In the severe dementia, patients become bed-bound and show reduction in communication abilities (McKhann et al. 2011; 2023 Alzheimer´s association report).

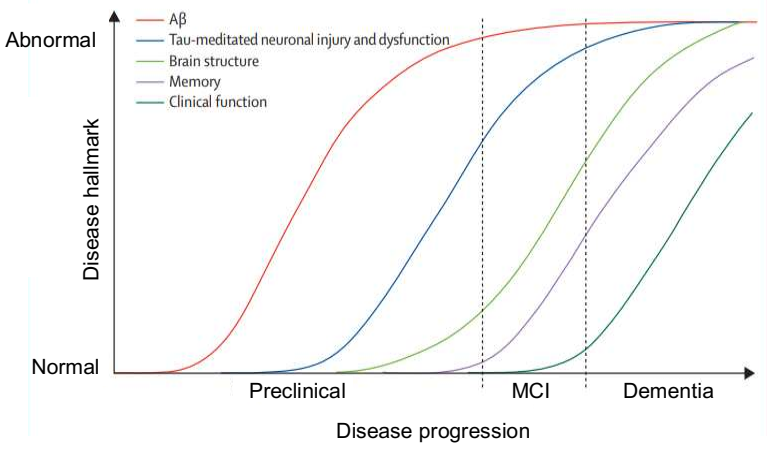

Figure 1. 3: Alzheimer´s disease continuum

Alzheimer´s disease is divided into preclinical, mild cognitive impairment (MCI) and dementia stages. During AD progression, pathological alterations become evident over time. Aβ plaques and Tau tangles are pathological hallmarks of AD and both are required for AD diagnosis. However, Aβ deposition is considered the earliest event and occurs before Tau accumulation. In the preclinical phase, AD patients have still normal cognitive abilities, but deposition of Aβ and Tau as well as signs of neurodegeneration appear. In the mild cognitive impairment (MCI), neurodegeneration and brain atrophy induce the onset of early signs of cognitive dysfunction (e.g. loss of episodic memory) but do not affect daily life activities. In the dementia stage, severe neurodegeneration progresses leading to significant cognitive impairment (e.g. memory loss) affecting daily life and independence. Figure adapted from (Jack et al. 2010).

1.2 *C. elegans* as a model organism

Caenorhabditis elegans (*C. elegans*) is a small free-living nematode found in the soil. Introduced as a model organism by Sidney Brenner in 1974 (Brenner, 1974), *C. elegans* has now been used for fifty years as an *in vivo* model in research including developmental biology, genetics, neuroscience and aging studies. *C. elegans* has the advantage of being a multicellular eukaryotic organism and at the same time anatomically simple. The nematode is composed of about a thousand cells that communicate with each other and that form multiple tissues (e.g. reproductive system, intestine, muscles, nervous system). *C. elegans* exists in two sexes, hermaphrodites (99.9% of the population) and males (0.1%). The hermaphrodites consist of 959 somatic cells and reproduce by self-fertilization, generating offspring that are homozygous and genetically identical to the original nematode (F0). Males have 1031 somatic cells and possess a characteristic fan-shape tail that allows them to mate with a hermaphrodite. Males are essential for genetic crossings, when different genotypes need to be combined (Altun and Hall, 2006).

Other practical advantages on the use of *C. elegans* in research is the easy and inexpensive cultivation. Animals are grown on NGM agar plates or in liquid culture feeding on non-pathogenic *E. coli* bacteria. A hermaphrodite can produce a large number of offspring by self-fertilization (about 300 embryos) and it takes approximatively 3.5 days for an embryo to develop into an adult nematode when kept at 20°C. The life cycle is short and consists of four larval stages (L1, L2, L3 and L4). Interestingly, L1 larvae can be cryogenically preserved enabling long and easy storage of *C. elegans* strains in liquid nitrogen for decades. Nematodes have become attractive for aging research because they have a short lifespan of about three weeks and they

exhibit alteration over the course of life that are associated to aging (e.g. reduction in motility, inhibition of reproduction, tissue degeneration) (Mack et al., 2018).
C. elegans was also the first multicellular organism whose genome was fully sequenced in 1998 (C. elegans Sequencing Consortium, 1998). It possesses five autosomes (I, II, III, IV, V) and one sex chromosome (XX for hermaphrodites and XO for males). Importantly, about 80% of the *C. elegans* proteome has homologs in human and only 11% is nematode-specific (Henricson et al., 2004; Lai et al., 2000).
Between 60-80% of human proteins have homologs in *C. elegans* and many signalling pathways are conserved (i.e. the insulin signalling pathway), thus this organism is used to study human gene function and human diseases (Y. Kim et al., 2018). *C. elegans* can be easily genetically manipulated. Nematodes are small (about 1 mm long) and their transparent body make them suitable for microscopy, for instance fluorescence proteins can be used to monitor protein expression, localization and aggregation in living nematodes. The nematode offers great potential also in neuroscience as it possesses a simple yet powerful nervous system composed of 302 neurons (and 56 glial cells). Neurons have fixed positions and the connection among them (connectome) is well known. The nervous system innervates the body wall muscles enabling nematode movement. Neurons are also responsible for moving towards odorant and food, repulsion from unfavourable conditions and pathogenic bacteria or response to touch (Corsi, 2006).

1.2.1 The novel $A\beta_{1-42}$ *C. elegans* model

C. elegans is a well-established experimental model to study neurodegenerative disorders such as Parkinson´s disease, Huntington's disease and Alzheimer's disease. *C. elegans* lacks genes that encode for the β-secretase, but expresses the *apl-1* gene, a homolog of the human APP. However, this gene does not contain the Aβ domain. Therefore, research has focused primarily on the transgenic expression of human Aβ (Caldwell et al., 2020; Markaki and Tavernarakis, 2010). The first Aβ nematode model to study Alzheimer´s disease was developed in 1995 and overexpressed only a truncated Aβ version in body wall muscles (Link, 1995). It became clear that the full $A\beta_{1-42}$ sequence was more toxic and induced more severe phenotypes. Additionally, labelling Aβ with a GFP fluorescent protein impaired Aβ fibrilization. To overcome these limitations, the Kirstein lab developed a novel Aβ model in which the toxic $A\beta_{1-42}$ is sub-

stoichiometric labelled with the mScarlet fluorescent protein, allowing simultaneous $A\beta_{1-42}$ fibrilization and visualization (Gallrein et al., 2021) (Fig. 1.4 a). $A\beta_{1-42}$ is expressed pan-neuronally using the *rgef-1* promoter (Fig. 1.4 b) or in the body wall muscles using the *myo-3* promoter (Fig. 1.4 c). These two models exhibited organismal defects such as short lifespan, reduced fertility and paralysis. Importantly, $A\beta_{1-42}$ aggregation increases with aging and can be monitored *in vivo* by fluorescence lifetime imaging microscopy (FLIM). This study also discovered that neuronal $A\beta_{1-42}$ aggregation starts in a specific subset of neurons, the IL2 neurons, located in the anterior head ganglion and that neuronal $A\beta_{1-42}$ exhibits neurological defects and neurodegeneration. The neuronal $A\beta_{1-42}$ strain (JKM2 strain) is referred in this work as nAβ, while the muscle $A\beta_{1-42}$ AD model (JKM7 strain) is referred to as mAβ.

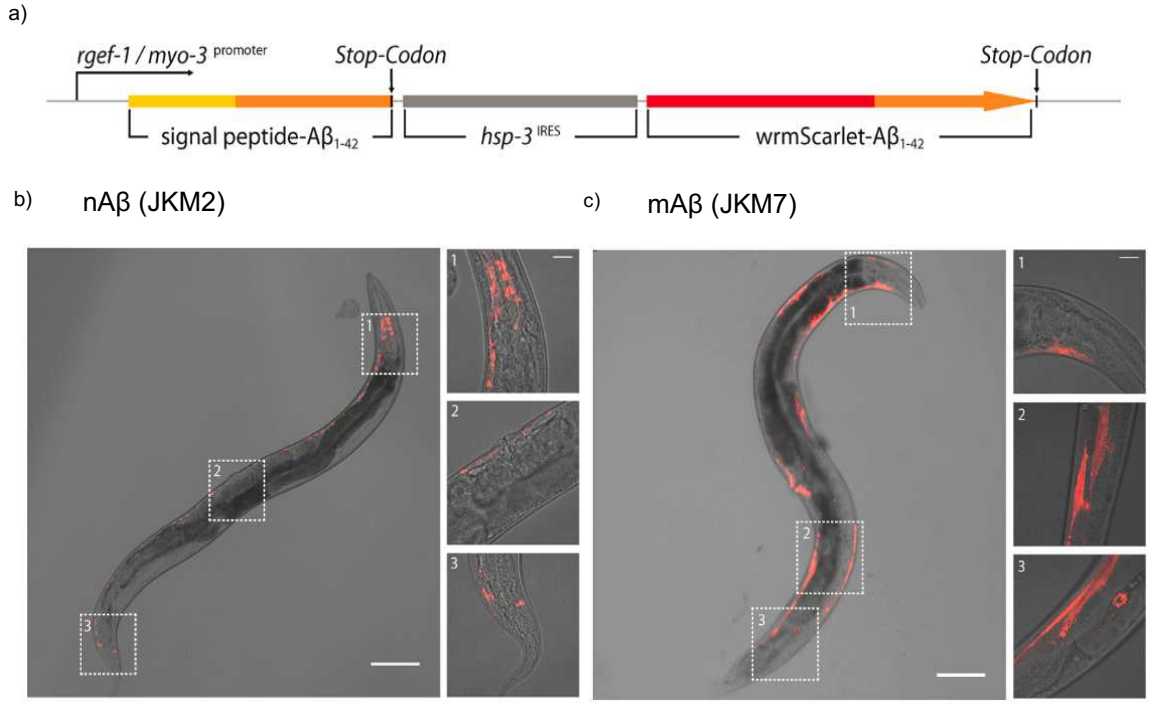

Figure 1. 4: The novel $A\beta_{1-42}$ models in *C. elegans*

a) Schematic representation of the sub-stoichiometric labelling of Aβ. The operon enables the expression of the human $A\beta_{1-42}$ pan-neuronally using the *rgef-1* promoter or in body wall muscles using the *myo-3* promoter. The $A\beta_{1-42}$ is directed to the secretory pathway via the signal peptide. The unlabelled $A\beta_{1-42}$ is expressed more efficiently following a cap-dependent translation. Conversely, the labelled mScarlet-$A\beta_{1-42}$ is translated less efficiently by the internal ribosome entry side (IRES). This ensures an excess of unlabelled $A\beta_{1-42}$ over the mScarlet-$A\beta_{1-42}$. Figure obtained from (Gallrein et al., 2021).

b) Representative confocal images of the neuronal $A\beta_{1-42}$ *C. elegans* strain. This strain expressed $A\beta_{1-42}$ pan-neuronally (nAβ) and the image is 100-fold magnified. Scale bar is 50 µm. The insets show the close-ups of 1) head, 2) mid body and 3) tail and are 630-fold magnified with a scale bar of 20 µm. Figure obtained from (Gallrein et al., 2021).

c) Representative confocal images of the muscle $A\beta_{1-42}$ *C. elegans* strain. This strain expressed $A\beta_{1-42}$ in the body wall muscles (mAβ) and the image is 100-fold magnified. Scale bar is 50 µm. The insets show the close-ups of 1) head, 2) mid body and 3) tail and are 630-fold magnified with a scale bar of 20 µm. Figure obtained from (Gallrein et al., 2021).

1.3 The proteostasis network

Proteins are essential molecules for the cell and perform a wide range of biological functions. Typically, a protein is synthetized from an mRNA as a linear polypeptide chain, that folds into a specific native conformation. Acquiring the native structure is critical for proteins to fulfil their biological functions, thus maintaining cellular and organismal health. Although folding is determined by the amino acid sequence, only a small fraction of proteins can spontaneously fold into the correct conformation. Proteins can inevitably adopt also non-functional structures. Unfolded and misfolded proteins expose hydrophobic regions, which can result in aggregates formation. These off-pathway reactions are favoured by endogenous or exogenous stressors, such as genetic mutations, transcriptional or translational errors, molecular crowding, elevated temperature and aging (Hartl et al., 2011; Hipp et al., 2019). Aberrant protein conformations are proposed to cause toxicity through loss and / or gain of function (Winklhofer et al., 2008). Loss of function results from a decrease of the functionally active protein pool whereas gain of function derives from novel toxic functionality exhibited by misfolded and aggregated proteins (e.g. toxic interactions, membrane damage). Protein misfolding and aggregation are prominent features in numerous diseases (Soto, 2003).

To maintain protein homeostasis and prevent proteotoxicity, the cell has evolved a network of protein quality control mechanisms that is referred to as the proteostasis network (PN) (Balch et al., 2008) (Fig.1.5). The PN is highly conserved and is composed of molecular chaperones and components of the protein degradation pathways (i.e. ubiquitin-proteasome system and lysosomal-autophagy pathway). It preserves proteome integrity by assisting protein synthesis and folding, maintaining protein conformational stability and ensuring correct protein turnover (Hipp et al.,

2019). It is a complex and coordinated network composed of about 2000 proteins in human cells (Klaips et al., 2018).

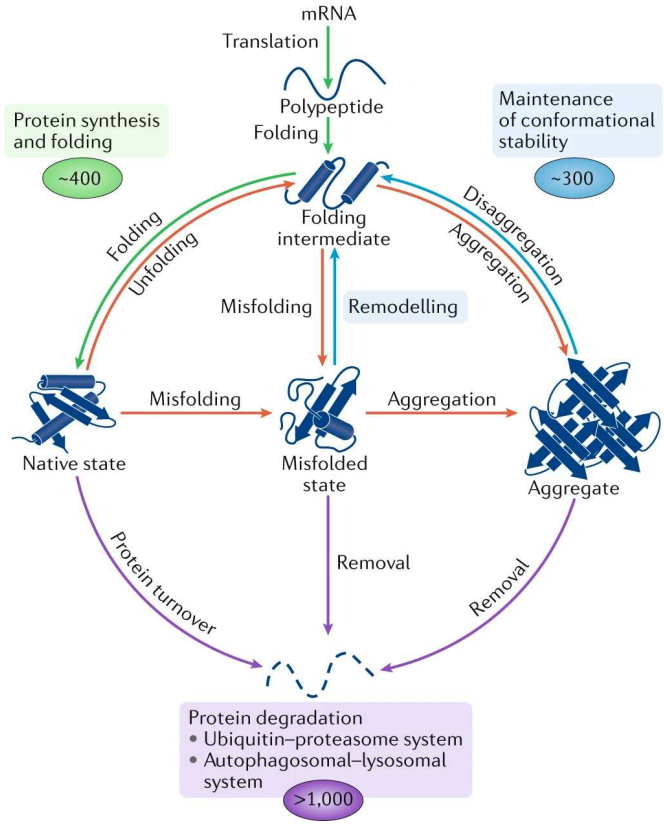

Figure 1. 5: Overview of the proteostasis network

Proteins can adopt a native functional state by folding (green). Proteins can also undergo off-pathway reactions (red) that generate non-native conformations through unfolding, misfolding and aggregation. The proteostasis network maintains the integrity of the proteome by assisting protein folding, refolding, disaggregation and degradation. Image from (Hipp et al. 2019).

The proteostasis capacity declines with aging and the amount of non-native folded proteins increases (Ben-Zvi et al., 2009). Protein aggregates in turn can sequester PN components, further compromising the proteostasis capacity and ultimately leading to proteostasis collapse (Hipp et al., 2019; Taylor and Dillin, 2011). Numerous age-related disorders are characterized by protein misfolding and aggregation, including neurodegenerative diseases (e.g. Alzheimer´s, Parkinson´s and Huntingtin's) (Soto, 2003). Neurons are particularly vulnerable to protein accumulation due to their post-mitotic nature. To prevent aggregation and proteotoxicity, PN components have been

investigated as potential targets for pharmacological intervention (Djajadikerta et al., 2020; Gong et al., 2016; Kampinga and Bergink, 2016).

The ubiquitin-proteasome system (UPS) and the lysosomal-autophagy pathway are two degradation mechanisms of the PN within eukaryotic cells. The UPS is the main cellular degradation pathway for unfolded and misfolded proteins. It is ATP-dependent and predominantly degrades single proteins rather than aggregates or large protein complexes (Pohl and Dikic, 2019). Proteins that are destined for their UPS-mediated turnover are first ubiquitinated by E1, E2 and E3 ligase and then degraded by the 26S proteasome. The proteasome is a large complex that recognizes polyubiquitylation, as a degradation signal, and targets the proteins to the inner core where they are proteolytically cleaved after unfolding (Ciechanover and Brundin, 2003; Dikic, 2017; Papaevgeniou and Chondrogianni, 2014). The lysosomal-autophagy pathway degrades larger structures such as protein complexes, protein aggregates, pathogens and cellular organelles. There are different types of autophagy, defined as macroautophagy, microautophagy and chaperone-mediated autophagy. The dominating autophagy pathway is macroautophagy (hereafter referred to as autophagy). Autophagy is initiated by the formation of the phagophore, a double membrane structure, that progressively closes around the autophagic cargo, forming an autophagosome. The human LC3 protein (LGG-1 in *C. elegans*) is anchored to the phagophore membrane after lipidation with phosphatidylethanolamine (PE). LC3 promotes membrane extension for autophagosome formation, therefore, it is considered an autophagosome marker. LC3 also recruits autophagic receptors (also known as adaptor proteins). Although autophagy has been considered a non-selective mechanism, autophagic receptors have recently been identified for cargo selection such as p62/SQSTM1, NBR1, NDP52, and OPTN. It is suggested that half of the selective autophagy depends on the ubiquitin signal for autophagy degradation (Pohl and Dikic, 2019). That p62/SQSTM1 is considered one of the receptors for aggregation prone proteins and was shown to be associated to mutant HTT in Huntington's disease and mutant SOD1 in Amyotrophic lateral sclerosis (Bjørkøy et al., 2005; Goode et al., 2016; Menzies et al., 2015). Autophagy proceeds with lysosomes, containing a multitude of proteases and other enzymes, fusing with the autophagosome to generate an autophagolysosome. The proteases then degrade the cargo, and eventually the autophagic receptors, releasing the degraded products into the cytosol (Menzies et al.,

2015; Vilchez et al., 2014). It was shown that autophagy degrades neurodegenerative associated protein aggregates (e.g. Tau, polyQ, α-syn and Aβ) and *in vivo* evidence suggested that induction of autophagy could ameliorate proteotoxic stress. (Djajadikerta et al., 2020; Ravikumar et al., 2004; Schaeffer et al., 2012; Webb et al., 2003; Wei et al., 2019).

Molecular chaperones are central proteins in the PN, they prevent aggregation by assisting *de novo* folding and refolding of proteins without being part of the final native conformation (Hipp et al. 2019). Chaperones also disaggregate aggregates and cooperate in the clearance of non-native proteins (Fernández-Fernández et al., 2017; Kirstein et al., 2017; Nillegoda et al., 2015; Scior et al., 2018; Wentink et al., 2020). The human cell possesses more than 300 different chaperones and they are highly conserved (Brehme et al., 2014). Chaperones were historically associated with stress response pathways upon heat stress and hence are often referred to as heat shock proteins (HSPs). Besides intracellular chaperones, also the role of extracellular chaperones have been recently emerging (Gallotta et al., 2020; Wyatt et al., 2013).

1.3.1 Molecular chaperones

Molecular chaperones can be grouped into different families according to their molecular weight: small HSP (sHSP), HSP40 or J-domain proteins (JDP), HSP60, HSP70, HSP90 and HSP110. Each family can contain multiple members and, although the majority are induced after stress conditions, some are constitutively expressed within the cell (Kampinga et al., 2009). The best characterized families are the HSP70 and the HSP90 due to their high abundance. They account for 1-2% of total proteins and have a broad spectrum of physiological functions (Labbadia and Morimoto, 2015). The HSP70 family is ubiquitous and consist of 13 members in human and 10 in *C. elegans*. The majority of the HSP70 members are stress inducible, whereas the HSC70 is constitutively expressed (HSP-1 in *C. elegans*) (Kampinga et al., 2009; Nikolaidis and Nei, 2004). HSP70s are ATP-dependent and are crucial for the cells as they participate in every stage of protein life (e.g. *de novo* folding, refolding, protein trafficking, disaggregation) as well as additional functions (e.g. clathrin-mediated endocytosis and protein degradation) (Fernández-Fernández et al., 2017; Stricher et al., 2013). The HSP90s are also ATP-dependent and function as homodimers, their clients include transcription factors, kinases and E3 ligases among other vital proteins.

Not all the HSPs are ATP-dependent and some function also independently of ATP, such as the small HSPs. Additionally, chaperones can function alone or in a combination with cooperating chaperones (co-chaperones). For instance, HSP70 cooperates with HSP40 and HSP110 to suppress protein aggregation (Ayala Mariscal et al., 2022; Dragovic et al., 2006; Rosenzweig et al., 2019; Scior et al., 2018).

Among the multitude of functions, the HSPs exhibit holdase activity, folding/refolding and chaperone-mediated disaggregation activity to maintain protein homeostasis and prevent proteotoxicity.

The holdase activity of e.g. sHSPs is ATP-independent and consists in the passive binding of aberrant proteins through abnormally exposed residues. The association with sHSPs shields the misfolded protein from forming toxic interactions and can keep the protein in a folding-competent state for the subsequent transfer to HSP70. sHSPs have a molecular weight of 12-45 kDa and they can form homo- and heterogenous oligomers to create a cage around misfolded proteins to prevent aggregation. There are 10 sHSPs in human and 14 in *C. elegans* (Hipp et al., 2019; Labbadia and Morimoto, 2015; Peter and Candido, 2002).

Folding and refolding occurs through an ATP-dependent cycle based on chaperone binding to the non-native protein, conformation remodelling and release of the protein from the chaperone. Often multiple cycles are required to fully fold a protein. Example of folding chaperones are the HSP90, HSP70 and HSP60 chaperone families (Hartl et al., 2011).

The chaperone-mediated disaggregation activity is key to resolubilizes aggregates. In eukaryotes, this activity is displayed by the HSP100 AAA+ chaperones, such as the HSP104 present in yeast (*Saccharomyces cerevisiae*) and plants (*Arabidopsis thaliana*) (Parsen et al., 1994). HSP104 is missing in higher eukaryotes, from *C. elegans* to human, where the disaggregation activity is mediated by the HSP70/HSP40/HSP110 machinery (Rampelt et al., 2012; Shorter, 2011). HSP104 and HSP110 are different and constitute two distinct heat shock families (Easton et al., 2000). The HSP110 family will be discussed in more detail in the following chapter. The HSP40s are co-chaperones of HSP70 and activate the ATP hydrolysis activity of HSP70, additionally they select protein substrates and are assumed to drive substrate specificity (Kampinga and Craig, 2010). The HSP40 family consist of 51 members in

human and 31 in *C. elegans* (Malinverni et al., 2023), they and are divided into A, B and C class based on the domain architecture (Ayala Mariscal and Kirstein, 2021).

1.3.2 The chaperone HSP110

HSP110 is one of the most abundant chaperones within eukaryotic cells (Scior et al., 2018). Although originally classified as non-canonical HSP70 members, nowadays HSP110 is recognized as a distinct family. HSP110s are large chaperones of about 100 kDa, whose known main function is to be a nucleotide exchange factor (NEF) for HSP70 (Easton et al., 2000; Yakubu and Morano, 2018). However, limited structural, biochemical and functional information are available.

Modelling analyses have revealed that HSP110 and HSP70 share a basic structural architecture. HSP70 consists of a N-terminal nucleotide binding domain (NBD), that binds ATP, and a substrate binding domain (SBD) responsible for protein binding (Fig. 1.6). SBD can be further subdivided into the β-sandwich SBDβ, a region that binds non-native proteins, and the α-helical lid SBDα, which covers the peptide binding domain (Rosenzweig et al. 2019). Similarly, HSP110 has an NBD, with high homology to HSP70, and an SBD (Easton et al., 2000). The NBD of HSP110 binds and hydrolyses ATP poorly compared to HSC70 (Oh et al., 1997). Additionally, HSP110 has a longer acidic loop linker within SBDβ as well as a C-terminal expansion. Interestingly, SBDα does not act as a lid for SBDβ, as in all HSP70, but stabilizes the NBD of HSP110 promoting HSP110-HSP70 interaction for NEF activity (Cabrera et al., 2022; Easton et al., 2000; Rosenzweig et al., 2019; Yakubu and Morano, 2018).

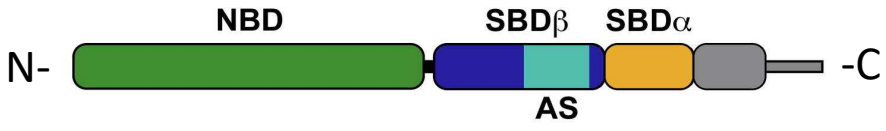

Figure 1. 6: Schematic representation of the HSP110 domains

HSP110 has a nucleotide binding domain (NBD) and a substrate binding domain (SBD), subdivided into SBDα and SBDβ. HSP110 contains an acidic sequence (AS) within the SBDβa and an extended C-terminal tail. From (Cabrera et al., 2022).

The first HSP110 studies can be dated back to the 1990s. Studies in yeast have found that *Saccharomyces cerevisiae* expresses two HSP110, Sse1 and Sse2 (Mukai et al., 1993). However, yeast HSP110 exhibits structural and functional diversity compared to human HSP110 (Raviol et al., 2006). The first mammalian HSP110s were cloned in 1990s (Lee-Yoon et al., 1995; Yasuda et al., 1995). Mammals express three cytosolic HSP110s, such as APG1, APG2 and HSP105 (Kaneko et al., 1997a, 1997b; Nonoguchi et al., 1999). *Drosophila melanogaster* and *C. elegans* express one cytosolic HSP110 and have respectively 58 and 55% sequence similarity to mammalian HSP110 (Easton et al., 2000).

After about 30 years, the HSP110s are still considered enigmatic chaperones whose functionality is still not well understood. Canonically, HSP110 functions as a nucleotide exchange factor (NEF) for HSP70, stimulating ADP release from HSP70 (Dragovic et al., 2006) (Fig. 1.7). Besides HSP110, the eukaryotic cells contain other NEF families that are structurally distinct, the BAG and the Armadillo proteins (Bracher and Verghese, 2015; Rosenzweig et al., 2019).

The HSP110 NEF function is important for both HSP70-mediated folding/refolding as well as for disaggregation activities. Interestingly, the NEF function is efficient at a sub-stoichiometric ratio (1:10) of HSP110 compared to HSP70, whereas higher levels appear to inhibit HSP70 (Wentink et al. 2020; Dragovic et al. 2006; Raviol, Sadlish, et al. 2006; Cabrera et al. 2019; Rampelt et al. 2012).

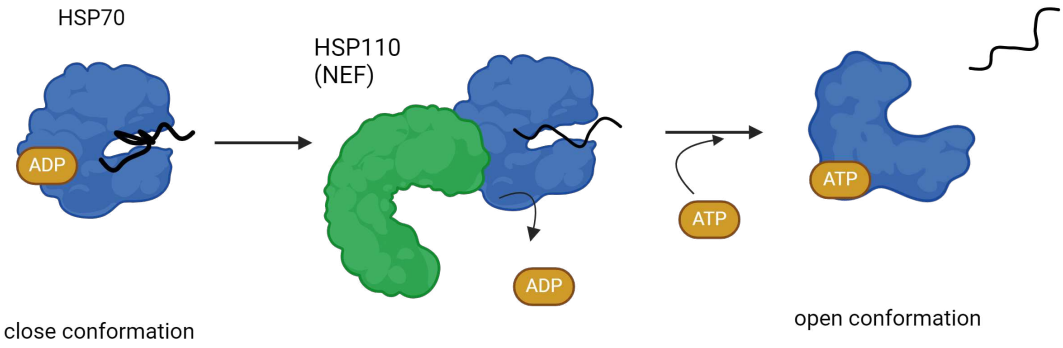

Figure 1. 7: Schematic representation of NEF activity of HSP110

HSP70 (blue) bound to ADP has a close conformation with high affinity for the substrate (e.g. unfolded, misfolded or aggregate protein). HSP110 (green) interacts with HSP70 and, through the NEF activity, induces ADP release from HSP70. Binding of ATP opens the HSP70 conformation allowing substrate release. Figure generated with BioRender.

Several studies have demonstrated that HSP70, together with HSP110 and J-domain proteins, can suppress aggregation by folding/refolding. This machinery works in an ATP-dependent cycle of substrate binding and release. The ATP-bound HSP70 has an open conformation and low affinity for protein substrates. J-domain proteins select non-native clients, transfers them to HSP70 and stimulates the low ATP hydrolysis activity of HSP70. ATP hydrolysis triggers a structural change in HSP70 from an open to a close conformation. In the close conformation, the ADP-bound HSP70 has high affinity for the non-native protein and can remodel the folding. Subsequently, HSP110 interacts with HSP70 to release ADP via its NEF activity. The binding of ATP in HSP70 induces the opening of HSP70 and the release of the substrate (Kityk et al., 2015; Rosenzweig et al., 2019). *In vitro* and *in vivo* studies have confirmed that the human HSC70/APG2/DNAJB1 and the *C. elegans* HSP-1/HSP-110/DNJ-13 can inhibit mutant HTT aggregation associated with HD (Scior et al. 2018). Recently, the same human complex, constituted of HSC70/APG2/DNAJB1, has been able to suppress also $A\beta_{1-42}$ aggregation *in vitro* (Ayala Mariscal et al. 2022).

The HSP70/HSP110/HSP40 machinery exhibits also disaggregation activity in higher eukaryotes, ranging from *C. elegans* to human. (Shorter 2011; Rampelt et al. 2012; Nillegoda & Bukau 2015; Kirstein et al. 2017). Interestingly, the disaggregation depends on the NEF activity of specifically the HSP110. It was observed that a different NEF, BAG-1, together with HSC70 and DNAJB1 could not stimulate disaggregation (Rampelt et al., 2012; Wentink et al., 2020). *In vitro* studies have demonstrated that the human disaggregase, consisting of HSC70, APG2 and DNAJB1, is highly efficient in disaggregating amyloid fibrils associated with neurodegenerative diseases, such as α-syn in PD (Gao et al. 2015). Recently, the mechanisms underlying amyloid fibrils disaggregation has been dissected showing that DNAJB1 targets HSP70 to the fibrils, the NEF HSP110 enables the efficient recirculation of HSP70 in a densely packed cluster. The HSP70 cluster on the surface of the fibril generates an entropic pulling force by steric clashes among HSP70, which results in disaggregation (Wentink et al. 2020). The chaperone-mediated disaggregation has been demonstrated also for amyloidogenic proteins other than α-syn, such as HTT and Tau (Kirstein et al. 2017; Nachman et al. 2020). However, the implication of the disaggregation activity in a physiological context is still under debate. Indeed, disaggregation can proceed via depolymerization from the end of the fibrils or by fragmentation, which can generate

small oligomeric species with high spreading and seeding potential, which can further exacerbate aggregation (Tittelmeier, Nachman, et al. 2020).

HSP110 has been suggested to function also independently from its NEF activity. One study has proposed that human HSP110s (HSP105 and APG2) are ATP-dependent foldases working in cooperation with J-domain proteins to remodel the conformation of non-native proteins (Mattoo et al., 2013). HSP110 and HSP70 showed different substrate binding propensities reflected by the divergent SBD, with HSP110 preferentially binding aromatic residues over hydrophobic ones (Xu et al., 2012). HSP110 has been also described as an holdase, based on its ability to bind heat-denatured proteins and keep them soluble *in vitro.* Luciferase and citrate synthase were used as model substrate proteins and it was demonstrated that HSP110 inhibits their aggregation when present in 1:1 ratio and that HSP110 is more efficient than HSC70 (Gotoh et al., 2004; Oh et al., 1997). More than 20 years later, this holdase function was tested in the context of neurodegenerative associated proteins. An *in vitro* study discovered that fly and human HSP110 can suppress $A\beta_{1-42}$ aggregation independently from other chaperones via an additional domain. This 138-amino acid domain is located in the C-terminus of HSP110 and it is predicted to be an intrinsically disordered region (IDR) highly conserved in *C. elegans* but missing in yeast (Yakubu and Morano, 2021). In conclusion, several *in vitro* and *in vivo* studies have linked HSP110 to neurodegenerative associated proteins: α-syn in PD (Taguchi et al., 2019; Tittelmeier et al., 2020b), SOD1 in ALS (Nagy et al., 2016; Song et al., 2013), HTT or polyQ in HD (Kirstein et al. 2017; Kuo et al. 2013), Tau in AD (Eroglu et al., 2010; Nachman et al., 2020) and $A\beta_{1-42}$ (Ayala Mariscal et al., 2022; Yakubu and Morano, 2021). However, the precise role, mechanistic insights and the physiological implications of HSP110 are still under debate.

2 Objectives of the thesis

HSP110 is a relatively poorly characterized molecular chaperone whose functional spectrum has not been fully elucidated. Importantly, HSP110 has recently been implicated in various neurodegenerative diseases, including the aggregation of $A\beta_{1-42}$ that is associated with Alzheimer´s disease. *In vitro* studies suggested that human HSP110 can inhibit $A\beta_{1-42}$ fibril formation either alone or in combination with HSC70 and a J-domain protein. However, the physiological implications of HSP110 in neurodegenerative diseases are still under debate. Therefore, I aimed to improve our understanding of the *in vivo* effect of HSP110 and its interplay with $A\beta_{1-42}$ in *C. elegans* by addressing the following research questions:

I. What is the effect of HSP-110 on $A\beta_{1-42}$ aggregation *in vivo* in the Aβ *C. elegans* model JKM2?

II. What are the global transcriptomic and proteomic changes associated with the expression of $A\beta_{1-42}$ in the *C. elegans* models JMK2 and JKM7?

3 Results

3.1 A novel *C. elegans* model pan-neuronally overexpressing the chaperone HSP-110

Molecular chaperones are essential proteins that protect the proteome of the cell and are evolutionary conserved. HSP110 is a large and highly abundant molecular chaperone present in all eukaryotes. Despite its abundance, HSP110 remains still poorly characterized. The lack of available genetic tools contributes to the limited comprehensive knowledge. Therefore, additional *in vivo* models are needed. *C. elegans* expresses one cytosolic HSP-110, while mammals possess three members (APG1, APG2 and HSP105) (Easton et al., 2000). Studying HSP110 in mammals could be challenging due to redundancy, therefore I investigate HSP110 in *C. elegans*. Interestingly, HSP105 is expressed in almost all mammalian tissues with a high expression in the brain, raising also the question of a potential function within the nervous system (Lee-Yoon et al., 1995; Yasuda et al., 1995). Recent publications have also associated HSP110 to neurodegeneration, however the implications remain still enigmatic (Tittelmeier et al., 2020a; Yakubu and Morano, 2018).

3.1.1 Generation and characterization of the pan-neuronal overexpression of *hsp-110* in *C. elegans*

In order to investigate the role of the chaperone HSP-110 *in vivo* in neuronal proteostasis and in neurodegeneration (i.e. Alzheimer´s disease), I have generated a novel *C. elegans* model that overexpressed *hsp-110* pan-neuronally. Indeed, no *C. elegans* strain that overexpressed *hsp-110* in the neurons or in any other tissues was available so far. I used the well-established *rgef-1* promoter to overexpress the nematode *hsp-110* in the neurons and I fused the gene to *gfp* into a pPD95_77 backbone plasmid (Fig. 3.1 a). The plasmid was injected into N2 wildtype nematodes by Maria Lucia Pigazzini (Kirstein Lab) and I UV-integrated the transgene to obtain a stable line. I obtained two stable transgenic lines with different HSP-110 expression

levels in the neurons visible by the green GFP fluorescence: *n hsp-110 I* and *n hsp-110 II* (Fig. 3.1 b).

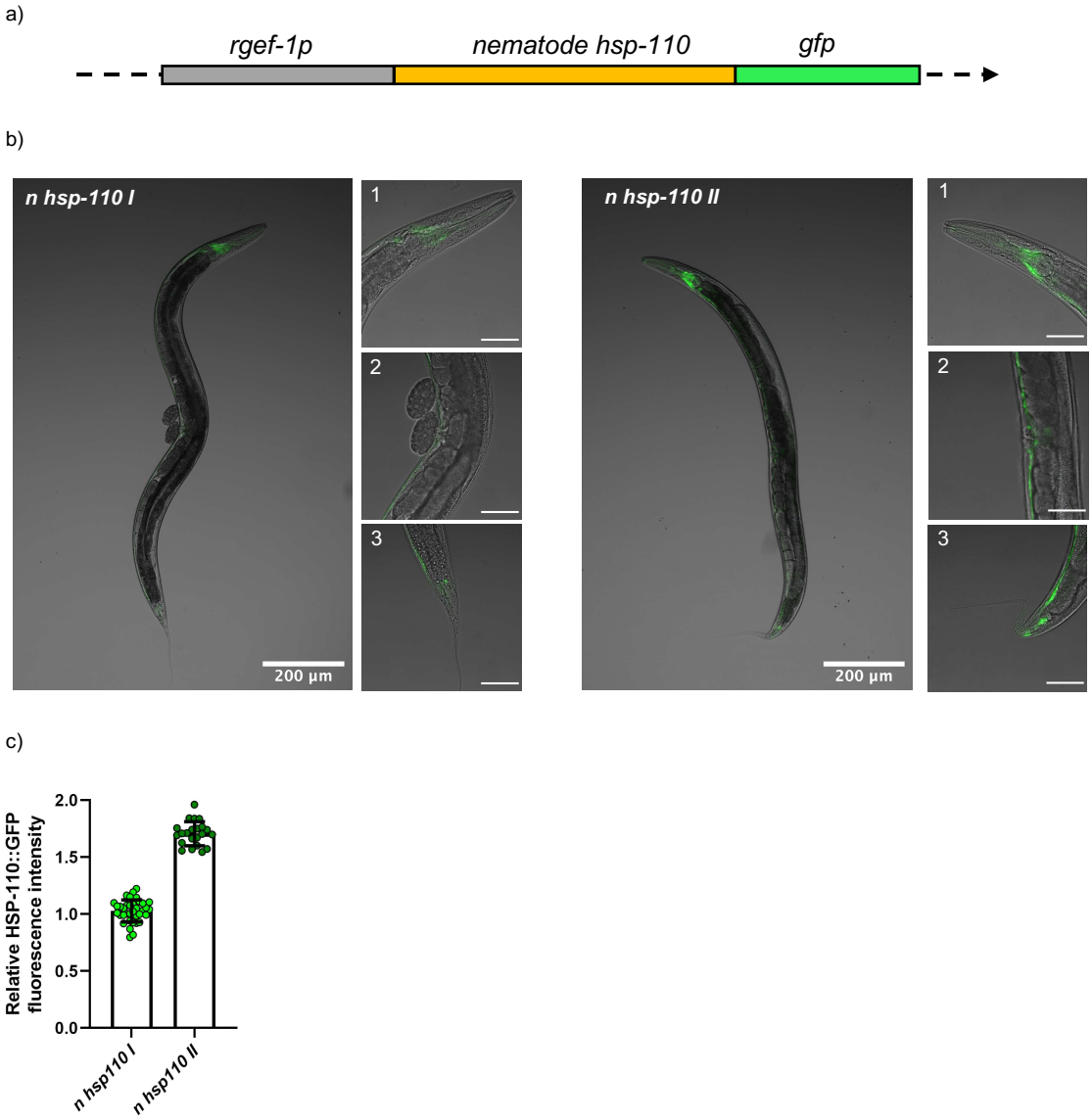

Figure 3. 1: The novel pan-neuronal *hsp-110* overexpression strains in *C. elegans*

a) Schematic representation of the *n hsp-110::gfp* construct. The nematode *hsp-110* (yellow) is fused to *gfp* (green) and the expression is pan-neuronally driven by the *rgef-1* promoter (grey).

b) Confocal fluorescent images of young adult (day 4) *n hsp-110* (*I* and *II*) *C. elegans* strains. Two strains were selected during plasmid integration: *n hsp-110 II* strain on the right shows higher HSP-110::GFP level than the *n hsp-110 I* on the left. Images are 100-fold magnified (scale bar is 200 µm). Insets 1-3 show the respective close-ups of the head region (1), the mid body (2) and the tail (3) for the respective strains. Close-up images are 400-fold magnified (scale bar is 50 µm). Further experiments were performed using *n hsp-110 I*.

c) Relative quantification of HSP-110::GFP fluorescence intensity in the whole body of *n hsp-110* (*I* and *II*) *C. elegans* strains. Confocal fluorescent images of three cohorts of *n hsp-110 I* (light green) and two cohorts of *n hsp-110 II* (dark green) nematodes (day 4) each were analyzed. Each cohort consisted of at least 10 nematodes. Fluorescence intensities were quantified by Fiji and normalized to *n hsp-110 I*. The graph shows 1.7-fold higher expression for *n hsp-110 II* relative to *n hsp-110 I*. Data are displayed as mean fluorescence intensity ± SD.

The *n hsp-110 II* line exhibited a 1.7-fold (± 0.11) higher HSP-110::GFP level relative to *n hsp-110 I*, as determined by fluorescence quantification of confocal images (Fig. 3.1 c). The pan-neuronal expression pattern was similar for both lines, with expression of HSP-110::GFP in the head, mid body and tail neurons (Fig. 3.1 b, insets). Since the pan-neuronal overexpression of *hsp-110* negatively affected the physiology of the nematodes (see chapter 3.1.2), I continued the study with the moderate overexpressing line *n hsp-110 I*, which showed a less pronounced developmental delay.

To confirm the correctness of the construct *in vivo* and to quantify the HSP-110 overexpression level, a western blot (WB) was performed using the *n hsp-110 I* nematode lysate.

The *n hsp-110 I* lysate was first analyzed with an anti-GFP antibody to ensure that GFP was not cleaved off *in vivo* (Fig. 3.2 a). As expected, the HSP-110::GFP band was visible at approximately 130 kDa. No other faster migrating GFP bands were detected, confirming that HSP-110::GFP is stable *in vivo*. Next, HSP-110 was visualized using an anti-nematode HSP-110 antibody (Fig. 3.2 b). As predicted, the antibody detected a protein band at approximately 100 kDa in N2 wildtype and *n hsp-110 I*, corresponding to the endogenous HSP-110. Moreover, a protein band migrating at 130 kDa was detected, corresponding to the transgene HSP-110::GFP that was missing in N2 wildtype and was visible in the *n hsp-110 I* lysate. The total HSP-110 expression level of *n hsp-110 I*, which is a contribution of the endogenous HSP-110 at 100 kDa and the HSP-110::GFP at 130 kDa, was quantified by western blot. The *n hsp-110 I* exhibited a 1.35-fold (± 0.19) HSP-110 expression relative to N2 wildtype on day 4 of life (Fig. 3.2 c). Notably, the overexpression within neurons is much higher. In fact, HSP-110::GFP is only expressed in neurons and was quantified in a total protein lysate relative to the endogenous HSP-110, which is expressed throughout the whole body.

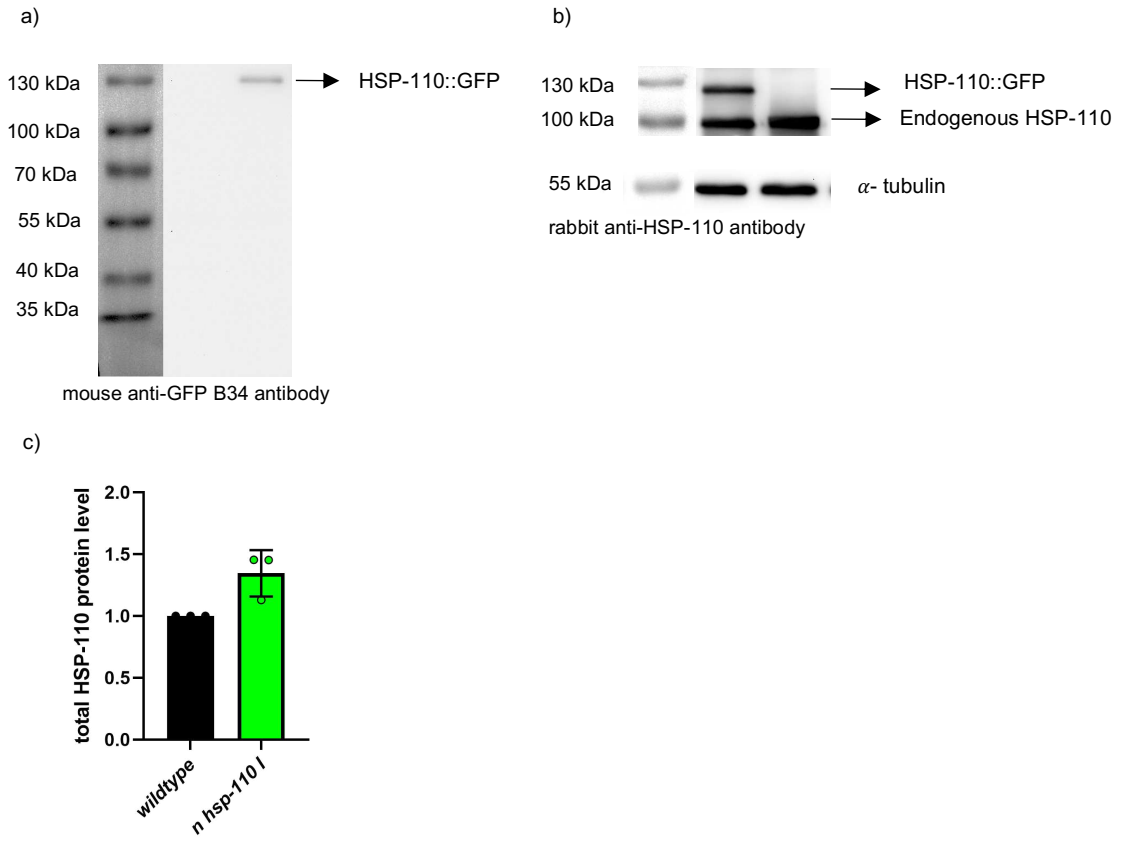

Figure 3. 2: Quantification by western blot results in 135 % HSP-110 level in *n hsp-110 I* relative to wildtype

a) Representative western blot detecting GFP protein. Soluble fractions of N2 wildtype and *n hsp-110 I* (day 4) were analyzed using mouse anti-GFP B34 antibodies (Enzo). A GFP signal (see arrow) is visible only in the *n hsp-110 I* strain at about 130 kDa.

b) Representative western blot detecting HSP-110 protein. Total lysates of N2 wildtype and *n hsp-110 I* (day 4) were used to detect HSP-110 using rabbit anti-nematode HSP-110 antibody. Endogenous HSP-110 (about 100 kDa) is visible in both N2 wildtype and *n hsp-110 I* animals (see lower arrow). Neuronal HSP-110::GFP (abou 130 kDa) is detected as a slower migrating protein band only in the *n hsp-110 I* strain (see upper arrow). Signal intensities were normalized to α-tubulin.

c) Quantification of the western blot signals shown in b) of total HSP-110 in N2 wildtype and *n hsp-110 I* (day 4). Total HSP-110 abundance (endogenous and overexpressed GFP-tagged HSP-110) was quantified in three biological replicates and normalized to α-tubulin. The graph depicts the abundance of total HSP-110 of *n hsp-110 I* (green) relative to N2 wildtype (black). Data are displayed as mean intensity ± SD. The *n hsp-110 I* strain results in 135% HSP-110 expression relative to N2 wildtype.

The expression of the transgene HSP-110::GFP was also characterized with the progression of aging by whole body confocal images of *n hsp-110 I* taken on day 4, 7 and 10 of life (Fig. 3.3).

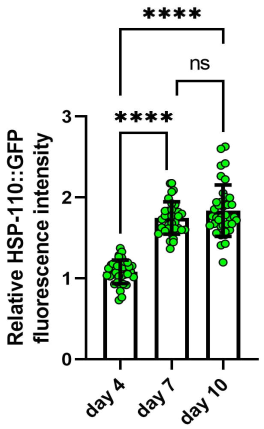

Figure 3. 3: Quantification of HSP-110::GFP with the progression of aging in *n hsp-110 I*

Confocal fluorescent images of three cohorts of 10-13 nematodes each were analyzed on day 4, day 7 and day 10 of life for the *n hsp-110 I* strain. Fluorescence intensities were quantified by Fiji. The images were corrected for the increase of autofluorescence with aging by subtracting the fluorescence intensities of age-matched N2 wildtype nematodes. Fluorescence intensities were normalized to day 4. The graph shows an increase of HSP-110::GFP level with aging (day 7 and day 10). Data are displayed as mean fluorescence intensity ± SD (graph and table). Significance was tested by one-way ANOVA + Bonferroni post hoc test (**** = $p < 0.0001$).

The fluorescence level was quantified and corrected for the increased autofluorescence characteristic of aging nematodes. The HSP::GFP fluorescence intensity level relative to day 4 increased to 1.7-fold (± 0.20) on day 7. The intensity did not increase further and showed a 1.8-fold (± 0.32) increase on day 10 relative to day 4.

3.1.2 Pan-neuronal *hsp-110* overexpression negatively affect the physiology of *C. elegans*

As mentioned above, physiological alterations were observed in *hsp-110* overexpressing *C. elegans* compared to N2 wildtype. Therefore, the fitness of the nematodes was monitored systemically using two phenotypic assays. The lifespan assay measures the survival of the nematodes as they age, i.e. how long nematodes are viable and responsive to external stimuli. On the other hand, the progeny assay calculates the viable offspring of nematodes as an indication of fertility. Both assays are well established tools to assess organismal fitness. The lifespan of the *n hsp-110 I* was first analyzed and compared to N2 wildtype (Fig. 3.4 a).

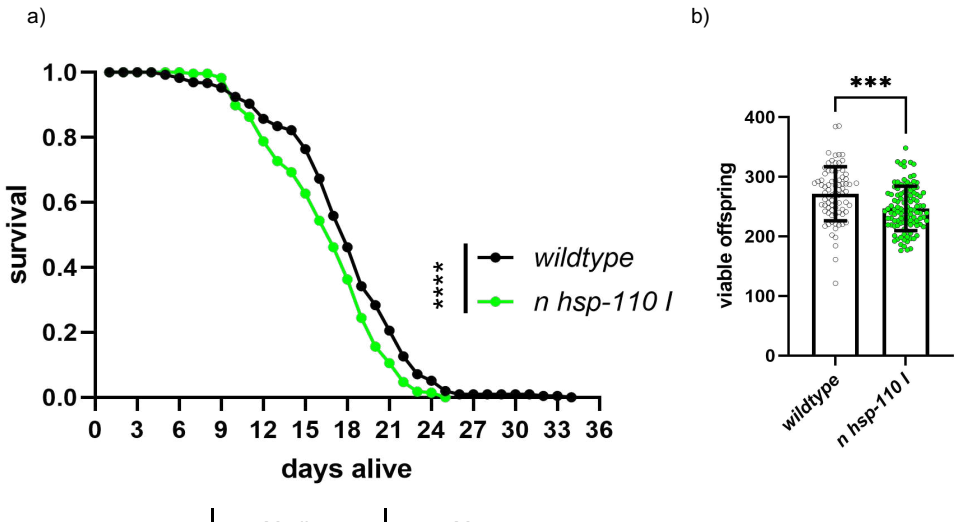

	Median (days)	Max (days)
wildtype	17.6 ± 1.2	27.3 ± 5
n hsp-110 I	16.5 ± 1.5	24 ± 0

Figure 3. 4: Pan-neuronal overexpression of *hsp-110::gfp* causes systemic detrimental effects in *C. elegans*

a) Lifespan analysis of *n hsp-110 I* versus N2 wildtype. Three cohorts with 100-180 nematodes each were tested for N2 wildtype (black) and *n hsp-110 I* (green). The survival curve shows the sum of the three independent repeats as cumulative survival probability (survival) versus age (days alive). Significance was tested with a log-rank test (**** = $p \leq 0.0001$) using Oasis 2 online tool. Average of the median lifespan ± SD and average maximum lifespan ± SD are shown in the table on the bottom.

b) Progeny assay of *n hsp-110 I* versus N2 wildtype. Three cohorts with 20-40 nematodes each were tested for N2 wildtype (black) and *n hsp-110 I* (green). Scatter dot plot shows the average number

of offspring per nematode as mean ± SD. Significance was assessed by t-test with Welch´s correction (*** p ≤ 0.001).

One of the biological replicates of N2 wildtype lifespan was obtained by my colleague Sudarson Baskaran (Kirstein Lab). The *n hsp-110 I* exhibited a 1-day reduction in its median lifespan compared to N2 wildtype (from 17.6 ± 1.2 to 16.5 ± 1.5 days). The median lifespan indicates the day when survival reaches 50%. The *n hsp-110 I* showed also a reduction of about 3 days in its maximal lifespan compared to N2 wildtype (from 27.3 ± 5 to 24 ± 0 days).

Secondly, the progeny of the *n hsp-110 I* was quantified (Fig. 3.4 b). Two biological replicates of *n hsp-110 I* were obtained by Govinda Adhikari (Kirstein Lab). The assay indicated a reduction in brood size of approximately 10% for *n hsp-110 I* compared to N2 wildtype (from 271 ± 45 to 247 ± 37 offspring). Taken together, these data point towards a reduction of the nematode fitness when *hsp-110* is overexpressed in the neurons. Interestingly, RNAi (RNA interference) also exhibited defects in the physiology by impairing survival, development and fertility (Kamath and Ahringer, 2003; Tittelmeier et al., 2020b).This suggests that the chaperone HSP-110 plays an important role in *C. elegans* growth and fertility and that its levels need to be tightly regulated.

3.1.3 HSP-110 does not alter HSP-1 and DNJ-13 levels but is a modulator of the autophagy pathway *in vivo*

HSP-110 cooperates with other chaperones to ensure protein folding and prevent aggregation. HSP-110 functions as a nucleotide exchange factor for the HSP-1 cycle and, together with a J-domain protein, regulates the folding and off-folding pathway of various proteins in *C. elegans*. For instance, the HSP-1/HSP-110/DNJ-13 combination was shown to exert a potent effect in counteracting protein aggregation in *C. elegans* (Kirstein et al., 2017; Nillegoda et al., 2015; Rampelt et al., 2012; Scior et al., 2018). Therefore, I wondered whether the modulation of HSP-110 could affect the protein levels of the cooperating chaperones HSP-1 and DNJ-13 in *C. elegans*. Indeed, it was shown that overexpression of HSP110 in a murine model increased the level of HSC70, homolog of HSP-1 (Taguchi et al., 2019).To investigate this, I first quantified the total HSP-1 and DNJ-13 levels by western blot when *hsp-110* is overexpressed using day 4 of life *n hsp-110 I* lysate. I also monitored the chaperone levels when *hsp-110* is

depleted by RNAi using day 4 of life *eri-1* mutant *C. elegans* strain, which enhances neuronal RNAi (Kennedy Scott et al., 2004) (Fig. 3.5).

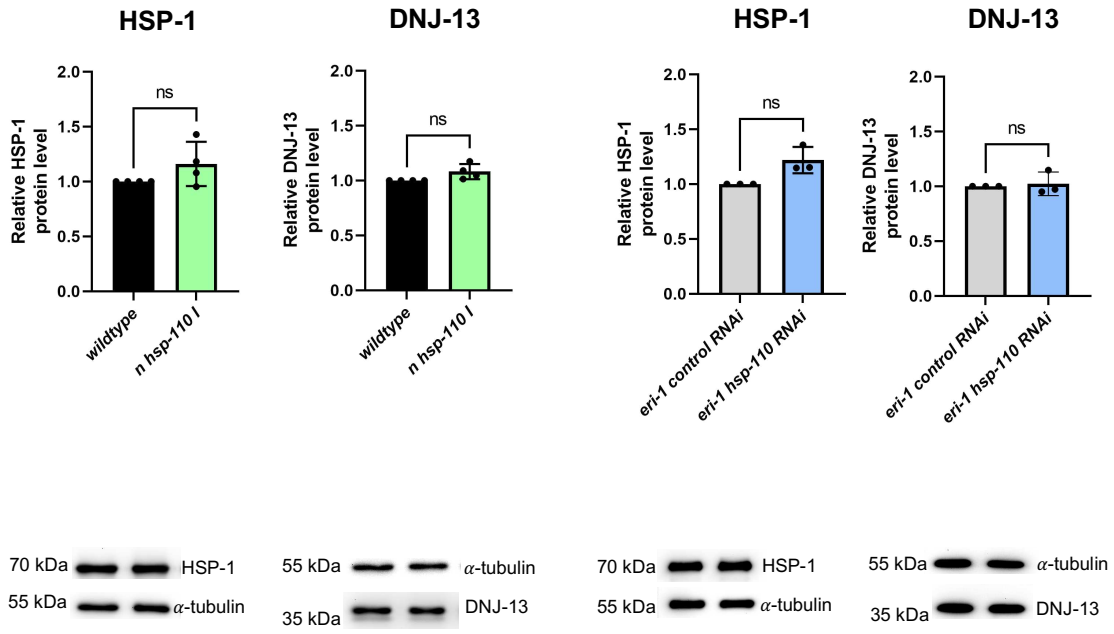

Figure 3. 5: Modulation of HSP-110 does not change the levels of HSP-1 and DNJ-13

Neither overexpression nor RNAi-mediated depletion of HSP-110 does affect the protein levels of the partner chaperones HSP-1 and DNJ-13. On the left, total lysate of N2 wildtype (black) and *n hsp-110 I* (light green) of day 4 of life animals were analyzed by western blot to assess HSP-1 and DNJ-13 protein levels upon pan-neuronal overexpression of HSP-110. On the right, total lysate of *eri-1* control RNAi (grey) and *eri-1 hsp-110* RNAi (light blue) of day 4 of life old animals were analyzed by western blot to assess HSP-1 and DNJ-13 protein levels when *hsp-110* is systemically downregulated by RNAi. Relative quantifications of at least three biological replicates, normalized to α-tubulin, are shown as scatter dot plots on the upper panel. Data are displayed as mean fluorescence intensity ± SD. Significance was tested by t-test with Welch´s correction (ns = $p > 0.05$). Representative western blots are shown on the bottom.

HSP-1 and DNJ-13 were detected using anti-nematode HSP-1 and anti-nematode DNJ-13 antibodies. Values were normalized to α-tubulin and displayed as relative quantification to the respective controls. I also confirmed that *hsp-110* RNAi was effective in the *eri-1* strain by western blot, detecting a 70% reduction of systemic HSP-110 (Fig. S.2a). No significant difference in the systemic abundance of HSP-1 and

DNJ-13 was observed, suggesting that the expression of these two chaperones is not affected by HSP-110 modulation on day 4.

In addition, the chaperone system and the autophagy pathway are known to be tightly regulated. Autophagy is a clearance mechanism that ensures the removal of misfolded proteins, damaged organelles and pathogens. It is induced when the chaperone system is compromised. This is potentially a compensatory mechanism to guarantee the clearance of misfolded and aggregated proteins when chaperones can no longer assure protein homeostasis (Feleciano et al., 2019). Therefore, the impact of HSP-110 modulation on autophagy was analyzed. The autophagy markers LGG-1 and SQST-1/p62 were quantified by western blot following *hsp-110* overexpression and RNAi-mediated knockdown in day 4 nematodes (Fig. 3.6).

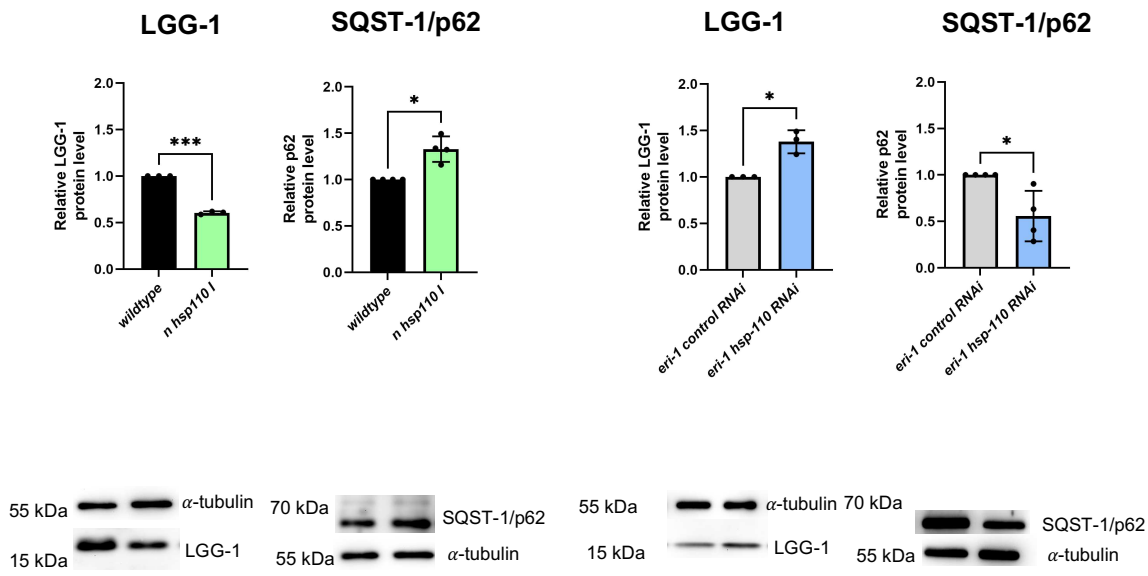

Figure 3. 6: HSP-110 modulates autophagy

HSP-110 overexpression reduces and depletion of HSP-110 activates autophagy. On the left, total lysate of wildtype (black) and *n hsp-110 I* (light green) of day 4 old animals were analyzed by western blot to assess LGG-1 and SQST-1/p62 protein levels when *hsp-110* is pan-neuronally upregulated. On the right, total lysate of *eri-1* control RNAi (grey) and *eri-1 hsp-110* RNAi (light blue) of day 4 old animals were analyzed by western blot to assess LGG-1 and SQST-1/p62 protein levels when *hsp-110* is systemically downregulated by RNAi. Relative quantifications of at least three biological replicates, normalized to α-tubulin, are shown as

scatter dot plots on the upper panel. Data are displayed as mean fluorescence intensity ± SD. Significance was tested by t-test with Welch´s correction (* = $p \leq 0.05$; *** = $p \leq 0.001$). Representative western blots are shown on the bottom.

LGG-1 is an autophagosome marker and elevated levels could be a consequence of either an induction or an impairment of autophagy, leading to accumulation of autophagosomes. Hence, it is important to monitor also the cargo adapter protein SQST-1/p62, which is degraded by autophagy. LGG-1 was detected using the anti-nematode LGG-1 antibody, while SQST-1/p62 was detected using the anti-nematode SQST-1/p62 antibody. Values were normalized to α-tubulin and were quantified relative to the respective controls. The data showed that upon *hsp-110* depletion, LGG-1 accumulated (1.38-fold (± 0.12)) and SQST-1/p62 simultaneously decreased (0.56-fold (± 0.27)), indicating that autophagy was induced. When *hsp-110* was overexpressed, LGG-1 decreased (0.61-fold (± 0.02)) and SQST-1/p62 levels increased (1.33-fold (± 0.14)), suggesting that autophagy was instead compromised. These findings indicate that HSP-110 is a negative modulator of autophagy, i.e. *hsp-110* overexpression impairs autophagy whereas *hsp-110* depletion induces autophagy.

3.2 HSP-110 is a modulator of amyloid beta ($A\beta_{1-42}$) aggregation in *C. elegans*

Together with HSP70 and a J-domain protein, the chaperone HSP110 can prevent the aggregation as well as resolubilize amyloidogenic aggregates implicated in neurodegenerative diseases (i.e. α-syn, HTT, and Tau) (Gao et al., 2015; Nachman et al., 2020; Scior et al., 2018). Thus, I wondered if HSP110 could also modulate the aggregation of the $A\beta_{1-42}$ peptide involved in Alzheimer´s disease. A very recent publication from the Kirstein lab showed that the human HSC70/HSP110/DNAJB1 can suppress $A\beta_{1-42}$ fibrilization *in vitro* (Ayala Mariscal et al., 2022). Interestingly, another publication also showed that the human HSP110s alone can inhibit $A\beta_{1-42}$ fibril formation *in vitro* (Yakubu and Morano, 2021).Therefore, I explored the potential role of HSP110 in $A\beta_{1-42}$ fibrillation in a physiological context using *C. elegans* as an *in vivo* model.

3.2.1 Pan-neuronal *hsp-110* overexpression enhances $A\beta_{1-42}$ aggregation

To better understand the role of HSP-110 in the regulation of Aβ aggregation *in vivo*, I used the $A\beta_{1-42}$ *C. elegans* model (JKM2) that was previously established in the Kirstein lab (Gallrein et al., 2021). This strain mimics Alzheimer's disease pathology and has been already employed for the study of modulators of $A\beta_{1-42}$ aggregation (Gallrein et al., 2023; Pras et al., 2021; Schiavi et al., 2023). The strain expresses pan-neuronally the untagged human $A\beta_{1-42}$ peptide and a sub-stoichiometric $A\beta_{1-42}$ fraction labelled with the mScarlet fluorescent protein. This operon allows simultaneous $A\beta_{1-42}$ aggregation and *in situ* visualization. Indeed, the strain exhibits $A\beta_{1-42}$ aggregation, spreading and severe proteotoxicity. I crossed the *C. elegans* nAβ model with *n hsp-110 I* strain, overexpressing *hsp-110* in the neurons. I obtained the nAβ x *n hsp-110 I* strain, which expresses both *hsp-110* and $A\beta_{1-42}$ neuronally (Fig. 3.7 a + S.1 a). I also crossed the nmScarlet strain with the *n hsp-110 I* to obtain the control strain nmScarlet *x n hsp-110 I,* which expressed the mScarlet fluorescent protein and *hsp-110* (Fig. 3.7 b + S.1 b).

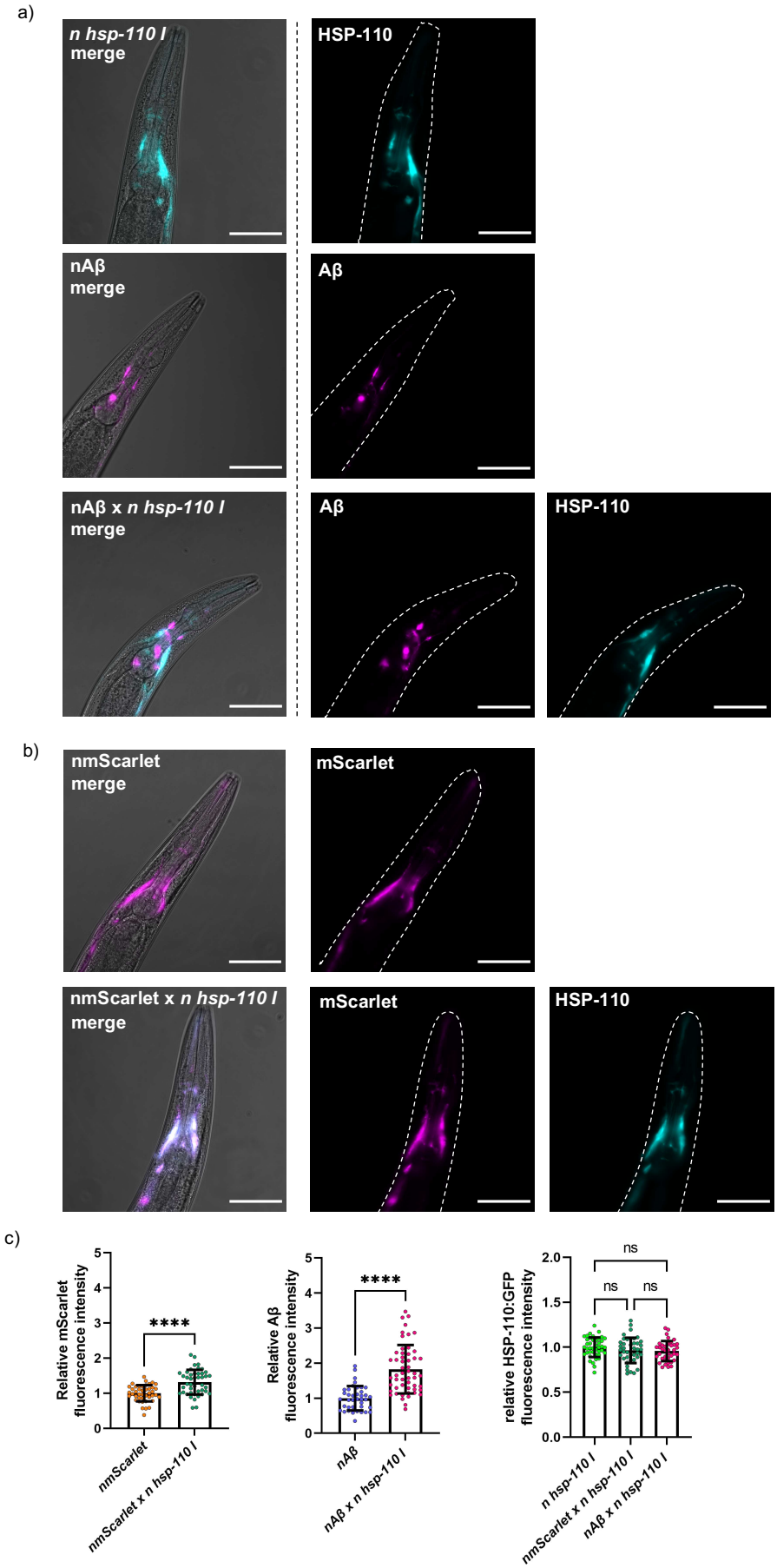
a)
n hsp-110 I
merge
HSP-110
nAβ
merge
Aβ
nAβ x n hsp-110 I
merge
Aβ
HSP-110
b)
nmScarlet
merge
mScarlet
nmScarlet x n hsp-110 I
merge
mScarlet
HSP-110
c)
Relative mScarlet fluorescence intensity
****
nmScarlet
nmScarlet x n hsp-110 I
Relative Aβ fluorescence intensity
****
nAβ
nAβ x n hsp-110 I
relative HSP-110:GFP fluorescence intensity
ns
ns
ns
n hsp-110 I
nmScarlet x n hsp-110 I
nAβ x n hsp-110 I

Figure 3. 7: Overexpression of *hsp-110* leads to elevated Aβ/mScarlet levels on day 4

a) Confocal fluorescent images of parental strains (nAβ, *n hsp-110 I*) and the cross *(*nAβ x *n hsp-110 I*). The head regions of day 4 old animals are depicted as merge, Aβ fluorescence (magenta) and HSP-110 fluorescence (cyan). Images are 400-fold magnified (scale bar is 50 µm). 100-fold magnified images are in supplementary figure S.1 a.
b) Confocal fluorescent images of the parental control strain (nmScarlet) and the cross (nmScarlet x *n hsp-110 I*). The head regions of day 4 old animals are depicted as merge, mScarlet fluorescence (magenta), and HSP-110 fluorescence (cyan). Images are 400-fold magnified (scale bar is 50 µm). 100-fold magnified images are in supplementary figure S.1 b.
c) Relative quantification of mScarlet and Aβ fluorescence intensities after *hsp-110* overexpression. On the left, mScarlet fluorescence intensity after *hsp-110* overexpression was measured in the head of nmScarlet x *n hsp-110 I* (dark green) relative to nmScarlet animals (orange). In the middle, Aβ fluorescence intensity after *hsp-110* overexpression was quantified in the head of nAβ x *n hsp-110 I* (magenta) relative to nAβ animal (blue). Confocal fluorescent images of nematodes of three cohorts of 10-19 nematodes each were analyzed on day 4 of life. Fluorescence intensities were quantified by Fiji and normalized to the respective controls. Scatter dot plots show an increase of mScarlet and Aβ levels upon *n hsp-110* I crossing. Data are displayed as relative mean fluorescence intensity ± SD (see table below). Significance was assessed by t-test with Welch´s correction (ns = $p > 0.05$; **** = $p \leq 0.0001$). On the right, relative quantification of HSP-110::GFP fluorescence intensity was measured in the head of day 4 old *n hsp-110 I* animals (light green), nmScarlet x *n hsp-110 I* (dark green) and nAβ x *n hsp-110 I* (magenta). Confocal fluorescent images of three cohorts of 10-15 nematodes each were analyzed on day 4 of life. Fluorescence intensities were quantified by Fiji and normalized to *n hsp-110 I*. Data are displayed as relative mean fluorescence intensity ± SD. Significance was assessed by one-way ANOVA + Bonferroni post hoc test (ns = $p > 0.05$).

The fluorescence tags of both transgenes, HSP-110::GFP (depicted in cyan) and mScarlet or mScarlet-$A\beta_{1-42}$ (depicted in magenta) allow an *in vivo* and *in situ* analysis by fluorescence microscopy. The nAβ x *n hsp-110 I* exhibited elevated levels of mScarlet- $A\beta_{1-42}$ (1.83-fold (± 0.69)) relative to nAβ. The *nmScarlet x n hsp-110 I* showed increased mScarlet levels (1.32-fold (± 0.36)) relative to nmScarlet strain. The HSP-110::GFP levels were unchanged in the crosses relative to *n hsp-110 I*. This was confirmed by imaging the head of day 4 of life nematodes by confocal microscopy. The fluorescence intensity was quantified relative to their parental strains. (Fig. 3.7 c).
To study the effect of HSP-110 on $A\beta_{1-42}$ aggregation *in vivo* and with the progression of aging, FLIM was employed. FLIM is a cutting-edge technique that has already been used to monitor the aggregation of $A\beta_{1-42}$ as well as other amyloidogenic proteins (HTT and α-syn) in *C. elegans* (Gallrein et al., 2021; Kaminski Schierle et al., 2011; Laine et

al., 2019; Pigazzini et al., 2020). FLIM measures the fluorescence lifetime (also known as tau or τ) of the fluorescent protein mScarlet. The lifetime is expressed in nanoseconds (ns) and it is the time that a photon requires to decay from its excited state back to its ground state after excitation. The lifetime is independent of the concentration and the fluorescence intensity, but it is dependent on the microenvironment (Becker, 2012). Indeed, when mScarlet is incorporated into Aβ fibrils, its lifetime decreases due to quenching by increasing β-sheets formation. It is therefore possible to monitor and quantify the aggregation propensity *in vivo*, *in situ* and in a non-invasive manner by monitoring the reduction in the τ value.

FLIM measurements were performed in the head neurons of day 4 and day 7 old nematodes using *nmScarlet*, *nmScarlet x n hsp-110 I,* nAβ and nAβ x *n hsp-110 I* strains. On day 4, the aging process begins for nematodes and consequently the proteostasis capacity of the nematode declines giving rise to the first aggregates (Labbadia and Morimoto, 2014). Animals on day 7 are older, thus the aggregation can be followed with the progression of aging.

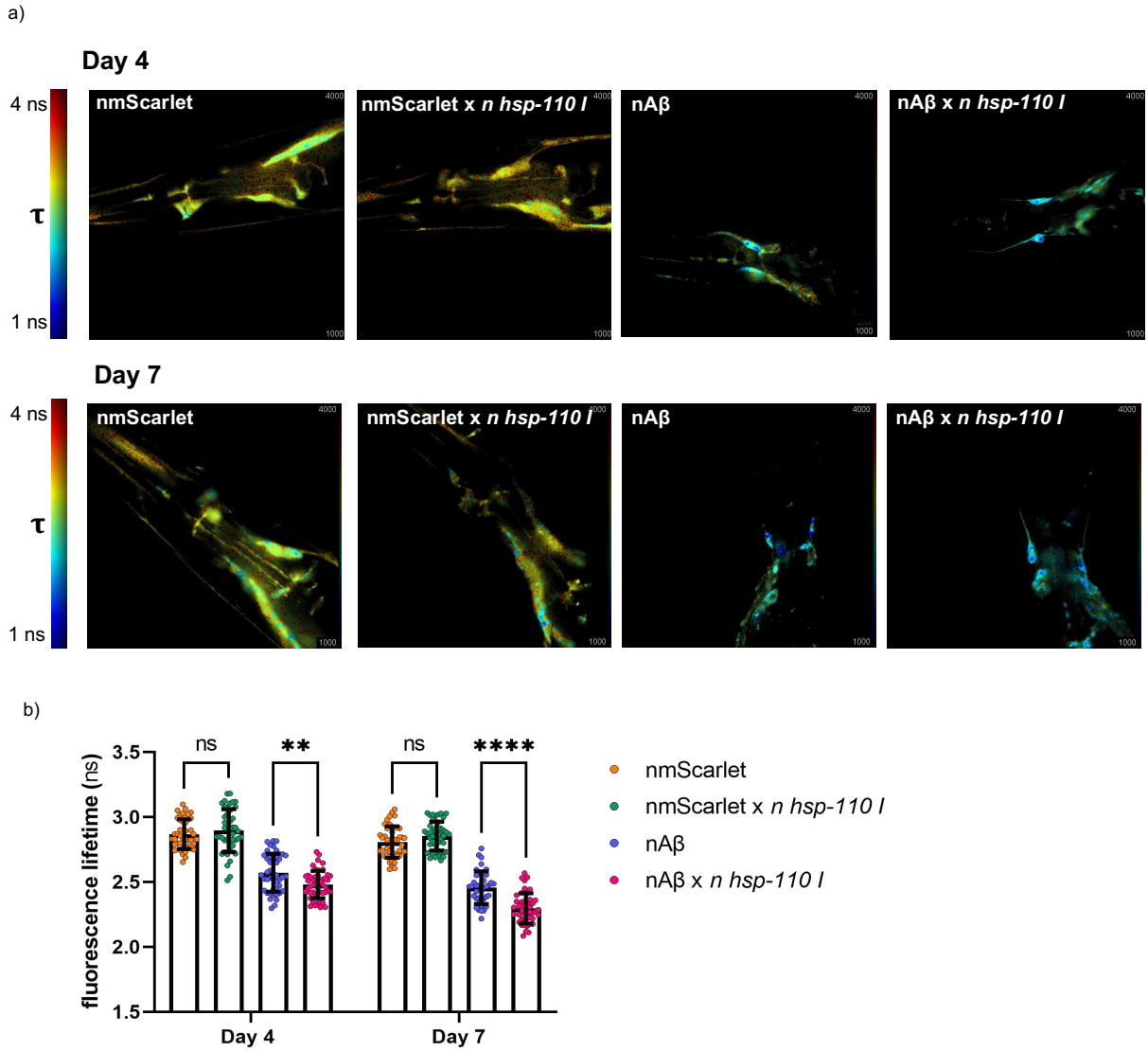

Figure 3. 8: Pan-neuronal overexpression of *hsp-110* enhances Aβ$_{1-42}$ aggregation

a) Representative TCSPC-FLIM images of nmScarlet and nAβ parental strains as well as the respective crosses with *n hsp-110 I*. Head neurons of day 4 old animals (top row) and day 7 old animals (bottom row) were analyzed. Images depict the pixel-wise fluorescence lifetime in ns merged with the fluorescent intensity. Fluorescence lifetime is false-colored: blue represents low fluorescent lifetimes (1 ns) and red high fluorescent lifetimes (4 ns).

b) Scatter dot plot of the average fluorescence lifetime (ns) of mScarlet in nmScarlet and nAβ parental strains as well as the respective crosses with *n hsp-110 I*. Data display the average fluorescence lifetimes ± SD for day 4 (left side) and day 7 (right side) of nmScarlet (orange), nmScarlet x *n hsp-110 I* (dark green), nAβ (blue) and nAβ x *n hsp-110 I* (magenta). Every dot represents the average fluorescence lifetime for the head neurons of one single nematode. Three independent cohorts of 10-18 animals each were analyzed. Significance was tested by two-way ANOVA + Bonferroni post hoc test (** = $p \leq 0.01$; **** = $p \leq 0.0001$).

Fluorescence lifetime values can be visualized in the TCSPC images by false-colouring (Fig 3.8 a). A yellow-red colour indicates higher τ value and reflects soluble protein (i.e nmScarlet). Conversely, a blue colour represents lower τ value and is indicative of protein aggregation (i.e nAβ). The averaged τ value for the whole head of each nematode was plotted (Fig. 3.8 b). Consistent with previous publications (Gallrein et al., 2021), nAβ exhibited lower τ values (blue foci) compared to the nmScarlet control on day 4 and on day 7. Indeed, the nAβ strain is characterized by the aggregation of the $A\beta_{1-42}$ peptide which reduces the τ value compared to the nmScarlet control from 2.87 ns to 2.57 ns on day 4 (****$p < 0.0001$) and from 2.81 ns to 2.46 ns on day 7 (****$p < 0.0001$). $A\beta_{1-42}$ aggregation exacerbates with aging, evidenced by an increasing number of blue foci in the representative TCSPC images from day 4 to day 7, as well as by the decrease τ value from 2.57 ns on day 4 to 2.46 ns on day 7 (***$p = 0.0001$). As expected, the overexpression of *hsp-110* did not alter the fluorescence lifetime in *nmScarlet x n hsp-110 I* compared to nmScarlet nematodes on day 4 and day 7. Interestingly, when *hsp-110* was overexpressed in the neurons of the nAβ the blue foci increased on both day 4 and on day 7. On day 4, nAβ x *n hsp-110 I* showed a decrease of the τ valus compared to nAβ from 2.57 ns to 2.48 ns. The reduction was more pronounced on day 7 with a decrease in τ compared to nAβ from 2.46 ns to 2.30 ns, indicating that *hsp-110* overexpression increased $A\beta_{1-42}$ aggregation.

To obtain additional information on the conformational variability of Aβ, I analyzed the histograms of nAβ and nAβ x *n hsp-110 I* strains on day 4 and day 7 of life (Fig. 3.9).

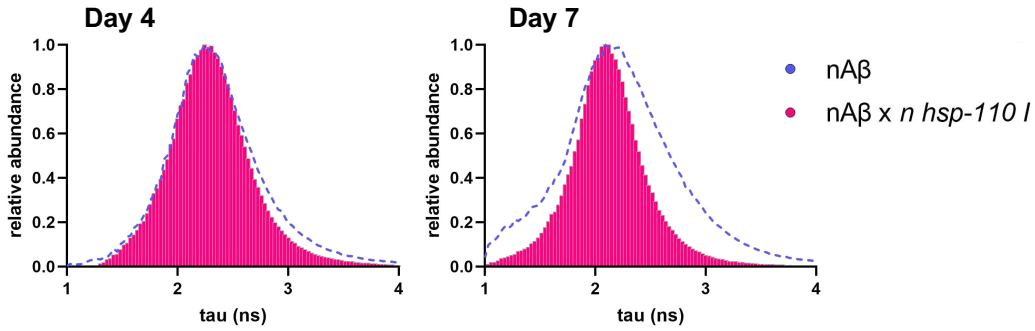

Figure 3. 9: The *hsp-110* overexpression appeared to reduce Aβ $_{1-42}$ conformational variability

The histograms show the average occurrence of pixels (y-axis) with a certain fluorescence lifetime (x-axis) and represent the Aβ conformers distribution in nAβ and nAβ x *n hsp-110 I* animals. The fluorescence lifetime in the head neurons, as in Fig. 3.8 b, was measured for day 4 old (left) and day 7

old animals (right). The histogram of nAβ x *n hsp-110 I* animals is depicted in magenta and overlayed with the histogram of the parental nAβ animals (dashed blue curve).

The histogram represents the abundance of pixels (y-axes) with specific fluorescence lifetime values (x-axes) and is the sum of all analyzed animals for each strain. On day 7 the shape of the histogram for nAβ x *n hsp-110 I* (magenta) sharpened, showing a narrowed occurrence of τ values compared to nAβ (blue dashed line). This could indicate that HSP-110 generated more homogenous $A\beta_{1-42}$ aggregate conformational species in older animals. However, it is not yet possible to associate specific τ values with their exact corresponding $A\beta_{1-42}$ conformational state (e.g. oligomeric state, prefibrillar, fibrillar species). Nevertheless, FLIM analysis showed that *hsp-110* overexpression increased $A\beta_{1-42}$ aggregation and could potentially reduce the conformational variability.

To note, HSP-110 is a cytosolic protein while the $A\beta_{1-42}$ peptide is located both inside and outside the neurons. For example, $A\beta_{1-42}$ is known to accumulate also in the coelomocytes of the nematodes. Coelomocytes are cells that take up macromolecules from the body cavity and that are suggested to have immune and hepatic-like functions. In order to investigate if HSP-110 could have an effect also on the secretion of $A\beta_{1-42}$, I analyzed the $A\beta_{1-42}$ levels in coelomocytes. Coelomocytes were visualized using a *unc-122p::gfp* marker (strain ZIM1048 kindly provided by the Zimmer Lab) and the fluorescence intensity of mScarlet-$A\beta_{1-42}$ was quantified using confocal microscopy (Fig. 3.10).

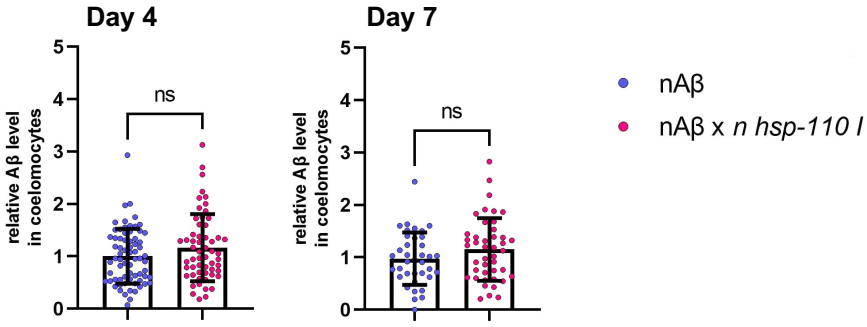

Figure 3. 10: *hsp-110* overexpression does not affect secretion of $A\beta_{1-42}$

Aβ levels in the coelomocytes of nAβ and nAβ x *n hsp-110 I* animals on day 4 (left) and 7 (right) of life. The nAβ and nAβ *x n hsp-110 I* strains were crossed with the ZIM1048 coelomocyte marker strain (*unc-*

122p::gfp). Confocal images of Aβ fluorescence intensities in coelomocytes were quantified. Scatter dot plots show the relative Aβ fluorescence for nAβ x *n hsp-110 I* (magenta) to Aβ (blue) for day 4 of life (on the left) and day 7 of life (on the right). Three cohorts of 8-14 animals were analyzed. Significance was assessed by t-test with Welch´s correction (ns = p > 0.05).

There was no statistical difference in the relative $A\beta_{1-42}$ levels in the coelomocytes between nAβ and nAβ x *n hsp-110 I* on both day 4 and day 7, suggesting that HSP-110 affects the intraneuronal $A\beta_{1-42}$.

3.2.2 RNAi mediated *hsp-110* depletion ameliorates $A\beta_{1-42}$ aggregation

As mentioned above, overexpression of *hsp-110* increased $A\beta_{1-42}$ aggregation hence *hsp-110* depletion could lead to the opposite effect. Therefore, the already available Ahringer bacterial library was used to deplete *hsp-110* by RNAi mediated knockdown (Feleciano et al., 2019; Kamath and Ahringer, 2003). Nematodes were fed with either control RNAi (empty vector) or *hsp-110* RNAi bacteria. RNAi induces a systemic depletion of *hsp-110*, however neurons are less sensitive to it. In order to enhance neuronal RNAi, the *eri-1* mutant was crossed with nmScarlet and nAβ strains to obtain nmScarlet *eri-1* and nAβ *eri-1* strains. To further increase RNAi efficiency, I used the second generation of nematodes fed with RNAi bacteria and I confirmed a 45-70 % of *hsp-110* RNAi efficiency by western blot (Fig. S.2 b). The levels of mScarlet and mScarlet-$A\beta_{1-42}$ in control RNAi condition as well as upon *hsp-110* depletion were tested by confocal imaging on day 4 animals (Fig. 3.11).

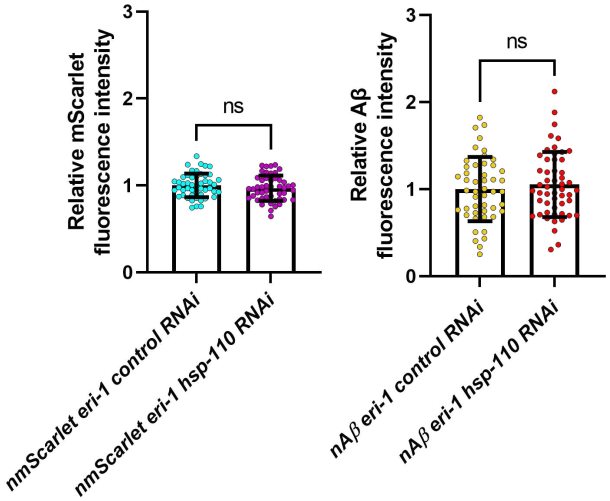

Figure 3. 11: Depletion of *hsp-110* does not change mScarlet/mScarlet- Aβ$_{1-42}$ levels on day 4

Relative quantification of mScarlet and nAβ fluorescence intensities of the parental strains and upon *hsp-110* depletion. On the left, mScarlet fluorescence intensity upon *hsp-110* depletion was quantified in the head of nmScarlet *eri-1 hsp-110* RNAi animals (purple) relative to nmScarlet *eri-1* control RNAi (cyan). On the right, Aβ fluorescence intensity upon *hsp-110* depletion was quantified in the head of nAβ *eri-1 hsp-110* RNAi animals (red) relative to nAβ *eri-1* control RNAi (yellow). Confocal fluorescent images of three cohorts of 10-19 nematodes each were analyzed on day 4 of life. Fluorescence intensities were quantified by Fiji. Scatter dot plots show so statistical difference in Aβ/mScarlet levels upon *hsp-110* depletion. Data are displayed as relative mean fluorescence intensity ± SD (see table below). Significance was assessed by t-test with Welch´s correction (ns = $p > 0.05$).

The fluorescence intensity was quantified relative to the control RNAi and shows no statistical difference on day 4 between control RNAi and *hsp-110* RNAi conditions for both nmScarlet *eri-1* and nAβ *eri-1* strains. Conversely, *hsp-110* overexpression exhibited higher mScarlet/ mScarlet- Aβ$_{1-42}$ levels on day 4.

Next, FLIM was performed on nmScarlet *eri-1* and nAβ *eri-1* strains on both day 4 and day 7 to study the effect of *hsp-110* depletion on Aβ$_{1-42}$ aggregation propensity (Fig. 3.12 a).

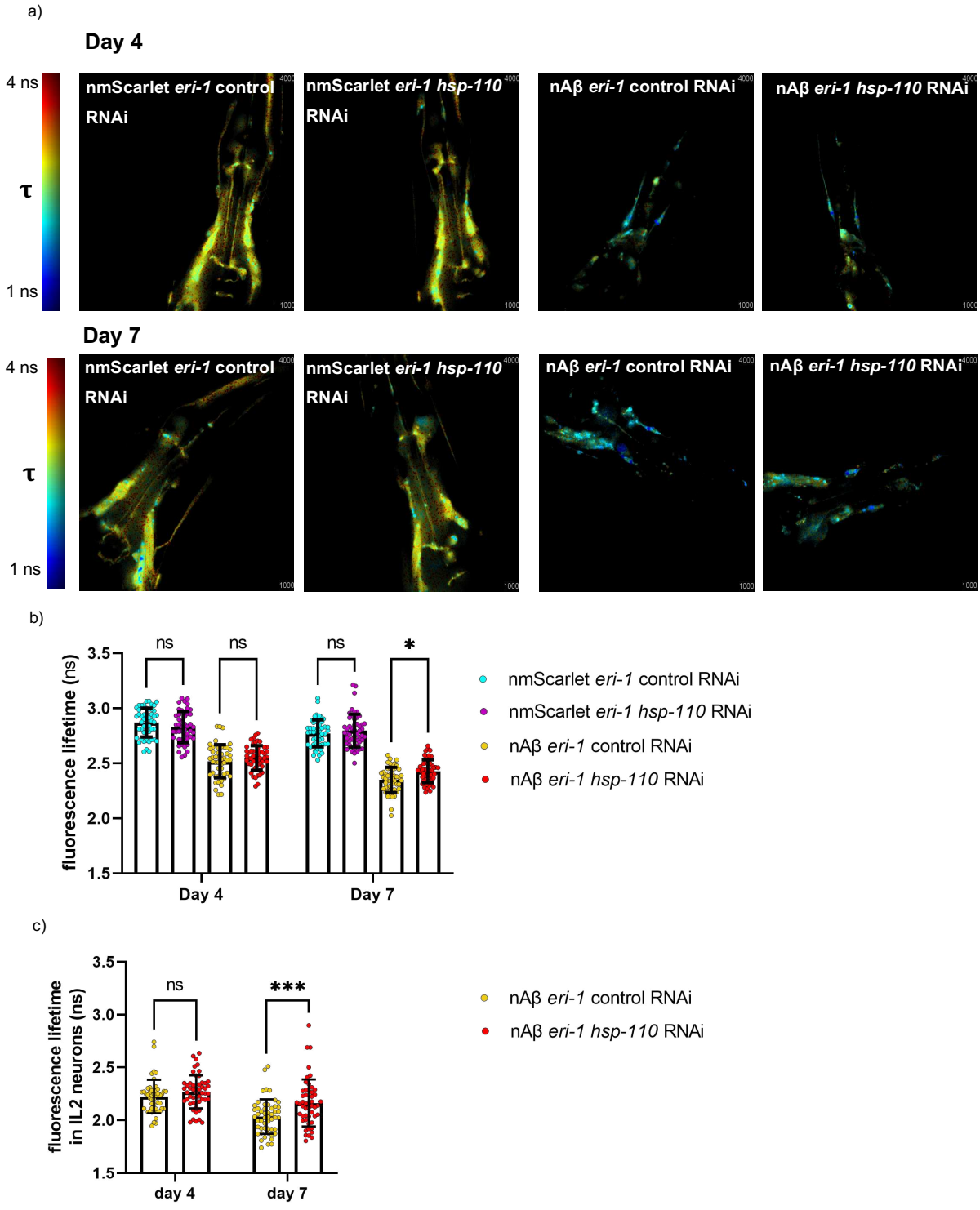

Figure 3. 12: Systemic *hsp-110* depletion decreases Aβ$_{1-42}$ aggregation

a) Representative TCSPC-FLIM images of nmScarlet *eri-1* and nAβ *eri-1* nematodes after systemic *hsp-110* depletion by RNAi. Head neurons of day 4 old animals (top row) and day 7 old animals (bottom row) were analyzed. Images depict the pixel-wise fluorescence lifetime (ns) merged with the

fluorescent intensity of mScarlet in nmScarlet and nAβ nematodes. Fluorescence lifetime is false-colored: blue represents low fluorescence lifetime (1 ns) and red high fluorescent lifetime (4 ns).

b) Scatter dot plot of the average fluorescence lifetime in nanoseconds (ns) of the head neurons of mScarlet in nmScarlet *eri-1* and nAβ *eri-1* nematodes after systemic *hsp-110* depletion by RNAi or control RNAi conditions. Data display the average fluorescence lifetime ± SD for day 4 (left side) and day 7 old (right side) of nmScarlet *eri-1* control RNAi (cyan), nmScarlet *eri-1 hsp-110* RNAi (purple), nAβ *eri-1* control RNAi (yellow), and nAβ *eri-1 hsp-110* RNAi (red) animals as in (a). Every dot represents the average fluorescence lifetime for the head neurons of one single nematode. Three independent cohort of 13 - 20 animals each were analysed. Significance was tested by two-way ANOVA + Bonferroni post hoc test (ns = $p > 0.05$; * = $p \leq 0.05$).

c) Scatter dot plot of the average fluorescence lifetime (ns) of mScarlet in nAβ *eri-1* nematodes after systemic *hsp-110* depletion by RNAi in the IL2 neurons. Data display the average fluorescence lifetime ± SD for day 4 (left side) and day 7 old (right side) nAβ *eri-1* control RNAi (yellow) and nAβ *eri-1 hsp-110* RNAi (red) animals. Every dot represents the average fluorescence lifetime in the IL2 neurons of one single nematode. Three independent cohort of 13-20 animals were analysed. Significance was tested by two-way ANOVA + Bonferroni post hoc test (ns = $p > 0.05$; *** = $p \leq 0.001$).

The depletion of *hsp-110* did not alter significantly the fluorescence lifetime in nmScarlet *eri-1* on day 4 and day 7 compared to the control RNAi condition. In nAβ *eri-1 hsp-110* RNAi instead a moderate but significant increase in the fluorescence lifetime was measured compared to the control RNAi on day 7, where the τ value raised from 2.35 ns to 2.43 ns (Fig. 3.12 b). Higher τ values are a proxy for more soluble $A\beta_{1-42}$ species, indicating a reduction in $A\beta_{1-42}$ aggregation upon *hsp-110* depletion. Notably, the reduction in $A\beta_{1-42}$ aggregation was more pronounced in older nematodes when analyzing only the IL2 neurons (Fig. 3.12 c). The IL2 neurons are a subset of head neurons characterized by the onset of $A\beta_{1-42}$ aggregation and are assumed to be the most vulnerable neurons to $A\beta_{1-42}$ aggregation. When the head of the nAβ *eri-1 hsp-110* RNAi strain was segmented for the IL2 neurons, the τ value incremented from 2.03 ns to 2.16 ns on day 7 compared to the control RNAi. No significant effect on the IL2 neurons was instead detected for the overexpression of neuronal *hsp-110* (Fig. S. 3).

To gain additional information on the $A\beta_{1-42}$ conformational landscape, I analysed the histograms of nAβ *eri-1 hsp-110* RNAi (in red) in the whole head and compared it to the control RNAi condition (yellow line) on day 4 and day 7 of life (Fig. 3.13).

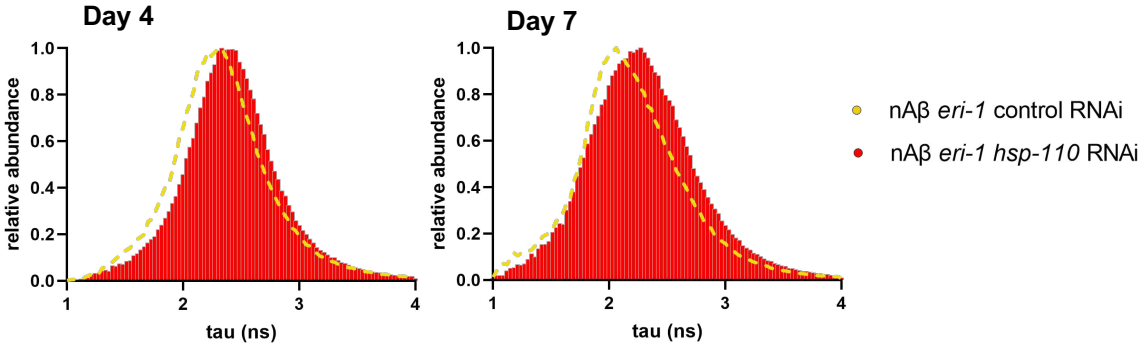

Figure 3. 13: Systemic *hsp-110* depletion shows more soluble Aβ $_{1-42}$ conformers

The histograms show the average occurrence of pixels (y-axis) with a certain fluorescence lifetime (x-axis) and represent the Aβ conformers distribution in nAβ *eri-1* control RNAi and nAβ *eri-1 hsp-110* RNAi conditions. The fluorescence lifetime in the head neurons, as in (Fig 3.12 b), was measured on day 4 (left) and on day 7 (right) old animals.

The shape of the histogram did not change as observed for *hsp-110* overexpression (section 3.2.1). However, a shift of the histogram to the right is apparent and indicates the occurrence of more soluble $A\beta_{1-42}$ species with higher fluorescence lifetime values. Taken together, these data point to a reduction of $A\beta_{1-42}$ aggregation in older animals when *hsp-110* is depleted by RNAi. Interestingly, this effect is more significant in the IL2 neurons which mark the onset of $A\beta_{1-42}$ aggregation.

3.2.3 Overexpression and depletion of *hsp-110* compromises organismal fitness of both nAβ and control nematodes

Based on the $A\beta_{1-42}$ aggregation FLIM data, I wondered if a systemic impact on the physiology of the nematodes was detectable. The overexpression of *hsp-110* increased $A\beta_{1-42}$ aggregation, which in turn could potentially exacerbate proteotoxicity. Conversely, reduced $A\beta_{1-42}$ aggregation upon *hsp-110* depletion could ameliorate proteotoxicity. To assess systemically the physiology of the nematodes, I performed lifespan and fecundity assays on nAβ nematodes and the respective controls when *hsp-110* is overexpressed. Moreover, I performed the lifespan assay when *hsp-110* is depleted in nAβ *eri-1* and in controls. Lifespan measures the survival of the nematodes in days while fecundity evaluates the number of viable offspring for each nematode.

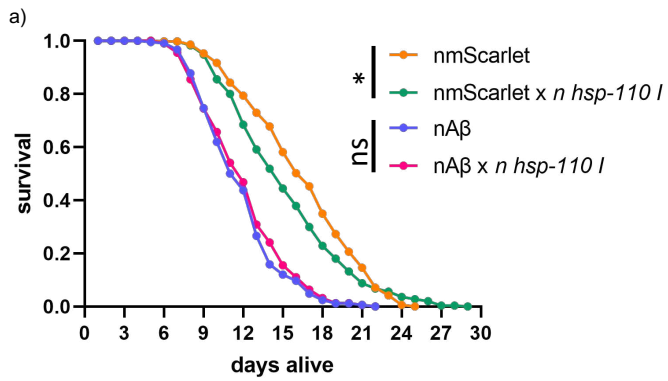

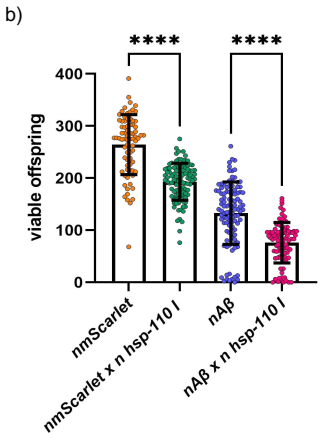

	Median (days)	Max (days)
nmScarlet	16.5 ± 1	23.7 ± 0.6
nmScarlet x *n hsp-110 I*	14.5 ± 0.6	26.7 ± 1.2
nAβ	11.6 ± 1.3	18 ± 2.6
nAβ x *n hsp-110 I*	11.8 ± 0.5	18.7 ± 2.1

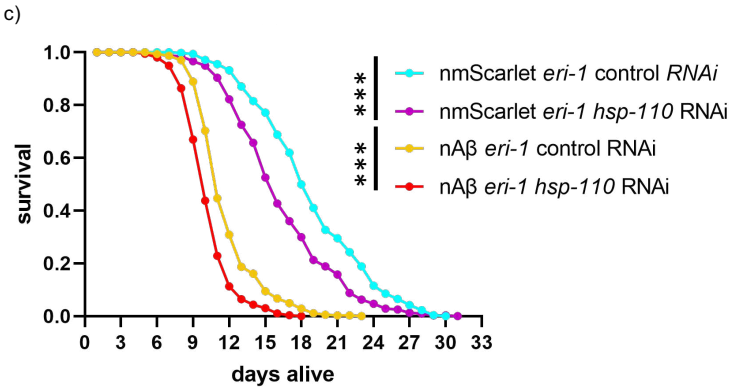

	Median (days)	Max (days)
nmScarlet *eri-1* control RNAi	18.4 ± 1.2	26.3 ± 2.5
nmScarlet *eri-1 hsp-110* RNAi	16.8 ± 2.5	26.0 ± 4.3
nAβ *eri-1* control RNAi	10.9 ± 0.3	19.0 ± 3.0
nAβ *eri-1 hsp-110* RNAi	9.7 ± 0.9	15.7 ± 1.5

Figure 3. 14: Overexpression and depletion of *hsp-110* impairs organismal fitness of Aβ and control animals

a) Lifespan analysis of nmScarlet versus nAβ animals and their respective crosses with *n hsp-110 I*. Three independent cohorts with 150-180 nematodes each were tested for nmScarlet (orange), nmScarlet x *n hsp-110 I* (dark green), nAβ (blue) and nAβ x *n hsp-110 I* (magenta). The survival curve shows the sum of the three independent repeats as cumulative survival probability (survival) versus age (days alive). Significance was tested with a log-rank test (* = $p \leq 0.05$) using Oasis 2 online tool. Average of the median lifespan ± SD and average maximum lifespan ± SD are shown in the table below.

b) Progeny assay of nmScarlet versus nAβ animals and their respective crosses with *n hsp-110 I*. Three independent cohorts with 20-40 nematodes each were tested for nmScarlet (orange), nmScarlet x *n hsp-110 I* (dark green), nAβ (blue) and nAβ x *n hsp-110 I* (magenta). Scatter dot plot shows the average number of viable offspring per nematode as mean ± SD, values are reported also in the table below. Significance was assessed by one-way ANOVA + Bonferroni post hoc test (**** = $p \leq 0.0001$).

c) Lifespan analysis of nmScarlet versus nAβ nematodes after systemic *hsp-110* depletion by RNAi. Three independent cohorts with 100-195 nematodes each were tested for mScarlet *eri-1* control RNAi (cyan), nmScarlet *eri-1 hsp-110* RNAi (purple), nAβ *eri-1* control RNAi (yellow) and nAβ *eri-1 hsp-110* RNAi (red). The survival curve shows the sum of the three independent repeats as cumulative survival probability (survival) versus age (days alive). Significance was tested with a log-rank test (**** = $p \leq 0.00001$) using Oasis 2 online tool. Average of the median lifespan ± SD and average maximum lifespan ± SD are shown in the table below.

Overexpression of *hsp-110* compromised the fitness of both nAβ and control animals (Fig. 3.14 a). Pan-neuronal *hsp-110* overexpression reduced of about 2 days (from 16.5 ± 1 to 14.5 ± 0.6 days) the median and about 3 days (from 26.7 ± 0.6 to 23.7 ± 1.2 days) the maximal lifespan in nmScarlet x *n hsp-110 I* compared to nmScarlet. The nAβ and nAβ x *n hsp-110 I* did not show a reduction of the lifespan but a compromised fertility (Fig. 3.14 b). The nAβ x *n hsp-110* strain exhibited a reduction of about 43% of viable offspring compared to nAβ from 133 ± 60 to 76 ± 39. The nmScarlet x *n hsp-110 I* strain showed a reduction in the brood size of about 27% from 264 ± 58 to 183 ± 35 compared to nmScarlet. Two biological replicates of the progeny assay for nmScarlet x *n hsp-110 I* were obtained by my colleague Govinda Adhikari (Kirstein Lab). These data confirm that *hsp-110* overexpression is detrimental to the physiology of the nematodes, as seen in section 3.1.2, and that this affects nmScarlet and nAβ strains. In addition, also the lifespan upon *hsp-110* depletion showed a negative effect for both, control and nAβ nematodes (Fig. 3.14 c). The nmScarlet *eri-1 hsp-110* RNAi showed a reduction of about 1.6 days (from 18.4 ± 1.2 to 16.8 ± 2.5 days) in the median lifespan compared to nmScarlet *eri-1* control RNAi. The nAβ *eri-1 hsp-110* RNAi exhibited a

reduction of about 1 day in the median lifespan (from 10.9 ± 0.3 to 9.7 ± 0.9 days) and about 3 days in the maximal lifespan (from 19.0 ± 3 to 15.7 ± 1.5 days) compared to nAβ *eri-1* control RNAi. One biological replicate of nAβ *eri-1* control RNAi lifespan was obtained by my colleague Mira Sleiman (Kirstein Lab). These results demonstrated that also a depletion of *hsp-110* is detrimental for control and nAβ animals. Although *hsp-110* RNAi ameliorates $A\beta_{1-42}$ aggregation, it did not rescue the proteotoxicity. However, it is plausible that HSP-110 exerted pleotropic effects in *C. elegans* and its modulation is detrimental, suggesting that HSP-110 levels need to be tightly regulated.

3.3 Transcriptomic and proteomic analyses provide insights into the novel $A\beta_{1-42}$ *C. elegans* models

Transcriptomic and proteomic analyses were performed to explore differentially expressed genes (DEGs) and differentially expressed proteins (DEPs) in the novel $A\beta_{1-42}$ *C. elegans* models. Nematodes of the two $A\beta_{1-42}$ strains, nAβ and mAβ, and their respective controls, nmScarlet and mmScarlet, were analysed at two different time points during aging, on day 4 (young adults) and on day 8 of life (older animals).
The transcriptomic analysis was conducted in collaboration with the Sawarkar lab (MPI Freiburg & Cambridge University, UK). Total RNA was extracted from the nAβ, mAβ, nmScarlet and mmScarlet strains on day 4 and on day 8 of life. The Sawarkar lab performed the RNA sequencing, the bioinformatic analysis and provided a list of up- and downregulated genes for nAβ and mAβ relative to their controls (Fig. 3.15 a). For each condition, I selected the significant up- and downregulated genes by applying a fold discovery rate (FDR) cut-off < 0.05. The number of DEGs per condition was plotted, with upregulated DEGs displayed in pink and downregulated DEGs in blue (Fig. 3.15 b). On day 4, the nAβ strain showed a marked change in gene expression with 221 DEGs, of which 160 were upregulated and 61 were downregulated. On day 4, 91 DEGs were detected for the mAβ strain, with 42 upregulated and 49 downregulated genes. On day 8, the nAβ strain showed only 17 DEGs, with 6 upregulated and 11 downregulated genes. On day 8, the mAβ showed 108 DEGs, with 64 upregulated and 44 downregulated genes.

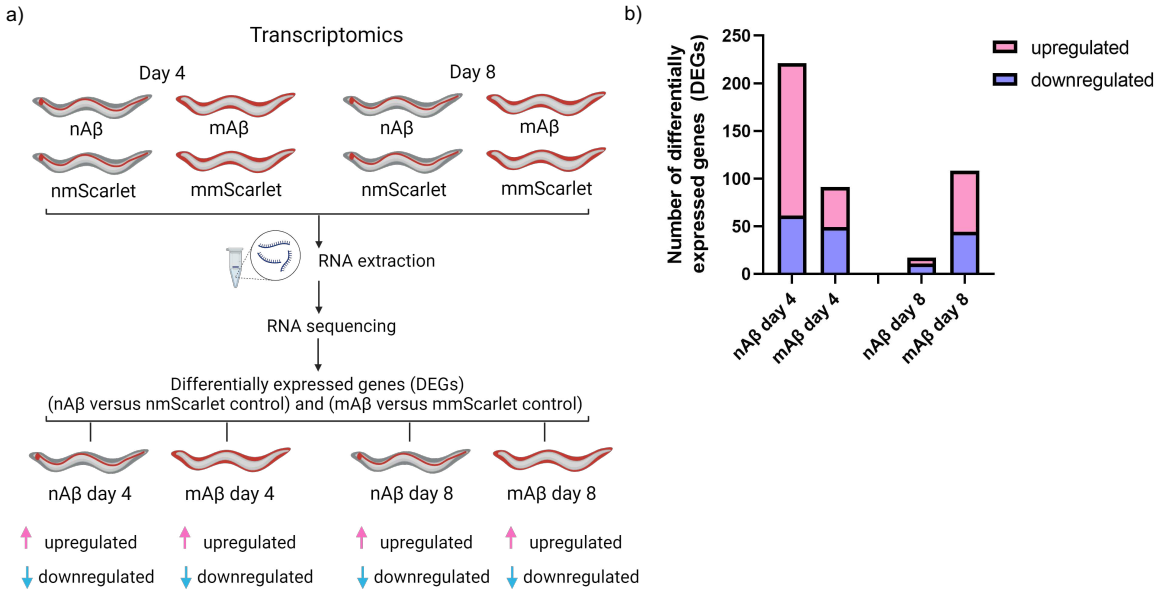

Figure 3. 15: Transcriptomic analysis

a) Schematic illustration of the transcriptomic analysis. Total RNA was extracted from nAβ (JKM2), mAβ (JKM7), nmScarlet (JKM3) and mmScarlet on day 4 and day 8. Three cohorts were analyzed for each condition except for the nmScarlet control strain, where only two replicates could be provided.

b) Resulting DEGs from the transcriptomic analysis. The total number of DEGs per condition is indicated on the y-axes in the stacked bar graph. DEGs were selected with a cut-off of FDR < 0.05. Upregulated DEGs are shown in pink and downregulated DEGs in blue.

The proteomic analysis was conducted in collaboration with the Savitski lab (EMBL, Heidelberg). I harvested the nAβ, mAβ, nmScarlet and mmScarlet strains on day 4 and on day 8. The Savitski lab performed total protein extraction, mass spectrometry and the bioinformatic analysis. A list of up- and downregulated proteins was generated for nAβ and mAβ relative to their controls (Fig. 3.16 a). Proteins were classified as hits or candidates by the Savitski lab according to the FDR and the fold change. Hit proteins have an FDR below 0.05 and a fold change of at least 2, while candidates have an FDR below 0.2 and a fold change of at least 1.5. To compare transcriptomics and proteomics, I applied to hit and candidate proteins the same FDR cut-off used in the transcriptomics (FDR < 0.05). The number of DEPs per condition was plotted, with upregulated proteins displayed in pink and downregulated proteins highlighted in blue (Fig. 3.16 b). On day 4, nAβ strain exhibited 159 DEPs with 98 upregulated and 61 downregulated proteins, whereas mAβ showed 144 DEPs with 74 upregulated and 70

downregulated proteins. On day 8, the nAβ strain exhibited 132 DEPs with 101 upregulated and 31 downregulated proteins whereas the mAβ showed 118 DEPs with 71 upregulated and 47 downregulated proteins.

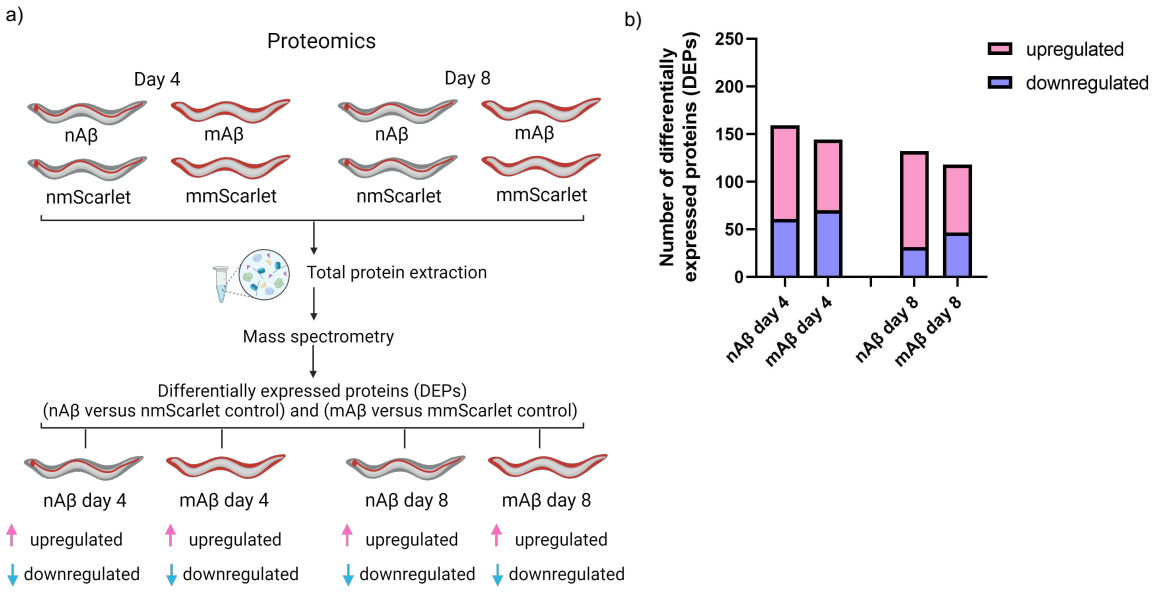

Figure 3. 16: Proteomic analysis

a) Schematic illustration of the proteomic analysis. Total proteins were extracted from nAβ (JKM2), mAβ (JKM7), nmScarlet and mmScarlet on day 4 and day 8. For each condition, three cohorts were analysed.

b) Resulting DEPs from the proteomic analysis. The total number of DEPs per condition is indicated on the y-axes in the stacked bar graph. DEPs were selected with a cut-off of FDR < 0.05. Upregulated DEPs are shown in pink and downregulated DEPs in blue.

In the following sections, a preliminary biological interpretation of the DEPs for each condition is presented. Functional enrichment analysis was performed using gene ontology (GO) with a focus on the biological process (BP).

3.3.1 Proteomic analysis of neuronal $A\beta_{1-42}$ *C. elegans* on day 4

The 98 upregulated DEPs found for nAβ on day 4 were subjected to GO to determine the overrepresented biological processes (Table 3.1). Interestingly, biological processes related to nucleosome and chromatin GO terms were enriched.

Table 3. 1: GO analysis for upregulated DEPs in nAβ day 4

List of GO terms for biological process and their ID with an FDR < 0.05.

Term ID and description	Genes	Gene count	Background genes	FDR
GO:0006334_Nucleosome assembly	*his-48*|*nasp-2*|*his-24*|*hil-2*	4	24	0.0401
GO:0031497_Chromatin assembly	*his-48*|*nasp-2*|*his-24*|*ifc-2*|*hil-2*	5	51	0.0401

The 50 most upregulated DEPs were annotated (Table 3.2).

Table 3. 2: 50 most upregulated DEPs in nAβ day 4

List of the 50 most upregulated DEPs in nAβ day 4 ranked by their FDR value. The gene name and the Uniprot ID are given for each DEP. In addition, each DEP was annotated with a short description and known human homologs.

	Gene	Protein Uniprot ID	Description	Human homologs	FDR
1	*CELE_F07B7.2*	G5ECF6	Uncharacterized protein		3.60E-10
2	*CELE_T21H3.1*	H2KZV5	Predicted to be involved in lipid metabolic process		9.48E-10
3	*acox-1.5*	P34355	Predicted acyl-CoA oxidase activity, peroxisome	Acyl-CoA oxidase 1 (ACOX1)	3.52E-08
4	*pdpr-1*	Q9U300	Predicted oxidoreductase	Pyruvate dehydrogenase phosphatase regulatory subunit (PDPR)	3.51E-07

			activity, mitochondrion		
5	*C36C5.5*	O16405	Predicted extracellular holdase		6.51E-07
6	*C01G6.3*	Q17572	Uncharacterized protein		9.11E-07
7	*nlt-1*	Q23655	Predicted lipid binding activity	SCP2 sterol binding domain containing 1 (SCP2D1), hydroxysteroid 17-beta dehydrogenase 4 (HSD17B4)	1.27E-06
8	*cht-1*	Q11174	Predicted endochitinase	Chitinase (CHIT1, CHIA, CHI3L2, CHI3L1, OVGP1)	1.74E-06
9	*perm-2*	O44145	Permeable eggshell, structural integrity of oocytes and embryonic eggshell		6.93E-06
10	*clec-190*	Q9NAP0	Uncharacterized protein, predicted C-type Lectin		7.65E-06
11	*his-24*	P10771	Histone 24	Histone (H1.0, H1.4, H1.5)	9.07E-06
12	*ule-1*	O01780	Predicted chitin binding protein		2.26E-05
13	*gale-1*	Q564Q1	UDP-galactose-4-epimerase	UDP-galactose-4-epimerase (GALE)	2.26E-05
14	*cbd-1*	O45599	Predicted chitin binding, involved in eggshell formation		2.69E-05
15	*clec-150*	O44871	Predicted carbohydrate binding activity		3.50E-05
16	*hpo-6*	Q95Y17	Uncharacterized protein, located in membrane raft		3.61E-05
17	*CELE_F18A1.7*	Q19536	Uncharacterized protein		3.66E-05
18	*nasp-2*	O17687	Predicted histone binding	Nuclear autoantigenic sperm protein (NASP)	3.66E-05
19	*cpr-9*	Q20950	Predicted cysteine-type endopeptidase	Cathepsin B (CTSB)	5.87E-05

20	*CELE_ZK105.1*	Q965Z4	Uncharacterized protein		6.28E-05
21	*C17G1.2*	Q93240	Uncharacterized protein		7.59E-05
22	*rnr-2*	P42170	Ribonucleotide reductase	Ribonucleotide reductase regulatory subunit M2 (RRM2)	9.01E-05
23	*ubr-4*	A0A0S4XR36	Uncharacterized protein, predicted UBR E3 ubiquitin ligase homolog	Ubiquitin protein ligase E3 component n-recognin 4 (UBR4)	1.50E-04
24	*perm-4*	O44144	Permeable eggshell, structural integrity of oocytes and embryonic eggshell		2.38E-04
25	*top-2*	Q23670	Predicted topoisomerase type II	DNA topoisomerase II (TOP2A/B)	3.30E-04
26	*asp-6*	O01530	Aspartic protease	Progastricsin (PGC), cathepsin E (CTSE), pepsinogen (PGA3/4/5	4.65E-04
27	*C44B7.5*	Q18594	Uncharacterized protein		5.72E-04
28	*CELE_D1054.10*	Q18943	Uncharacterized protein		5.72E-04
29	*clec-63*	O45444	Predicted C-type lectin		6.02E-04
30	*CELE_F54D5.4*	Q20770	Uncharacterized protein, involved in innate immune response		7.42E-04
31	*clec-65*	O45443	Predicted C-type lectin		7.42E-04
32	*ctsa-1.2*	P52715	Cathepsin A, predicted serine-type carboxypeptidase	Cathepsin A (CTSA)	8.21E-04
33	*plpp-1.1*	A0A238UKJ7	Predicted phosphatidate phosphatase	Phospholipid phosphatase (PLPP1/2/3)	8.41E-04
34	*his-48*	Q27876	Histone 48	Histone (H2B)	8.41E-04
35	*CELE_F49C12.7*	Q20584	Predicted kinase		8.59E-04
36	*skr-14*	Q9N3U9	Skp1-related, ubiquitin ligase complex component	S-phase kinase associated protein (SKP1)	8.72E-04

37	*clec-85*	Q95XX2	Predicted C-type lectin, intestine		1.15E-03
38	*skpo-1*	Q20616	Peroxidase		1.20E-03
39	*CELE_F35F10.1*	Q9GYT3	Predicted hydrolase activity		1.40E-03
40	*CELE_T03F1.11*	P91423	EF-hand domain-containing protein, predicted calcium binding		1.40E-03
41	*skr-9*	G5EFA9	Skp1-related, ubiquitin ligase complex component	S-phase kinase associated protein (SKP1)	2.15E-03
42	*mtl-1*	P17511	Metallothionein		2.23E-03
43	*CELE_H34I24.2*	O76672	Uncharacterized protein		2.29E-03
44	*rsp-8*	Q9XTZ2	SR Protein (splicing factor), predicted to be involved in mRNA splicing	RNA binding protein (CIRBP, RBM3, RBMX, RBMY), transformer 2 alpha homolog (TRA2A/B)	2.34E-03
45	*pmp-1*	Q18597	Predicted ATP-binding cassette (ABC) transporter, peroxisome	ATP binding cassette subfamily D (ABCD1/2/3/4)	2.35E-03
46	*asp-5*	O01532	Predicted aspartic-type endopeptidase	Progastricsin (PGC), cathepsin E (CTSE), pepsinogen (PGA3/4/5	2.35E-03
47	*lec-10*	G5EBV4	Galectin, intestine	Galectin 3 (LGALS3)	2.36E-03
48	*cyp-33c8*	O02641	Cytochrome P450 family	Cytochrome P450 (CYP2J2/C9/U1/C18)	2.45E-03
49	*CELE_T09B4.5*	O02155	Uncharacterized protein		2.54E-03
50	*CELE_F09C8.1*	O01300	Predicted phospholipase, intestine	Phospholipase B1 (PLB1)	2.98E-03

Interestingly, histones (i.e. *his-48, his-24, his-2, htz-1, his-71, hil-2*) were found to be highly upregulated. Components of the ubiquitin protein ligase system such as *skr-9*, *skr-14*, *ubr-4* were upregulated together with some proteases *cpr-9*, *asp-5*, *asp-6* and *ctsa-1.2*. Chaperones were not altered, besides *dnj-23* and two predicted extracellular regulators of protein aggregation C36C5.5 and *ule-1.*

The list of upregulated DEPs and DEGs only partially overlapped (Fig. 3.17). Transcript and protein levels correlated for 13 hits (i.e. *C01G6.3, cht-1, his-24, asp-6, clec-63, clec-65, clec-85, asp-5, lec-10, igcm-3, cav-1, hil-2, hmg-1.1*). *Clec* genes encode for C-type lectins.

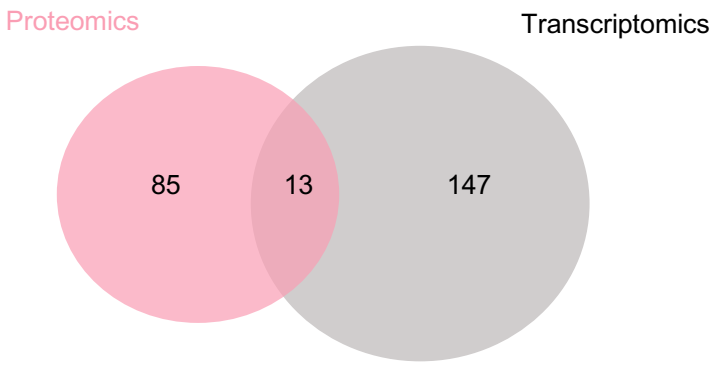

Figure 3. 17: Venn diagram of the upregulated DEPs and DEGs in nAβ day 4

The number of upregulated DEPs from the proteomic analysis are reported in the pink circle while upregulated DEGs from transcriptomic analysis in the grey circle. Common hits are shared between the two circles.

The 61 downregulated DEPs found for nAβ on day 4, were subjected to GO to determine the overrepresented biological processes (Table 3.3). Biological processes related to the metabolism were enriched.

Table 3. 3: GO analysis for downregulated DEPs in nAβ day 4

List of GO terms for biological process and their ID with an FDR < 0.05. Redundant terms (cut-off 0.5) were removed.

Term ID and description	Genes	Gene count	Background genes	FDR
GO:0044281_Small molecule metabolic process	*gspd-1|mtrr-1|ivd-1|C05C8.7|mel-32|mthf-1|cyp-35C1|oatr-1|ampd-1|atic-1|pyr-1|acox-1.2|dhs-25|hach-1|ddo-2|F25B5.6|sur-5|dao-3|asns-2|R102.4|pck-2|kat-1|T07D3.9|W02H5.8|Y62E10A.13*	25	763	1.93E-16
GO:1901605_Alpha-amino acid metabolic process	*mtrr-1|ivd-1|mel-32|mthf-1|oatr-1|pyr-1|hach-1|ddo-2|asns-2|R102.4|Y62E10A.13*	11	130	3.00E-10
GO:0044282_Small molecule catabolic process	*ivd-1|mel-32|oatr-1|acox-1.2|hach-1|ddo-2|R102.4|pck-2|kat-1|W02H5.8*	10	180	7.13E-08
GO:0006760_Folic acid-containing compound metabolic process	*mel-32|mthf-1|F25B5.6|dao-3*	4	9	1.36E-05
GO:0009066_Aspartate family amino acid metabolic process	*mtrr-1|mthf-1|ddo-2|asns-2|R102.4*	5	30	1.44E-05
GO:0009070_Serine family amino acid biosynthetic process	*mel-32|R102.4|Y62E10A.13*	3	21	0.0076
GO:0009156_Ribonucleoside monophosphate biosynthetic process	*ampd-1|atic-1|pyr-1*	3	22	0.0083
GO:0018130_Heterocycle biosynthetic process	*C05C8.7|mel-32|oatr-1|ampd-1|atic-1|pyr-1|F25B5.6*	7	349	0.0116
GO:0043648_Dicarboxylic acid metabolic process	*mel-32|oatr-1|ddo-2*	3	28	0.0141
GO:0009064_Glutamine family amino acid metabolic process	*oatr-1|pyr-1|asns-2*	3	30	0.0158
GO:0006631_Fatty acid metabolic process	*acox-1.2|dhs-25|sur-5|pck-2|kat-1*	5	162	0.0159
GO:0006071_Glycerol metabolic process	*pck-2|W02H5.8*	2	9	0.0472

The 50 most downregulated DEPs were annotated (Table 3.4).

Table 3. 4: 50 most downregulated DEPs in nAβ day 4

List of the 50 most downregulated DEPs in nAβ day 4 ranked according to their FDR value. The gene name and the Uniprot ID are given for each DEP. In addition, each DEP was annotated with a short description and known human homologs.

	Gene	Protein Uniprot ID	Description	Human homologs	FDR
1	*anmt-2*	Q20308	Predicted N-methyltransferase activity	Indolethylamine/phenylethanolamine/ nicotinamide N-methyltransferase (INMT, PNMT, NNMT)	6.91E-11
2	*CELE_F33H2.6*	O62216	Predicted microtubule binding, mitochondrion	Regulator of microtubule dynamics 1 (RMDN1)	5.28E-10
3	*sur-5*	Q21166	Predicted acetoacetyl-CoA synthetase, fatty acid metabolic process.	Acetoacetyl-CoA synthetase (AACS)	9.48E-10
4	*CELE_Y37E11B.5*	Q9TYN2	Predicted tRNA-dihydrouridine synthase	Dihydrouridine synthase 3 like (DUS3L)	5.62E-07
5	*eppl-1*	P91408	Ethanolamine-phosphate phospho-lyase homolog 1	Ethanolamine-phosphate phospho-lyase (ETNPPL), 5-phosphohydroxy-L-lysine phospho-lyase (PHYKPL)	7.23E-07
6	*ampd-1*	A0A2C9C377	Predicted AMP deaminase	Adenosine monophosphate deaminase (AMPD1/2/3)	9.91E-07
7	*pck-2*	O02286	Predicted phosphoenolpyruvate carboxykinase, gluconeogenesis	Phosphoenolpyruvate carboxykinase (PCK1/2)	1.74E-06
8	*atic-1*	Q95QQ4	Predicted purine biosyntehsis protein	5-aminoimidazole-4-carboxamide ribonucleotide formyltransferase/IMP cyclohydrolase (ATIC)	3.96E-06
9	*fkb-5*	P91180	Peptidyl-prolyl cis-trans isomerase	FKBP prolyl isomerase (FKBP9/10/11)	6.93E-06

10	*ivd-1*	G5EEH6	Predicted isovaleryl-CoA dehydrogenase, mitochondrion	Isovaleryl-CoA dehydrogenase (IVD)	1.38E-05
11	*dao-3*	Q21285	Predicted methenyltetrahydrofolate cyclohydrolase/ dehydrogenase (NADP+)	Methylenetetrahydrofolate dehydrogenase (NADP+ dependent) (MTHFD1/2)	1.82E-05
12	*C30G12.2*	Q09486	Predicted oxidoreductase		2.32E-05
13	*CELE_F21C10.9*	Q19661	Predicted acyltransferase		3.66E-05
14	*CELE_T07D3.9*	H2L0J4	Predicted acyl-CoA hydrolase, mitochondrion	Acyl-CoA thioesterase 9 (ACOT9)	6.21E-05
15	*set-18*	Q8I4F7	histone H3K36 methyltransferase activity, predicted chromatin remodeling	SET and MYND domain (SMYD1/2/3)	8.41E-05
16	*CELE_F21D5.3*	Q19687	Predicted oxidoreductase		1.15E-04
17	*gspd-1*	Q27464	Predicted glucose-6-phosphate dehydrogenase, glucose metabolic process	Glucose-6-phosphate dehydrogenase (G6PD)	1.50E-04
18	*hach-1*	Q19278	Predicted 3-hydroxyisobutyryl-CoA hydrolase involved in valine catabolic process, mitochondrion	3-hydroxyisobutyryl-CoA hydrolase (HIBCH)	1.72E-04
19	*CELE_Y62E10A.13*	A0A061ACH4	Predicted to be involved in L-serine biosynthetic process and dephosphorylation	Phosphoserine phosphatase (PSPH)	1.90E-04
20	*sqrd-1*	C6KRP5	Predicted sulfide quinone oxidoreductase, mitochondrion	Sulfide quinone oxidoreductase (SQOR)	2.73E-04

21	*gfm-1*	Q9XV52	Predicted mitochondrial elongation factor G1	G elongation factor mitochondrial (GFM1/2)	2.89E-04
22	*C29F7.2*	O17621	Predicted kinase		7.42E-04
23	*alh-5*	O44555	Predicted aldehyde dehydrogenase	Aldehyde dehydrogenase 3 (ALDH3A1/A2/B1/B2)	7.42E-04
24	*CELE_Y47G6A.22*	Q8MXS8	Predicted oxidoreductase	Hydroxysteroid 17-beta dehydrogenase 14 (HSD17B14)	1.08E-03
25	*F25B5.6*	Q09509	Predicted tetrahydrofolylpolyglutamate synthase	Folylpolyglutamate synthase (FPGS)	1.15E-03
26	*R102.4*	Q21890	Predicted aldolase, involved in glycine biosynthesis and threonine catabolism		1.15E-03
27	*CELE_F17A9.4*	O16214	Predicted oxidoreductase		1.16E-03
28	*CELE_Y56A3A.7*	A7DTF5	Predicted DNA binding activity		1.28E-03
29	*CELE_T25G3.3*	Q22792	Predicted to be involved in ribosomal large subunit export from nucleus	NMD3 ribosome export adaptor (NMD3)	1.81E-03
30	*acox-1.2*	O62137	Predicted acyl-CoA oxidase activity, peroxisome	Acyl-CoA oxidase 1 (ACOX1)	1.87E-03
31	*ugt-21*	A0A061AKV1	Predicted UDP-glycosyltransferase	UDP glucuronosyltransferase (UGT1/2/3)	2.35E-03
32	*dhs-25*	Q19246	Dehydrogenase	Hydroxysteroid 17-beta dehydrogenase (HSD17B8)	2.61E-03
33	*C45E5.1*	Q18645	Predicted phosphatase	Pyridoxal phosphatase (PDCP), phosphoglycolate phosphatase (PGP)	2.61E-03
34	*CELE_Y57A10A.26*	Q9NA74	Uncharacterized protein	Failed axon connections homolog (FAXC)	2.98E-03
35	*cyp-35c1*	G5ECD0	Cytochrome P450	cytochrome P450 (CYP2A7P1/2)	3.11E-03
36	*dbr-1*	Q966M6	Predicted RNA lariat debranching	Debranching RNA lariats (DBR1)	3.13E-03

			enzyme, involved in mRNA splicing via spliceosome		
37	*col-42*	Q8I4C0	Putative cuticle collagen	Macrophage receptor with collagenous structure (MARCO)	3.27E-03
38	*tag-297*	G5EFR0	Uncharacterized protein		3.63E-03
39	*ttr-31*	Q93805	Transthyretin-related family domain		4.06E-03
40	*srdh-1*	Q21080	Predicted L-serine and L-threonine ammonia-lyase		4.37E-03
41	*kat-1*	Q22100	Predicted acetyl-CoA C-acetyltransferase, involved in fatty acid beta-oxidation, mitoxhondrion	Acetyl-CoA acetyltransferase (ACAT1/2), acetyl-CoA acyltransferase (ACAA2)	5.29E-03
42	*CELE_F20G2.3*	Q93546	Uncharacterized protein		5.51E-03
43	*CELE_T03F7.7*	Q8I4G3	Uncharacterized protein		5.76E-03
44	*asns-2*	Q21463	Predicted asparagine synthase	Asparagine synthetase (ASNS)	6.49E-03
45	*tpa-1*	P34722	Protein kinase involved in several processes	protein kinase C (PRKCD/Q)	7.72E-03
46	*tin-13*	O45319	Predicted to be involved in protein insertion into mitochondrial inner membrane	Translocase of inner mitochondrial membrane (TIMM13)	9.11E-03
47	*fkb-3*	O16309	Predicted peptidyl-prolyl cis-trans isomerase	FKBP prolyl isomerase (FKBP9/10/11)	9.49E-03
48	*C05C8.7*	O16315	Predicted mannose-6-phosphate isomerase	Mannose phosphate isomerase (MPI)	9.87E-03
49	*CELE_W02H5.8*	Q9N5C4	Predicted glycerone kinase	Triokinase and FMN cyclase (TKFC)	1.18E-02
50	*hex-3*	G5EDG9	beta-N-acetylhexosaminidase involved in	Hexosaminidase D (HEXD)	1.28E-02

			polysaccharide metabolic process		

A metabolic dysregulation was detected related to amino acid, glucose, ribonucleoside monophosphate and lipid processes. Human homologs of *anmt-2* and *pck-2* were annotated to be involved in Alzheimer´s disease according to WormBase. Interestingly, also a histone modifier such as the histone methyltransferase *set-18* was downregulated.

The list of downregulated DEPs and DEGs only minimally overlapped (Fig. 3.18). Transcript and protein levels correlated for 3 hits (*pck-2*, *kat-1*, *asns-2*). The *pck-2* gene is predicted to be involved in carbohydrate biosynthesis while *asns-2* is predicted to be an asparagine synthetase. The *kat-1* gene is predicted to be involved in fatty acid oxidation and is located in mitochondria.

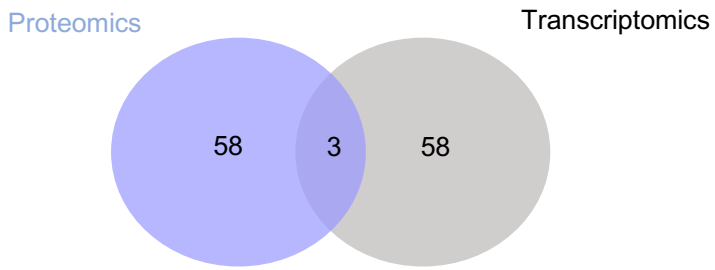

Figure 3. 18: Venn diagram of the downregulated DEPs and DEGs in nAβ day 4

The number of downregulated DEPs from the proteomic analysis are reported in the blue circle while downregulated DEGs from transcriptomic analysis in the grey circle. Common hits are shared between the two circles.

3.3.2 Proteomic analysis of neuronal Aβ$_{1-42}$ *C. elegans* on day 8

The 101 upregulated DEPs found for nAβ on day 8 were subjected to GO to determine the overrepresented biological processes (Table 3.5). Interestingly, biological processes related to chromatin, mRNA and nuclear envelope GO terms were enriched.

Table 3. 5: GO analysis for upregulated DEPs in nAβ day 8

List of GO terms for biological process and their ID with an FDR < 0.05.

Term ID and description	Genes	Gene count	Background genes	FDR
GO:0031497_Chromatin assembly	*his-48|hil-4|ifp-1|his-24|ifc-2|ifd-1|hil-2*	7	51	8.48E-05
GO:0000398_mRNA splicing, via spliceosome	*rsp-8|rsp-6|rsp-4|rnp-5|rsp-2|rsp-1|rsp-3*	7	131	0.0165
GO:0006334_Nucleosome assembly	*his-48|hil-4|his-24|hil-2*	4	24	0.0165
GO:0006397_mRNA processing	*rsp-8|rsp-6|rsp-4|rsr-1|rnp-5|rsp-2|rsp-1|rsp-3*	8	219	0.0169
GO:0006998_Nuclear envelope organization	*ifp-1|ifc-2|ifd-1|oma-2*	4	31	0.019
GO:0045910_Negative regulation of DNA recombination	*hil-4|his-24|hil-2*	3	13	0.0328
GO:0048024_Regulation of mRNA splicing, via spliceosome	*rsp-8|rsp-4|rsr-1|rsp-1*	4	43	0.0412
GO:0051664_Nuclear pore localization	*ifp-1|ifc-2|ifd-1*	3	15	0.0412

The 50 most upregulated DEPs were annotated (Table 3.6).

Table 3. 6: 50 most upregulated DEPs in nAβ day 8

List of the 50 most upregulated DEPs in nAβ day 8 ranked according to their FDR value. The gene name and the Uniprot ID are given for each DEP. In addition, each DEP was annotated with a short description and known human homologs.

	Gene	**Protein Uniprot ID**	**Description**	**Human homologs**	**FDR**
1	*CELE_F07B7.2*	G5ECF6	Uncharacterized protein		2.80E-14
2	*CELE_ZK105.1*	Q965Z4	Uncharacterized protein		7.24E-09
3	*C36C5.5*	O16405	Predicted extracellular holdase		5.06E-07
4	*his-24*	P10771	Histone 24	Histone (H1.0, H1.4, H1.5)	1.62E-06
5	*perm-2*	O44145	Permeable eggshell, structural integrity of oocytes and embryonic eggshell		1.62E-06
6	*nlt-1*	Q23655	Predicted lipid binding activity	SCP2 sterol binding domain containing 1 (SCP2D1), hydroxysteroid 17-beta dehydrogenase 4 (HSD17B4)	3.88E-06
7	*pdpr-1*	Q9U300	Predicted oxidoreductase activity, mitochondrion	Pyruvate dehydrogenase phosphatase regulatory subunit (PDPR)	4.12E-06
8	*acox-1.5*	P34355	Predicted acyl-CoA oxidase activity, peroxisome	Acyl-CoA oxidase 1 (ACOX1)	4.62E-06
9	*clec-190*	Q9NAP0	Uncharacterized protein, predicted C-type Lectin		6.54E-06
10	*ubr-4*	A0A0S4XR36	Uncharacterized protein, predicted UBR E3 ubiquitin ligase homolog	Ubiquitin protein ligase E3 component n-recognin 4 (UBR4)	1.01E-05

11	*pas-3*	Q9N599	Proteasome Alpha Subunit	Proteasome 20S subunit alpha 4 (PSMA4)	1.57E-05
12	*tep-1*	O46015	Thiolester containing protein, predicted endopeptidase inhibitor	Glycosyl phosphatidylinositol (GPI)-linked glycoprotein (CD109), negative signaling regulator	1.79E-05
13	*perm-4*	O44144	Permeable eggshell, structural integrity of oocytes and embryonic eggshell		1.79E-05
14	*CELE_T21H3.1*	H2KZV5	Predicted to be involved in lipid metabolic process		2.12E-05
15	*his-48*	Q27876	Histone 48	Histone (H2B)	6.71E-05
16	*timp-1*	Q21267	Predicted metalloendopeptidase inhibitor	Metallopeptidase inhibitor 2 (TIMP2)	7.14E-05
17	*mob-2*	F5GUA6	Predicted protein kinase activator, involved in signal transduction	MOB kinase activator 2 (MOB2)	7.71E-05
18	*CELE_ZK180.6*	Q23447	Uncharacterized protein		8.81E-05
19	*rsp-8*	Q9XTZ2	SR Protein (splicing factor), predicted to be involved in mRNA splicing	RNA binding protein (CIRBP, RBM3, RBMX, RBMY), transformer 2 alpha homolog (TRA2A/B)	1.87E-04
20	*tag-65*	G5ED97	Predicted to be involved in intracellular calcium ion homeostasis	Calcium homeostasis endoplasmic reticulum protein (CHERP)	1.94E-04
21	*grd-6*	A0A3P6MY87	Ground-like domain-containing protein		2.17E-04
22	*CELE_Y62H9A.4*	Q9XWT4	Uncharacterized protein		2.38E-04
23	*CELE_T09B4.5*	O02155	Uncharacterized protein		3.14E-04
24	*far-6*	Q9XUB7	Fatty acid/retinol binding protein, predicted lipid binding activity		5.77E-04

25	*CELE_D1054.10*	Q18943	Uncharacterized protein		5.91E-04
26	*cbd-1*	O45599	Predicted chitin binding, involved in eggshell formation		7.82E-04
27	*rsp-3*	Q9NEW6	SR Protein (splicing factor), predicted to be involved in splicing	Serine and arginine rich splicing factor (SRSF1/9)	8.79E-04
28	*rsp-1*	Q23121	SR Protein (splicing factor), predicted to be involved in splicing	Serine and arginine rich splicing factor (SRSF4/5/6)	8.79E-04
29	*ifd-1*	Q86DC6	Intermediate filament D	Lamin B2 (LMNB2)	1.14E-03
30	*let-2*	P17140	Alpha-2 type IV collagen, extracellular matrix structural constituent	Collagen (COL1A/2A/3A/4A)	1.15E-03
31	*nas-11*	Q21432	Predicted metalloendopeptidase		1.52E-03
32	*pcp-5*	P34676	Prolyl Carboxy Peptidase	Prolylcarboxypeptidase (PRCP), dipeptidyl peptidase 7 (DPP7)	1.56E-03
33	*B0513.4*	O45227	Uncharacterized protein		1.60E-03
34	*emb-9*	P17139	alpha-1 chain of Type IV basement membrane collagen	Collagen (COL1A/2A/3A/4A)	1.93E-03
35	*ule-5*	Q9XWT3	Uncharacterized protein		2.25E-03
36	*pde-6*	Q9N2V9	Phosphodiesterase	Phosphodiesterase 8 (PDE8A/B)	2.28E-03
37	*rnh-1.0*	Q21024	RNase H ribonuclease\	Ribonuclease H1 (RNASEH1)	2.28E-03
38	*rsr-1*	O62185	Predicted to be part of spliceosomal complex	Serine and arginine repetitive matrix (SRRM1)	2.35E-03
39	*ifc-2*	A0A5E4LYE2	Intermediate filament C	Lamin B2 (LMNB2)	3.20E-03
40	*pqn-52*	G4SL51	Predicted glutamine/asparagine rich protein		3.48E-03

41	*CELE_F40F8.5*	H2L296	Uncharacterized protein		3.53E-03
42	*pmp-1*	Q18597	Predicted ATP-binding cassette (ABC) transporter, peroxisome	ATP binding cassette subfamily D (ABCD1/2/3/4)	3.75E-03
43	*CELE_W09G12.7*	O45198	Uncharacterized protein		4.00E-03
44	*CELE_T28A11.2*	A5HU97	Uncharacterized protein		4.44E-03
45	*F13E6.1*	P55326	Uncharacterized protein	Tumor protein D52 (TPD52)	6.61E-03
46	*grsp-4*	P91207	Glycine rich secreted protein		6.94E-03
47	*hmg-1.1*	G5EFV4	Predicted transcription cis-regulatory region binding activity	High mobility group box (HMGB1/2/3/4)	7.83E-03
48	*his-2*	P08898	Histone	H3 histone (H3C)	9.02E-03
49	*nlp-29*	O44664	Neuropeptide-like protein		9.27E-03
50	*pgp-3*	P34713	P-Glycoprotein related	ATP binding cassette subfamily B (ABCB1/4/5/11)	9.52E-03

As for day 4, histones (i.e. *his-48, his-24, his-2, htz-1, his-71, hil-2* and *hil-4*) were found to be highly upregulated. Components of the proteasome and the ubiquitin protein ligase system (i.e. *pas-3* and *ubr-4*) were also upregulated. Chaperones were not altered besides two predicted extracellular regulators of protein aggregation (C36C5.5 and *ule-1*).

Conversely to day 4, proteases (i.e. *cpr-9*, *asp-5*, *asp-6* and *ctsa-1.2*.) were not upregulated besides *pcp-5*. Moreover, a predicted protease inhibitor *timp-1* was upregulated, this gene was also associated with Alzheimer´s disease by WormBase. Interestingly, the *nlp-29* gene encoding for a neuropeptide-like protein is upregulated and chaperone levels were unchanged.

The list of upregulated DEPs and DEGs did not overlap (Fig. 3.19).

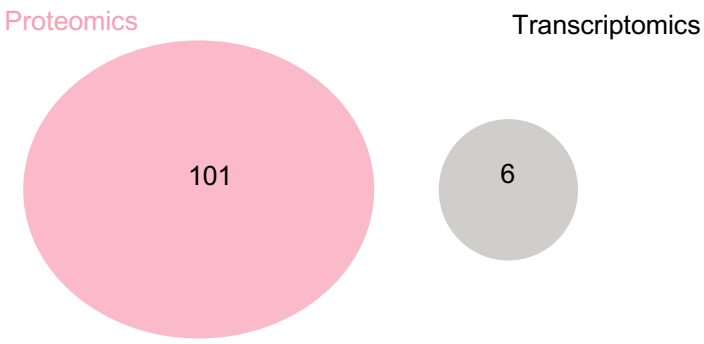

Figure 3. 19: Venn diagram of the upregulated DEPs and DEGs in nAβ day 8

The number of upregulated DEPs from the proteomic analysis are reported in the pink circle while upregulated DEGs from transcriptomic analysis in the grey circle. No hits are shared between the two circles.

The 31 downregulated DEPs found for nAβ on day 8 were subjected to GO to determine the overrepresented biological processes (Table 3.7). Biological processes related to metabolic GO terms were enriched.

Table 3. 7: GO analysis for downregulated DEPs in nAβ day 8

List of GO terms for biological process and their ID with an FDR < 0.05.

Term ID and description	Genes	Gene count	Background genes	FDR
GO:0006082_Organic acid metabolic process	*cyp-35C1|ard-1|fat-7|sur-5|R102.4|pck-2|men-1|Y62E10A.13*	8	448	0.0013
GO:0044281_Small molecule metabolic process	*cyp-35C1|atic-1|ard-1|fat-7|sur-5|R102.4|pck-2|men-1|Y62E10A.13*	9	763	0.0032
GO:0008152_Metabolic process	*cyp-35C1|nuc-1|C45E5.1|atic-1|aagr-1|ard-1|sqrd-1|fat-7|anmt-2|sur-5|lea-1|R102.4|pck-2|map-2|Y37E11B.5|men-1|gst-29|Y62E10A.13|pmt-1*	19	4551	0.0037
GO:0019752_Carboxylic acid metabolic process	*ard-1|fat-7|sur-5|R102.4|pck-2|men-1|Y62E10A.13*	7	408	0.0037
GO:0032787_Monocarboxylic acid metabolic process	*ard-1|fat-7|sur-5|pck-2|men-1*	5	214	0.0153

GO:0044237_Cellular metabolic process	*cyp-35C1|nuc-1|C45E5.1|atic-1|aagr-1|ard-1|sqrd-1|fat-7|sur-5|R102.4|pck-2|Y37E11B.5|men-1|gst-29|Y62E10A.13|pmt-1*	16	3704	0.0153

The 31 downregulated DEPs were annotated (Table 3.8).

Table 3. 8: 31 downregulated DEPs in nAβ day 8

List of the 31 downregulated DEPs in nAβ day 8 ranked according to their FDR value. The gene name and the Uniprot ID are given for each DEP. In addition, each DEP was annotated with a short description and known human homologs.

	Gene	**Protein Uniprot ID**	**Description**	**Human homologs**	**FDR**
1	*anmt-2*	Q20308	Predicted N-methyltransferase activity	Indolethylamine/phenylethanolamine/nicotinamide N-methyltransferase (INMT, PNMT, NNMT)	3.24E-15
2	*CELE_F33H2.6*	O62216	Predicted microtubule binding, mitochondrion	Regulator of microtubule dynamics 1 (RMDN1)	4.80E-08
3	*lea-1*	H2FLK8	Predicted lipid binding activity	Perilipin 4 (PLIN4)	5.06E-07
4	*pck-2*	O02286	Predicted phosphoenolpyruvate carboxykinase, gluconeogenesis	Phosphoenolpyruvate carboxykinase (PCK1/2)	2.28E-05
5	*CELE_H06H21.8*	Q7YXH1	Predicted kinase		2.76E-05
6	*CELE_Y62E10A.13*	A0A061ACH4	Predicted to be involved in L-serine biosynthetic process and dephosphorylation	Phosphoserine phosphatase (PSPH)	5.17E-05
7	*atic-1*	Q95QQ4	Predicted purine biosyntehsis protein	5-aminoimidazole-4-carboxamide ribonucleotide formyltransferase/IMP cyclohydrolase (ATIC)	6.44E-05
8	*mmaa-1*	Q22111	Predicted to enable GTPase activity	Metabolism of cobalamin (Vitamin B12) associated A (MMAA)	6.52E-05

9	*R102.4*	Q21890	Predicted aldolase, involved in glycine biosynthesis and threonine catabolism		6.58E-05
10	*CELE_Y37E11B.5*	Q9TYN2	Predicted tRNA-dihydrouridine synthase	Dihydrouridine synthase 3 like (DUS3L)	1.61E-04
11	*ard-1*	Q19102	Predicted alcohol/Ribitol Dehydrogenase	Hydroxysteroid 17-beta dehydrogenase 10 (HSD17B10)	2.20E-04
12	*pmt-1*	Q23552	Phosphoethanolamine N-methyltransferase 1		3.20E-04
13	*brp-1*	I2HAF5	Bypass of Response to Pheromone		9.72E-04
14	*sur-5*	Q21166	Predicted acetoacetyl-CoA synthetase, fatty acid metabolic process.	Acetoacetyl-CoA synthetase (AACS)	9.72E-04
15	*map-2*	H1UBK1	Methionine aminopeptidase	Methionyl aminopeptidase 2 (METAP2)	1.18E-03
16	*sqrd-1*	C6KRP5	Predicted sulfide quinone oxidoreductase, mitochondrion	Sulfide quinone oxidoreductase (SQOR)	1.52E-03
17	*cyp-25a2*	Q27476	Cytochrome P450 family	Cytochrome P450 (CYP3A4/A5/A7, CYP4B1/V2/A22)	1.85E-03
18	*fat-7*	G5EGH6	Fatty acid desaturase	Stearoyl-CoA desaturase (SCD)	1.85E-03
19	*C30G12.2*	Q09486	Predicted oxidoreductase		2.03E-03
20	*Y39A3CL.4*	A0A8S4QCF9	Uncharacterized protein		8.46E-03
21	*gst-29*	Q9NAB1	Uncharacterized protein, predicted to encode Glutathione S-transferase domain	Gutathione S-transferase (GSTA/T	8.46E-03
22	*men-1*	Q9U296	Predicted malate dehydrogenase	Malic enzyme (ME1/2/3)	1.32E-02
23	*CELE_T03F7.7*	Q8I4G3	Uncharacterized protein		1.33E-02

24	*CELE_F21C10.9*	Q19661	Predicted acyltransferase		1.37E-02
25	*nuc-1*	Q17778	Deoxyribonuclease II	Deoxyribonuclease 2 (DNASE2)	2.18E-02
26	*C45E5.1*	Q18645	Predicted phosphatase	Pyridoxal phosphatase (PDCP), phosphoglycolate phosphatase (PGP)	2.48E-02
27	*ttr-31*	Q93805	Transthyretin-related family domain		3.37E-02
28	*cua-1*	G5ED40	Copper ion transmembrane transporter	ATPase copper transporting (ATP7A/B)	3.43E-02
29	*semo-1*	Q9XXF9	Methanethiol oxidase	Selenium binding protein (SELENBP1)	3.78E-02
30	*cyp-35c1*	G5ECD0	Cytochrome P450	Cytochrome P450 (CYP2A7P1/2)	4.30E-02
31	*aagr-1*	Q19004	Alpha-1,4-glucosidase	Maltase-glucoamylase (MGAM), alpha glucosidase (GAA)	4.50E-02

As for day 4, a metabolic dysregulation was detected. Human homologs of *anmt-2*, *pck-2* and *ard-1* were annotated to be involved in Alzheimer´s disease according to WormBase.

The list of downregulated DEPs and DEGs only overlapped for C30G12.2 (Fig. 3.20).

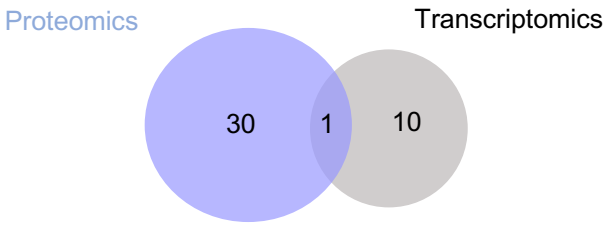

Figure 3. 20: Venn diagram of the downregulated DEPs and DEGs in nAβ day 8

The number of downregulated DEPs from the proteomic analysis are reported in the blue circle while downregulated DEGs from transcriptomic analysis in the grey circle. Common hits are shared between the two circles.

3.3.3 Proteomic analysis of muscle Aβ$_{1-42}$ *C. elegans* on day 4

The 74 upregulated DEPs found for mAβ on day 4 were subjected to GO to determine the overrepresented biological processes (Table 3.9). Biological processes related to unfolded protein response and protein refolding GO terms were enriched.

Table 3. 9: GO analysis for upregulated DEPs in mAβ day 4

List of GO terms for biological process and their ID with an FDR < 0.05.

Term ID and description	Genes	Gene count	Background genes	FDR
GO:0030968_Endoplasmic reticulum unfolded protein response	*C04F12.1|cht-1|catp-3|lec-8|tbb-6|T20D4.7|hsp-16.48|hsp-16.1|hsp-16.41*	9	163	7.24E-05
GO:0042026_Protein refolding	*hsp-43|hsp-16.48|hsp-16.1|hsp-16.41|hsp-16.2*	5	27	1.20E-04
GO:0071310_Cellular response to organic substance	*C04F12.1|cht-1|catp-3|rap-1|lec-8|tbb-6|T20D4.7|hsp-16.48|hsp-16.1|hsp-16.41*	10	327	2.80E-04
GO:0036498_IRE1-mediated unfolded protein response	*C04F12.1|catp-3|lec-8|hsp-16.48|hsp-16.1|hsp-16.41*	6	119	0.0036
GO:0006950_Response to stress	*his-48|lys-7|C04F12.1|cht-1|catp-3|hsp-43|F53C11.1|spt-16|lec-8|tbb-6|T20D4.7|hsp-16.48|hsp-16.1|hsp-16.41|hsp-16.2*	15	1131	0.0064
GO:0009408_Response to heat	*hsp-43|hsp-16.48|hsp-16.1|hsp-16.41|hsp-16.2*	5	77	0.0064
GO:0033554_Cellular response to stress	*C04F12.1|cht-1|catp-3|spt-16|lec-8|tbb-6|T20D4.7|hsp-16.48|hsp-16.1|hsp-16.41*	10	560	0.0165

The 50 most upregulated DEPs were annotated (Table 3.10).

Table 3. 10: 50 most upregulated DEPs in mAβ day 4

List of the 50 most upregulated DEPs in mAβ day 4 ranked according to their FDR value. The gene name and the Uniprot ID are given for each DEP. In addition, each DEP was annotated with a short description and known human homologs.

	Gene	**Protein Uniprot ID**	**Description**	**Human homologs**	**FDR**
1	*hsp-16.48*	P02513	Heat shock protein Hsp-16.48	Small HSP (HSPB1/2/3/6/8)	6.11E-24
2	*CELE_F07B7.2*	G5ECF6	Uncharacterized protein		5.22E-23
3	*hsp-16.41*	P06581	Heat shock protein Hsp-16.41	Small HSP (HSPB1/2/3/6/8)	5.89E-23
4	*hsp-16.2*	P06582	Heat shock protein hsp-16.2	Small HSP (HSPB1/2/3/6/8)	2.57E-18
5	*hsp-16.1*	P34696	Heat shock protein Hsp-16.1	Small HSP (HSPB1/2/3/6/8)	2.89E-18
6	*tbb-6*	G5EF01	Tubulin beta chain	Tubulin beta (TUBB3/6/8)	2.55E-09
7	*sur-5*	Q21166	Predicted acetoacetyl-CoA synthetase, fatty acid metabolic process.	acetoacetyl-CoA synthetase (AACS)	7.00E-09
8	*hsp-43*	H2KYS1	Heat shock protein Hsp-43	Small HSP (HSPB1/2/3/6/8)	1.28E-08
9	*cht-1*	Q11174	Predicted endochitinase	Chitinase (CHIT1, CHIA, CHI3L2, CHI3L1, OVGP1)	1.02E-07
10	*dig-1*	Q09165	Mesocentin (maintain axons and cell bodies in place)	Mucin 16, cell surface associated (MUC16)	2.08E-07
11	*C01G6.3*	Q17572	Uncharacterized protein		2.59E-07
12	*sto-1*	Q19200	Stomatin-1	Stomatin (STOM, STOML2, STOML3, NPHS2)	2.11E-06
13	*cex-1*	Q10131	Calexcitin-1, predicted metal ion binding		2.23E-06

14	*C04F12.1*	Q9XVF1	Piwi domain-containing protein, predicted RNA endonuclease activity		3.37E-06
15	*CELE_T20D4.7*	P91468	Involved in unfolded protein response	Nucleoredoxin like (NXNL2)	4.86E-06
16	*CELE_Y94H6A.10*	Q75MI6	Uncharacterized protein, predicted peptidase		5.02E-06
17	*CELE_T03F1.11*	P91423	EF-hand domain-containing protein, predicted calcium binding		1.24E-05
18	*icp-1*	G5EE37	InCenP homolog, serine/threonine kinase activator, involved in nuclear division	Inner centromere protein (INCENP)	2.47E-05
19	*igcm-3*	A0A8S4Q9R2	ImmunoGlobulin-like Cell adhesion Molecule family		2.74E-05
20	*CELE_W09G12.7*	O45198	Uncharacterized protein		4.10E-05
21	*C27B7.9*	Q7YTR9	Uncharacterized protein		4.50E-05
22	*CELE_T09B4.5*	O02155	Uncharacterized protein		4.92E-05
23	*sqst-1*	Q22436	Sequestosome	Sequestosome 1 (SQSTM1/p62)	8.12E-05
24	*his-24*	P10771	Histone 24	Histone (H1.0, H1.4, H1.5)	1.08E-04
25	*efhd-1*	Q9U2A6	Predicted calcium binding protein	EF-hand domain family member (EFHD1, EFHD2)	1.10E-04
26	*csc-1*	O45952	Chromosome segregation and cytokinesis defective protein 1		1.75E-04
27	*CELE_W01F3.2*	O62390	Uncharacterized protein	Matrix metallopeptidase (MMP2/9/23B)	2.14E-04
28	*C32D5.8*	Q09489	Uncharacterized protein	Nucleoredoxin like (NXNL2)	4.34E-04

29	*CELE_Y62H9A.4*	Q9XWT4	Uncharacterized protein		5.36E-04
30	*ule-1*	O01780	Predicted chitin binding protein		1.27E-03
31	*CELE_F48E3.4*	Q9GPA1	Predicted serine-type endopeptidase		1.29E-03
32	*his-48*	Q27876	Histone 48	Histone (H2B)	1.39E-03
33	*catp-3*	O16331	Cation transporting ATPase	ATPase Na+/K+ transporting (ATP1A1/1A2/12A/1A3/1A4)	1.39E-03
34	*ttr-15*	Q22288	Transthyretin-like protein 15		1.50E-03
35	*skr-14*	Q9N3U9	Skp1-related, ubiquitin ligase complex component	S-phase kinase associated protein (SKP1)	1.75E-03
36	*perm-2*	O44145	Permeable eggshell, structural integrity of oocytes and embryonic eggshell		2.23E-03
37	*CELE_ZK822.2*	Q23614	Uncharacterized protein		2.73E-03
38	*lec-6*	Q9N384	Galectin	Galectin (LGALS7/7B/1)	2.96E-03
39	*CELE_Y58A7A.1*	D6RYD3	Predicted copper transport protein		3.10E-03
40	*CELE_T04G9.7*	Q9TXQ6	Uncharacterized protein		3.92E-03
41	*C38D9.2*	Q9XVC4	Uncharacterized protein		4.08E-03
42	*cpi-1*	G5EDZ9	Cysteine protease inhibitor	Cystatin F CST1/2/3/4/5/6/7	5.09E-03
43	*nex-1*	G5EEA8	Annexin, calcium-dependent phospholipid binding protein	Annexin ANXA1/2/3/4/5/6/7/8/9/10/11/13	5.36E-03
44	*tra-3*	Q22036	Cysteine-type endopeptidase activity	Calpain (CAPN5)	5.43E-03
45	*C44B7.5*	Q18594	Uncharacterized protein		6.09E-03
46	*CELE_Y37E11B.5*	Q9TYN2	Predicted tRNA-dihydrouridine synthase	Dihydrouridine synthase 3 like (DUS3L)	6.23E-03

47	*spt-16*	Q9N5R9	Predicted nucleosome binding activity	Chromatin remodeling subunit (SUPT16H)	6.31E-03
48	*lec-8*	Q09610	Glycolipid-binding galectin, host defense response	Galectin 3 (LGALS3)	8.09E-03
49	*CELE_F55B11.3*	O17893	Uncharacterized protein		8.55E-03
50	*CELE_D1054.10*	Q18943	Uncharacterized protein		8.68E-03

Many sHSPs were found to be enriched such as *hsp-16.48, hsp-16.41, hsp-16.2, hsp-16.1* and *hsp-43*. However, chaperones were not altered besides a predicted extracellular regulator of protein aggregation *ule-1.* Human homologs of *hsp-16.2*, *CELE_W01F3.2* and *cpi-1* were annotated to be involved in Alzheimer´s disease by WormBase. A component of the ubiquitin ligase complex *skr-14* and an autophagy marker *sqst-1* were also upregulated. Additionally, predicted or known proteases as *CELE_F48E3.4* and *tra-3* were upregulated as well.

The list of upregulated DEPs and DEGs were overlapped. Four hits (*hsp-43, igcm-3, his-24 and C38D9.2*) were downregulated both in the transcriptomic and in the proteomic analysis (Fig. 3.21).

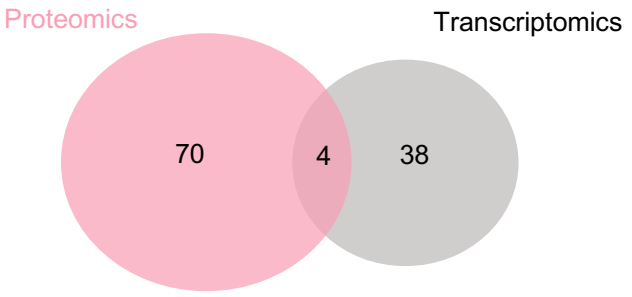

Figure 3. 21: Venn diagram of the upregulated DEPs and DEGs in mAβ day 4

The number of upregulated DEPs from the proteomic analysis are reported in the pink circle while upregulated DEGs from transcriptomic analysis in the grey circle. Common hits are shared between the two circles.

The 70 downregulated DEPs found for mAβ on day 4 were subjected to GO to determine the overrepresented biological processes (Table 3.11). Biological processes related to muscular and metabolic GO terms were enriched.

Table 3. 11: GO analysis for downregulated DEPs in mAβ day 4

List of GO terms for biological process and their ID with an FDR < 0.05.

Term ID and description	Genes	Gene count	Background genes	FDR
GO:0055001_Muscle cell development	*unc-15|unc-54|myo-6|tnt-2|pat-10|myo-5|myo-3|atn-1|unc-27*	9	47	1.36E-09
GO:0006936_Muscle contraction	*unc-54|myo-6|tnt-2|pat-10|myo-5|myo-3|lev-11|unc-27*	8	30	1.52E-09
GO:0061061_Muscle structure development	*unc-15|unc-54|myo-6|tnt-2|pat-10|myo-5|myo-3|alp-1|atn-1|unc-27*	10	95	2.70E-09
GO:0030239_Myofibril assembly	*unc-15|unc-54|myo-6|tnt-2|pat-10|myo-5|myo-3|unc-27*	8	41	4.54E-09
GO:0030036_Actin cytoskeleton organization	*unc-15|unc-54|myo-6|tnt-2|pat-10|myo-5|myo-3|alp-1|atn-1|lev-11|unc-27*	11	172	1.59E-08
GO:0045214_Sarcomere organization	*unc-54|myo-6|tnt-2|myo-5|myo-3|unc-27*	6	24	3.03E-07
GO:0097435_Supramolecular fiber organization	*unc-15|unc-54|myo-6|tnt-2|pat-10|myo-5|myo-3|lev-11|unc-27*	9	150	1.38E-06
GO:0048856_Anatomical structure development	*col-149|col-150|col-113|col-175|unc-15|unc-54|myo-6|tnt-2|pat-10|myo-5|bcat-1|col-49|myo-3|T01G5.1|col-118|alp-1|atn-1|lev-11|unc-27*	19	1641	5.30E-04
GO:0014866_Skeletal myofibril assembly	*unc-15|unc-54|pat-10*	3	8	0.0016
GO:0006082_Organic acid metabolic process	*cyp-35A2|dhs-25|hach-1|ddo-2|bcat-1|pck-2|pck-1|fat-1*	8	448	0.0267
GO:0006574_Valine catabolic process	*hach-1|bcat-1*	2	4	0.0267
GO:0030241_Skeletal muscle myosin thick filament assembly	*unc-15|unc-54*	2	4	0.0267

GO:0046327_Glycerol biosynthetic process from pyruvate	*pck-2|pck-1*	2	3	0.0267
GO:0046395_Carboxylic acid catabolic process	*hach-1|ddo-2|bcat-1|pck-2|pck-1*	5	139	0.0267
GO:0071333_Cellular response to glucose stimulus	*pck-2|pck-1*	2	3	0.0267
GO:0019543_Propionate catabolic process	*pck-2|pck-1*	2	5	0.0335
GO:0033993_Response to lipid	*pck-2|pck-1*	2	5	0.0335
GO:0044283_Small molecule biosynthetic process	*dhs-25|bcat-1|pck-2|pck-1|fat-1*	5	177	0.0491

The 50 most downregulated DEPs were annotated (Table 3.12).

Table 3. 12: 50 most downregulated DEPs in mAβ day 4

List of the 50 most downregulated DEPs in mAβ day 4 ranked according to their FDR value. The gene name and the Uniprot ID are given for each DEP. In addition, each DEP was annotated with a short description and known human homologs.

	Gene	**Protein Uniprot ID**	**Description**	**Human homologs**	**FDR**
1	*ppw-2*	Q9N585	Piwi domain-containing protein, predicted RNA endonuclease activity		9.90E-09
2	*unc-54*	P02566	Myosin	Myosin heavy chain (MYH1/2/3/4/6/7/8)	1.29E-08
3	*unc-15*	P10567	Paramyosin	Myosin heavy chain (MYH1/2/3/6/7/8)	1.39E-07
4	*ctsa-1.1*	P52717	Serine carboxypeptidase	Cathepsin A (CTSA)	1.71E-07
5	*myo-3*	P12844	Myosin	Myosin heavy chain (MYH1/2/3/4/6/7/8)	8.69E-07
6	*CELE_W04E12.7*	G5EE34	Uncharacterized protein		1.93E-06
7	*lev-11*	K8FDX2	Tropomyosin	Tropomyosin (TPM1/2/3/4)	1.94E-06

8	*rips-1*	O01593	Predicted to be involved in methylation		2.11E-06
9	*pck-2*	O02286	Predicted phosphoenolpyruvate carboxykinase, gluconeogenesis	Phosphoenolpyruvate carboxykinase (PCK1/2)	2.12E-06
10	*CELE_F21D5.3*	Q19687	Predicted oxidoreductase		3.07E-06
11	*F46H5.3*	Q10454	Predicted kinase	Creatine kinase B (CKB)	3.16E-06
12	*myo-5*	Q21000	Myosin	Myosin heavy chain (MYH1/2/3/4/6/7/8)	3.37E-06
13	*C46G7.2*	O02141	Uncharacterized protein		3.86E-06
14	*ifg-1*	A0A486WX07	Translation initiation factor 4F	Eukaryotic translation initiation factor (EIF4G1/2/3)	5.90E-06
15	*ctnb-1*	P91401	Catenin Beta like 1, predicted to be part of spliceosomal complex	Catenin beta like 1 (CTNNBL1)	1.25E-05
16	*CELE_F21C10.9*	Q19661	Predicted acyltransferase		2.79E-05
17	*pck-1*	O44906	Predicted phosphoenolpyruvate carboxykinase, gluconeogenesis	Phosphoenolpyruvate carboxykinase (PCK1/2)	2.93E-05
18	*col-79*	Q09233	Putative cuticle collagen	Surfactant protein D (SFTPD)	3.23E-05
19	*col-90*	P34340	Putative cuticle collagen		4.48E-05
20	*Y47G6A.19*	A0A7R9SW65	Predicted metallocarboxypeptidase		4.58E-05
21	*eppl-1*	P91408	Ethanolamine-phosphate phospho-lyase homolog 1	Ethanolamine-phosphate phospho-lyase (ETNPPL), 5-phosphohydroxy-L-lysine phospho-lyase (PHYKPL)	6.69E-05
22	*F44B9.2*	P34423	Uncharacterized protein		1.24E-04

23	*gfm-1*	Q9XV52	Predicted mitochondrial elongation factor G1	G elongation factor mitochondrial (GFM1/2)	1.43E-04
24	*atn-1*	H2L2C9	Actinin	Actinin alpha (ACTN1/2/3/4)	1.67E-04
25	*srp-1*	G5EE40	Serpin, predicted peptidase	Serpin family members (SERPINA/B/C)	1.75E-04
26	*CELE_K08E7.5*	Q21344	Uncharacterized protein		1.98E-04
27	*col-113*	M1ZJS7	Putative cuticle collagen	C1q and TNF related (C1QTNF2/7/9), adiponectin (ADIPOQ), otolin (OTOL1)	2.33E-04
28	*myo-6*	O62244	Myosin	Myosin heavy chain (MYH1/2/3/4/6/7/8)	2.92E-04
29	*tnt-2*	Q7Z072	Predicted tropomyosin	Troponin T (TNNT1/2/3)	3.00E-04
30	*ttr-25*	Q9XXQ6	TransThyretin-Related family domain		3.34E-04
31	*CELE_F25E2.2*	G4SF79	Uncharacterized protein		3.53E-04
32	*col-118*	A5JYR8	Putative cuticle collagen	Surfactant protein D (SFTPD)	4.34E-04
33	*C36C5.5*	O16405	Predicted extracellular holdase		4.69E-04
34	*CELE_T23E7.2*	A0A5E4LWN1	Uncharacterized protein		5.16E-04
35	*ttr-24*	Q9XXR4	TransThyretin-Related family domain		5.36E-04
36	*CELE_F42G10.1*	Q09393	Predicted metalloendopeptidase		6.61E-04
37	*bca-1*	Q22460	Beta carbonic anhydrase 1		7.06E-04
38	*ddo-2*	Q19564	D-aspartate oxidase 2	D-amino acid oxidase (DAO)	9.51E-04
39	*pat-10*	G5EF37	Troponin C	Troponin (TNNC1/2), calmodulin like (CALML6), EF-hand calcium binding domain (EFCAB2)	9.56E-04

40	*col-150*	Q17418	Putative cuticle collagen	Surfactant protein D (SFTPD)	1.29E-03
41	*hach-1*	Q19278	Predicted 3-hydroxyisobutyryl-CoA hydrolase involved in valine catabolic process, mitochondrion	3-hydroxyisobutyryl-CoA hydrolase (HIBCH)	1.29E-03
42	*grd-6*	A0A3P6MY87	Ground-like domain-containing protein		2.57E-03
43	*col-149*	Q17417	Putative cuticle collagen	Surfactant protein D (SFTPD)	2.76E-03
44	*CELE_F20G2.3*	Q93546	Uncharacterized protein		2.77E-03
45	*alp-1*	G5EFL5	Predicted actin binding activity	LIM domain binding (LDB3), PDZ and LIM domain (PDLIM1/5/7)	3.15E-03
46	*dhs-25*	Q19246	Dehydrogenase	Hydroxysteroid 17-beta dehydrogenase (HSD17B8)	4.26E-03
47	*bcat-1*	P54688	Branched-chain-amino acid aminotransferase	Branched chain amino acid transaminase (BCAT1/2)	4.46E-03
48	*tag-18*	Q22508	Uncharacterized protein		4.90E-03
49	*CELE_T01G5.1*	O18008	Protein kinase		4.91E-03
50	*mlc-3*	P53014	Myosin	Myosin heavy chain (MYH1/2/3/4)	4.91E-03

Several genes involved in muscle structure and contraction were downregulated (i.e. *unc-15, unc-54, myo-6, tnt-2, pat-10, myo-5, myo-3, alp-1, atn-1,* and *unc-27*). As for nAβ, a metabolic dysregulation was detected related to amino acid, glucose, and lipid processes. Human homologs of *pck-1* and *pck-2* were annotated to be involved in Alzheimer´s disease in Wormbase. Conversely to nAβ, some predicted or known proteases were downregulated such as *Y47G6A.19, srp-1* and *CELE_F42G10.1*. A predicted extracellular regulator of protein aggregation, C36C5.5, was downregulated.

The list of downregulated DEPs and DEGs overlapped for four hits (*tnt-2, pat-10, csq-1, unc-27*) that were downregulated in both the transcriptomic and in the proteomic analysis (Fig. 3.22).

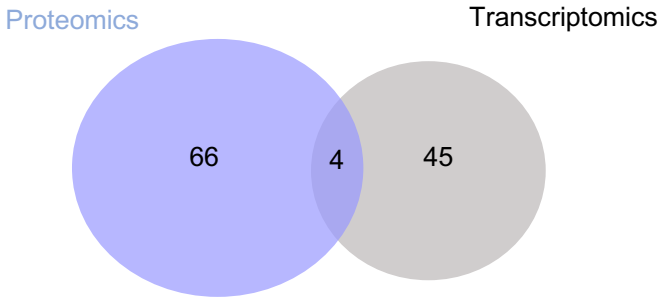

Figure 3. 22: Venn diagram of the downregulated DEPs and DEGs in mAβ day 4

The number of downregulated DEPs from the proteomic analysis are reported in the blue circle while downregulated DEGs from transcriptomic analysis in the grey circle. Common hits are shared between the two circles.

3.3.4 Proteomic analysis of muscle Aβ$_{1-42}$ *C. elegans* on day 8

The 71 upregulated DEPs found for mAβ on day 8 were subjected to GO to determine the overrepresented biological processes (Table 3.13). Biological processes related to unfolded protein response and protein refolding GO terms were enriched.

Table 3. 13: GO analysis for upregulated DEPs in mAβ day 8

List of GO terms for biological process and their ID with an FDR < 0.05.

Term ID and description	Genes	Gene count	Background genes	FDR
GO:0030968_Endoplasmic reticulum unfolded protein response	*C04F12.1|catp-3|tbb-6|T20D4.7|hsp-16.48|hsp-16.1|hsp-16.41*	7	163	0.0116
GO:0042026_Protein refolding	*hsp-16.48|hsp-16.1|hsp-16.41|hsp-16.2*	4	27	0.0116
GO:0036498_IRE1-mediated unfolded protein response	*C04F12.1|catp-3|hsp-16.48|hsp-16.1|hsp-16.41*	5	119	0.0264
GO:0051248_Negative regulation of protein metabolic process	*C25E10.8|swm-1|cri-2|vit-6|K11D12.7|tep-1*	6	197	0.0264

GO:0010033_Response to organic substance	*C04F12.1|catp-3|cri-2|tbb-6|T20D4.7|hsp-16.48|hsp-16.1|hsp-16.41*	8	401	0.0284

The 50 most upregulated DEPs were annotated (Table 3.14).

Table 3. 14: 50 most upregulated DEPs in mAβ day 8

List of the 50 most upregulated DEPs in mAβ day 8 ranked according to their FDR value. The gene name and the Uniprot ID are given for each DEP. In addition, each DEP was annotated with a short description and known human homologs.

	Gene	**Protein Uniprot ID**	**Description**	**Human homologs**	**FDR**
1	*hsp-16.48*	P02513	Heat shock protein Hsp-16.48	Small HSP (HSPB1/2/3/6/8)	2.63E-20
2	*CELE_F07B7.2*	G5ECF6	Uncharacterized protein		8.93E-20
3	*hsp-16.41*	P06581	Heat shock protein Hsp-16.41	Small HSP (HSPB1/2/3/6/8)	8.93E-20
4	*hsp-16.1*	P34696	Heat shock protein Hsp-16.1	Small HSP (HSPB1/2/3/6/8)	8.64E-16
5	*hsp-16.2*	P06582	Heat shock protein hsp-16.2	Small HSP (HSPB1/2/3/6/8)	1.19E-15
6	*CELE_ZK105.1*	Q965Z4	Uncharacterized protein		1.62E-15
7	*tbb-6*	G5EF01	Tubulin beta chain	Tubulin beta (TUBB3/6/8)	2.11E-09
8	*C04F12.1*	Q9XVF1	Piwi domain-containing protein, predicted RNA endonuclease activity		9.60E-09
9	*cex-1*	Q10131	Calexcitin-1, predicted metal ion binding		4.04E-08
10	*sdz-27*	Q93932	SKN-1 Dependent Zygotic		5.69E-08
11	*CELE_Y53H1B.2*	G5EDV7	Uncharacterized protein		6.11E-06
12	*CELE_ZK822.2*	Q23614	Uncharacterized protein		7.09E-06

13	*lys-7*	O16202	Lysozyme		9.96E-06
14	*catp-3*	O16331	Cation transporting ATPase	ATPase Na+/K+ transporting (ATP1A1/1A2/12A/1A3/1A4)	1.02E-05
15	*tep-1*	O46015	Thiolester containing protein, predicted endopeptidase inhibitor	Glycosyl phosphatidylinositol (GPI)-linked glycoprotein (CD109), negative signaling regulator	1.27E-05
16	*lec-5*	G5EFI4	Predicted galectin	Galectin (LGALS3/4/7/8/9	1.92E-05
17	*CELE_Y94H6A.10*	Q75MI6	Uncharacterized protein, predicted peptidase		3.17E-05
18	*CELE_F55B11.2*	O17891	Uncharacterized protein		4.05E-05
19	*CELE_Y57G11B.5*	O18224	Uncharacterized protein		5.00E-05
20	*test-1*	O44466	Predicted calcium ion binding activity	SPARC (osteonectin), cwcv and kazal like domains proteoglycan (SPOCK1/2/3)	1.22E-04
21	*CELE_F52E4.5*	Q20675	Uncharacterized protein		1.22E-04
22	*far-3*	Q19478	Fatty acid/retinol binding protein, predicted lipid binding activity		1.53E-04
23	*cht-3*	Q18143	Predicted chitinase		1.68E-04
24	*CELE_ZK856.7*	Q23642	Uncharacterized protein		1.71E-04
25	*pfn-3*	Q21193	Predicted actin monomer binding activity	Profilin family member 4 (PFN4)	2.25E-04
26	*ttr-24*	Q9XXR4	TransThyretin-Related family domain		2.32E-04
27	*hrg-7*	Q18020	Predicted aspartic-type endopeptidase		2.34E-04
28	*far-1*	P34382	Fatty acid/retinol binding protein, predicted lipid binding activity		2.50E-04

29	*ctsa-1.2*	P52715	Cathepsin A, predicted serine-type carboxypeptidase	Cathepsin A (CTSA)	4.20E-04
30	*pqn-24*	O01876	Predicted glutamine/asparagine rich protein		7.56E-04
31	*let-268*	Q20679	Glucosyltransferase activity	Procollagen-lysine,2-oxoglutarate 5-dioxygenase (PLOD1/2/3)	7.92E-04
32	*C44B7.5*	Q18594	Uncharacterized protein		1.05E-03
33	*brp-1*	I2HAF5	Bypass of Response to Pheromone		2.16E-03
34	*perm-2*	O44145	Permeable eggshell, structural integrity of oocytes and embryonic eggshell		2.43E-03
35	*swm-1*	Q18158	Sperm activation without mating, predicted serine-type endopeptidase inhibitor		2.55E-03
36	*tag-225*	Q21265	Conserved regulator of innate immunity, predicted metalloendopeptidase inhibitor	TIMP metallopeptidase inhibitor (TIMP1/2/4)	3.19E-03
37	*pho-14*	O17373	Predicted phosphatase	Acid phosphatase (ACP2/3/T)	3.19E-03
38	*dod-19*	O61874	Involved in innate immune response		3.55E-03
39	*vit-6*	P18948	Vitellogenin-6, predicted lipid transporter and negative regulation of ROS		3.86E-03
40	*vit-2*	P05690	Vitellogenin-2, predicted lipid transporter		4.03E-03
41	*ttr-51*	O62289	Transthyretin-Related family domain		4.68E-03

42	*vit-1*	P55155	Vitellogenin-1, predicted lipid transporter		4.80E-03
43	*CELE_T20D4.7*	P91468	Involved in unfolded protein response	Nucleoredoxin like (NXNL2)	5.27E-03
44	*asp-5*	O01532	Predicted aspartic-type endopeptidase	Progastricsin (PGC), cathepsin E (CTSE), pepsinogen (PGA3/4/5	5.41E-03
45	*C25E10.8*	Q18157	Predicted serine-type endopeptidase inhibitor		6.10E-03
46	*vit-5*	P06125	Vitellogenin-5, predicted lipid transporter		8.76E-03
47	*vit-4*	P18947	Vitellogenin-4, predicted lipid transporter		9.12E-03
48	*vit-3*	Q9N4J2	Vitellogenin-3, predicted lipid transporter		9.29E-03
49	*CELE_Y41C4A.32*	A0A1D3PDA8	Predicted to be part of COPI vesicle coat, involved in Golgi vesicle transport and intracellular protein transport	COPI coat complex subunit beta 2 (COPB2)	9.37E-03
50	*hum-8*	H2L0I7	Predicted actin filament binding	Myosin VI (MYO6)	1.02E-02

Similarly, to day 4, many sHSPs were upregulated such as *hsp-16.48, hsp-16.41, hsp-16.2* and *hsp-16.1*. Interestingly, human homologs of *hsp-16.2* and *tag-225* were annotated to be involved in Alzheimer´s disease in WormBase. Additionally, predicted proteases as aspartic-type endopeptidases (i.e. *asp-5* and *hrg*-7) and a cathepsin A (*ctsa-1.2*) were also upregulated.

The list of upregulated DEPs and DEGs only minimally overlapped (Fig. 3.23). Six hits (*C04F12.1, tep-1, lec-5, ttr-24, hrg-7, ttr-6*) were upregulated both in the transcriptomic and in the proteomic analysis.

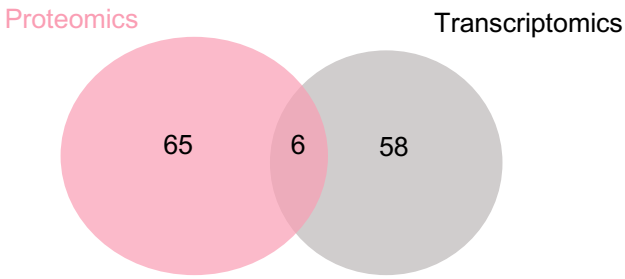

Figure 3. 23: Venn diagram of the upregulated DEPs and DEGs in mAβ day 8

The number of upregulated DEPs from the proteomic analysis are reported in the pink circle while upregulated DEGs from transcriptomic analysis in the grey circle. Common hits are shared between the two circles.

The 47 downregulated DEPs found for mAβ on day 8 were subjected to GO to determine the overrepresented biological processes (Table 3.15). Biological processes related to muscle contraction and actin organization were enriched.

Table 3. 15: GO analysis for downregulated DEPs in mAβ day 8

List of GO terms for biological process and their ID with an FDR < 0.05.

Term ID and description	Genes	Gene count	Background genes	FDR
GO:0006936_Muscle contraction	*tnt-3|tnt-2|pat-10|lev-11*	4	30	0.0058
GO:0030036_Actin cytoskeleton organization	*tnt-3|tnt-2|pat-10|alp-1|lev-11|ZK1321.4*	6	172	0.0058
GO:0048646_Anatomical structure formation involved in morphogenesis	*egg-1|tnt-3|tnt-2|pat-10|cbd-1*	5	106	0.0058
GO:0061061_Muscle structure development	*tnt-3|tnt-2|pat-10|alp-1|ZK1321.4*	5	95	0.0058

The 47 downregulated DEPs were annotated (Table 3.16).

Table 3. 16: 47 downregulated DEPs in mAβ day 8

List of the 47downregulated DEPs in mAβ day 8 ranked according to their FDR value. The gene name and the Uniprot ID are given for each DEP. In addition, each DEP was annotated with a short description and known human homologs.

	Gene	**Protein Uniprot ID**	**Description**	**Human homologs**	**FDR**
1	*CELE_F25E2.2*	G4SF79	Uncharacterized protein		1.91E-09
2	*gln-6*	O02225	Predicted glutamine synthetase	Glutamate-ammonia ligase (GLUL)	5.69E-08
3	*clec-87*	Q9XVS3	C-type lectin, carbohydrate binding	C-type lectin (CLEC2L), killer cell lectin like receptor (KLRB1/G1/F1/F2)	4.11E-06
4	*lev-11*	K8FDX2	Tropomyosin	Tropomyosin (TPM1/2/3/4)	9.96E-06
5	*rml-3*	Q17993	Predicted racemase and epimerase activity		1.10E-05
6	*icl-1*	Q10663	Predicted isocitrate lyase/malate synthase, mitochondrion		1.47E-05
7	*nasp-2*	O17687	Predicted histone binding	Nuclear autoantigenic sperm protein (NASP)	5.23E-05
8	*tnt-2*	Q7Z072	Predicted tropomyosin	Troponin T (TNNT1/2/3)	5.64E-05
9	*noah-1*	H2KZ73	Involved in molting cycle, locomotion and normal body morphology		1.46E-04
10	*fmo-2*	G5EBJ9	Flavin-containing monoxygenase, defense response to bacterium	Flavin containing dimethylaniline monoxygenase (FMO1/2/3/4/5)	1.81E-04
11	*rnr-2*	P42170	Ribonucleotide reductase	Ribonucleotide reductase regulatory subunit M2 (RRM2)	2.50E-04

12	*CELE_T23E7.2*	A0A5E4LWN1	Uncharacterized protein		4.26E-04
13	*noah-2*	Q9XUE5	Involved in molting cycle, locomotion and overall health		4.73E-04
14	*egg-1*	Q09967	LDL-receptor repeat-containing protein, fertilization	LDL receptor related protein (LRP3/10/12)	7.75E-04
15	*grd-6*	A0A3P6MY87	Ground-like domain-containing protein		1.47E-03
16	*imp-1*	Q564X0	Intramembrane aspartic protease, primarly head neurons	Signal peptide peptidase like 2 (SPPL2A/B/C)	1.68E-03
17	*asns-2*	Q21463	Predicted asparagine synthase	Asparagine synthetase (ASNS)	1.86E-03
18	*col-79*	Q09233	Putative cuticle collagen	Surfactant protein D (SFTPD)	2.08E-03
19	*pqn-22*	V6CKH6	Predicted glutamine/asparagine rich protein		3.06E-03
20	*C01G6.3*	Q17572	Uncharacterized protein		3.57E-03
21	*CELE_ZK1321.4*	G5EFP2	Predicted actin binding		4.01E-03
22	*ddo-2*	Q19564	D-aspartate oxidase 2	D-amino acid oxidase (DAO)	5.16E-03
23	*tag-18*	Q22508	Uncharacterized protein		5.48E-03
24	*col-90*	P34340	Putative cuticle collagen		6.77E-03
25	*tnt-3*	A0A4V6M4Y3	Predicted tropomyosin	Troponin T (TNNT1/2/3)	7.59E-03
26	*cht-1*	Q11174	Predicted endochitinase	Chitinase (CHIT1, CHIA, CHI3L2, CHI3L1, OVGP1)	8.76E-03
27	*CELE_F42G10.1*	Q09393	Predicted metalloendopeptidase		8.80E-03
28	*CELE_R13H4.2*	A5Z2W3	Uncharacterized protein		9.66E-03
29	*clik-1*	Q23050	Predicted actin filament binding		9.68E-03

30	*col-149*	Q17417	Putative cuticle collagen	Surfactant protein D (SFTPD)	9.68E-03
31	*alp-1*	G5EFL5	Predicted actin binding activity	LIM domain binding (LDB3), PDZ and LIM domain (PDLIM1/5/7)	1.02E-02
32	*pat-10*	G5EF37	Troponin C	Troponin (TNNC1/2), calmodulin like (CALML6), EF-hand calcium binding domain (EFCAB2)	1.08E-02
33	*EEED8.3*	Q09294	Uncharacterized protein		1.15E-02
34	*cbd-1*	O45599	Predicted chitin binding, involved in eggshell formation		1.23E-02
35	*CELE_F18A1.7*	Q19536	Uncharacterized protein		1.31E-02
36	*nlp-24*	Q20011	Predicted to be involved in neuropeptide signaling pathway		1.69E-02
37	*ctnb-1*	P91401	Catenin Beta like 1, predicted to be part of spliceosomal complex	Catenin beta like 1 (CTNNBL1)	2.04E-02
38	*hach-1*	Q19278	Predicted 3-hydroxyisobutyryl-CoA hydrolase involved in valine catabolic process, mitochondrion	3-hydroxyisobutyryl-CoA hydrolase (HIBCH)	2.04E-02
39	*mlc-3*	P53014	Myosin	Myosin heavy chain (MYH1/2/3/4)	2.34E-02
40	*grd-3*	Q9TYW7	Predicted to be involved in defense response		2.77E-02
41	*col-150*	Q17418	Putative cuticle collagen	Surfactant protein D (SFTPD)	3.32E-02
42	*sodh-1*	Q17334	Predicted to enable alcohol dehydrogenase (NAD+) activity involved in defense response		3.55E-02

43	*CELE_W05H9.1*	Q23179	Uncharacterized protein		3.98E-02
44	*CELE_ZK180.6*	Q23447	Uncharacterized protein		4.15E-02
45	*col-63*	Q94399	Putative cuticle collagen	Surfactant protein D (SFTPD)	4.50E-02
46	*col-118*	A5JYR8	Putative cuticle collagen	Surfactant protein D (SFTPD)	4.89E-02
47	*let-805*	Q9UB28	Myotactin, association between hypodermis and muscle	Tenascin (TNXB), fibronectin (FND3A/B)	4.94E-02

As for day 4, genes involved in muscle structure and contraction were downregulated (i.e. *tnt-3, tnt-2, pat-10, alp-1, ZK1321*). The human homolog of *gln-6* was annotated to be involved in Alzheimer´s disease. Some predicted or known proteases were downregulates such as *imp-1* and *CELE_F42G10.1.*

The list of downregulated DEPs and DEGs only minimally overlapped (Fig. 3.24). Two hits (*icl-1* and *hach-1*) both predicted to be located in the mitochondrion were downregulated in the transcriptomic and in the proteomic analysis.

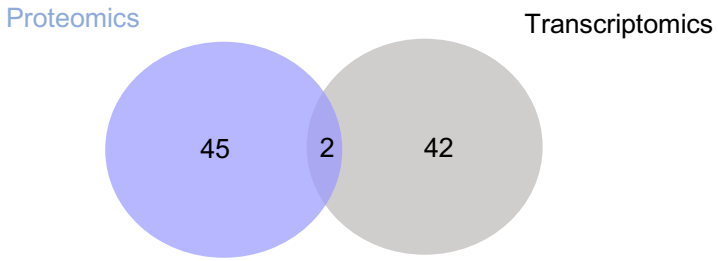

Figure 3. 24: Venn diagram of the downregulated DEPs and DEGs in mAβ day 8

The number of downregulated DEPs from the proteomic analysis are reported in the blue circle while downregulated DEGs from transcriptomic analysis in the grey circle. Common hits are shared between the two circles.

4 Discussion

Proteins can adopt aberrant conformations resulting in protein misfolding and aggregation. These toxic aggregates disturb cellular function, ultimately leading to cell death and impaired organismal health. This phenomenon is particularly relevant in neurodegenerative diseases. Indeed, neurons are particularly vulnerable to protein aggregation because of their post-mitotic nature. Molecular chaperones are essential in maintaining a functional proteome by assisting in protein folding, refolding and aggregate disassembly. Molecular chaperones can counteract protein aggregation and are therefore considered attractive targets to ameliorate neurodegenerative diseases (Paul J. Muchowski and Jennifer L. Wacker, 2005). Thus, the aim of this study was to shed light on the chaperone HSP110 to better understand its role in neuronal proteostasis and in neurodegeneration.

4.1 Generation of a novel *C. elegans* model to study HSP-110 *in vivo*

In this study, the first *C. elegans* model overexpressing *hsp110* pan-neuronally was generated. HSP110 is a poorly characterized molecular chaperone, although it is one of the most abundant cytosolic chaperones present from yeast to human (Easton et al., 2000). The lack of comprehensive knowledge it is also due to limited *in vivo* models. A *hsp-110* knockout in *C. elegans* is lethal and therefore only a depletion by systemic or tissue-specific RNAi could be achieved (Tittelmeier et al., 2020b). To complement the RNAi experiments, a *C. elegans* strain overexpressing *hsp-110* was needed. Yet, a *C. elegans* strain overexpressing *hsp-110* in the neurons or in other tissues was not available. To fill this gap, I generated a novel *C. elegans* strain pan-neuronally overexpressing the nematode *hsp-110* tagged with GFP. The C-terminal GFP tagging has been successfully employed previously for visualizing the endogenous HSP-110 *in vivo* via a Crispr/Cas approach (Tittelmeier et al., 2020b).

Pan-neuronal overexpression of *hsp-110* in *C. elegans* exhibited organismal defects. Other *in vivo* models overexpressing HSP110 have been generated in *Drosophila melanogaster* and in mice, however in these studies the organismal fitness was not compared to wildtype animals (Kuo et al., 2013; Nagy et al., 2016). Interestingly, also

systemic depletion of *hsp-110* in *C. elegans* has also been reported to have negative physiological consequences on growth, lifespan and fertility (Kamath and Ahringer, 2003; Rampelt et al., 2012; Tittelmeier et al., 2020b).

It could be speculated that HSP-110 reduction could lead to organismal defects due to loss of chaperone activity, whereas an overexpression could have inhibitory effects on the HSP-1 cycle. HSP-110 is a crucial chaperone in the proteostasis network and systemic and tissue-specific knockdown revealed an impairment in folding and disaggregation (Rampelt et al., 2012; Tittelmeier et al., 2020b). HSP-110 is a NEF for HSP-1 (HSC70 in human) and hence accelerates the release of ADP from HSP-1, enabling ATP binding to and substrate release from HSP-1 (Kirstein et al., 2017; Nillegoda et al., 2015). However, it is speculated that high concentrations of HSP-110 could induce excessive substrate release from HSP-1, compromising folding and solubilization of misfolded and aggregated proteins. The inhibitory effect of HSP110 on the HSC70 cycle has been demonstrated *in vitro* (Cabrera et al., 2019; Dragovic et al., 2006).

It was shown *in vitro* that the NEF function of HSP110 is optimal at a sub-stoichometric concentration relative to HSC70/HSP-1 (Rampelt et al., 2012). However, in *C. elegans* HSP-1 and HSP-110 are present in equimolar concentrations with 530 nmol/g/total protein of HSP-1 and 560 nmol/g/total protein of HSP110 (Scior et al., 2018). This suggests that in a physiological context HSP-110, besides the NEF activity, may have additional functions which have not been determined yet. For instance, another NEF, BAG3, was found to regulate multiple cellular pathways (e.g. autophagy, apoptosis and cytoskeleton organization) (Rosati et al., 2011)

The chaperone network is composed of a variety of chaperones that can work together in complexes. As mentioned above, HSP-110 acts as a NEF for HSP-1 and, together with a JDP, can ameliorate protein aggregation in *C. elegans* (Kirstein et al., 2017; Scior et al., 2018).

Interestingly, a study using a mouse model overexpressing HSP110 in neuronal cells showed higher HSC70 protein levels and unaffected DNAJB1 levels (Taguchi et al., 2019). Therefore, I quantified the protein levels of the respective *C. elegans* homologs, HSP-1 and DNJ-13, after HSP-110 modulation and showed that both were unaffected in *C. elegans*. There is not an easy explanation for this discrepancy. However, in the mouse model, chaperones were quantified in the brain while in this study HSP-1 and DNJ-13 were measured in the whole body of *C. elegans*. It is worth noting that

mammals express three members of the HSP110 family (APG1, APG2 and HSP105), while *C. elegans* expresses only one cytosolic HSP-110 (Easton et al., 2000). In the mouse model the APG1 member was overexpressed (Taguchi et al., 2019). To my knowledge, none of the previous *hsp-110* RNAi studies in *C. elegans* have measured the protein levels of potential cooperating chaperones. Experiments in HSP105 knockout mice have found unchanged HSC70 protein levels in the brain further supporting that immediate cooperating chaperone levels are unaffected by HSP110 (Nakamura et al., 2008). Additional studies are needed to clarify this discrepancy. Besides its function as part of the trimeric chaperone complex, HSP-110/HSP-1/DNJ-13, it cannot be excluded or is rather likely that HSP-110 has additional functions that may or may not be related to protein folding.

The chaperone network is also interconnected with the protein clearance pathways, i.e. the ubiquitin-proteasome system (UPS) and the lysosome-mediated autophagy. It was demonstrated that systemic *hsp-110* knockdown by RNAi impaired the proteasome capacity and induced autophagy in *C. elegans*. The compromised UPS was associated with a reduction in proteasome subunit levels due to a compromised chaperone machinery (Feleciano et al., 2019). However, in the current study the crosstalk between HSP-110 modulation and UPS has not been investigated and it might be an interesting aspect for future experiments. Nevertheless, I corroborated previous data showing that *hsp-110* depletion enhances autophagy *in vivo* in *C. elegans*. On the other hand, I found that *hsp-110* overexpression compromises autophagy *in vivo*, suggesting that HSP-110 is a negative regulator of autophagy. How HSP-110 regulates autophagy is not known and further studies are needed to elucidate it.

In conclusion, I have generated a novel pan-neuronal *hsp-110* overexpressing strain to complement already existing as well as novel findings from *hsp-110* RNAi experiments. This strain also provides an additional *in vivo* model to advance our knowledge of HSP-110. HSP-110 is an enigmatic chaperone. The inability to obtain a *hsp-110* knockout strain, suggests that HSP-110 plays a vital role in *C. elegans* and that a delicate balance of this protein is required as observed by organismal defects upon its modulation. I could show that HSP-110 exerts broader functions not limited only to the chaperone network but also extend e.g. to the autophagic pathway. While my data begin to shed light, additional studies are needed to elucidate the functional spectrum of HSP-110 *in vivo*.

4.2 HSP-110 is a modulator of $A\beta_{1-42}$ aggregation *in vivo*

This work showed that the chaperone HSP-110 modulates $A\beta_{1-42}$ aggregation in a *C. elegans* model. Neurodegenerative diseases are characterized by the accumulation of aberrant proteins and Aβ deposition is one of the pathological features of Alzheimer´s diseases. In the brain of Alzheimer´s patients, Aβ aggregates enriched in β-rich structures ultimately form amyloid plaques in the extracellular space. However, an increasing number of studies reported the presence of intracellular Aβ accumulation prior to extracellular plaques formation. For this reason, intracellular Aβ aggregation has been suggested to be an early event in the progression of Alzheimer´s disease (LaFerla et al., 2007). The two main isoforms of Aβ peptide are $A\beta_{1-40}$ and $A\beta_{1-42}$. In this work, I investigated the aggregation propensity of $A\beta_{1-42}$ because it is more fibrillogenic than $A\beta_{1-40}$. Observation from human brains indicated that $A\beta_{1-42}$ is the most abundant isoform in amyloid plaques and also the most prominent intraneuronal Aβ species (Gouras et al., 2000; LaFerla et al., 2007). The underlying mechanism of AD remains unclear, it is suggested that Aβ aggregation contributes to cytotoxicity and preventing its accumulation could be an approach for therapeutic intervention(Hampel et al., 2021). Intracellular chaperones play a crucial role in protein homeostasis by inhibiting and reverting abnormal protein associations. Based on their ability to ameliorate aggregation, molecular chaperones have gained increasing interest as therapeutic targets against neurodegenerative diseases (Sharma et al., 2023). HSP110 is an enigmatic chaperone whose functional spectrum has not yet been fully elucidated. However, HSP110 has been implicated in the modulation of amyloidogenic proteins associated with amyotrophic lateral sclerosis, Parkinson´s disease and Huntington's disease in *C. elegans* (Scior et al., 2018; Tittelmeier et al., 2020b; J. Wang et al., 2009). This raised the question whether HSP110 could also modulate $A\beta_{1-42}$ *in vivo*, therefore I used a recently established *C. elegans* model expressing $A\beta_{1-42}$ in the neurons (Gallrein et al., 2021). I manipulated the abundance of the nematode HSP-110 bidirectionally by systemic RNAi-mediated depletion and pan-neuronal overexpression. My data indicates that *hsp-110* depletion suppresses $A\beta_{1-42}$ aggregation *in vivo* and that this phenomenon is particularly prominent in the IL2 neurons, a subset of head neurons that mark the onset of $A\beta_{1-42}$ aggregation in *C.*

elegans. Conversely, *hsp-110* overexpression increased $A\beta_{1-42}$ aggregation and appeared to narrow the conformational variability of the aggregates. At first the enhancement of $A\beta_{1-42}$ aggregation by HSP-110 was surprising as *in vitro* data have revealed a beneficial effect of the chaperone. Indeed, the human APG2 (HSP-110 in *C. elegans*), together with HSC70 (HSP-1 in *C. elegans*) and DNAJB1 (DNJ-13 in *C. elegans*), suppressed $A\beta_{1-42}$ fibrilization *in vitro* (Ayala Mariscal et al., 2022). An additional *in vitro* study revealed that *Drosophila* HSP110 alone can suppress $A\beta_{1-42}$ aggregation through an intrinsically disordered region located in the C-terminal domain. This region is conserved in nematode and human HSP110 homologs (Yakubu and Morano, 2021). Therefore, my initial hypothesis was that nematode HSP-110, either alone or in combination with other chaperones, could suppress $A\beta_{1-42}$ aggregation in *C. elegans*. However, the presented data show the opposite scenario.

How can HSP-110 increase $A\beta_{1-42}$ aggregation? One possible explanation could stem from the participation of HSP-110 in the autophagy-lysosomal pathway. Autophagy ensures the turnover of misfolded and aggregated proteins. Notably, in AD human brains a dysfunctional autophagy was detected by electron microscopy as accumulated autophagic vesicles (Nixon et al., 2005). These data were confirmed also in a neuronal Aβ *Drosophila* model, showing that $A\beta_{1-42}$, but not $A\beta_{1-40}$ induces the accumulation of defective autophagic vesicles (Ling et al., 2009). *C. elegans* strains expressing $A\beta_{1-42}$ either in the muscles or pan-neuronally were also characterized by a compromised autophagy (Feleciano et al., 2019). My work, consistent with recent studies, showed that *hsp-110* depletion enhanced autophagy in *C. elegans*. One might speculate that, autophagy enhancement through *hsp-110* depletion could reduce $A\beta_{1-42}$ aggregation. With a complementary approach, I observed that *hsp-110* overexpression compromised autophagy in *C. elegans* and this scenario could exacerbate $A\beta_{1-42}$ aggregation. Surprisingly, RNAi mediated *hsp-110* downregulation reduces $A\beta_{1-42}$ accumulation but does not enhance *C. elegans* lifespan. However, survival is reduced also in control nematodes, indicating that HSP-110 modulation could have pleotropic effects on *C. elegans*. Additional experiments are necessary to assess the consequence of reduced $A\beta_{1-42}$ deposition on proteotoxicity.

A second explanation could arise from the involvement of HSP-110 in the disaggregation process. HSP-110 is a co-chaperone and it is known to function as a nucleotide exchange factor for HSP-1. HSP-110 accelerates HSP-1 exchange of ADP for ATP, allowing HSP-1 to bind misfolded and aggregated substrates. The HSP-

1/HSP-110 system together with a JDP can suppression aggregation as well as disaggregate toxic protein assemblies (Kirstein et al., 2017; Rampelt et al., 2012; Scior et al., 2018). Whether the chaperone system can disaggregate also $A\beta_{1-42}$ is unknown and needs to be clarified. Notably, it was demonstrated that the chaperone-mediated disaggregation is a double-edged sword in the context of neurodegenerative diseases *in vivo* (Tittelmeier et al., 2020a). It is beneficial because it breaks down protein aggregates, but it could be detrimental if small oligomeric species are released during the process. The soluble oligomers are generated by fibril fragmentation and act as seeds in secondary nucleation, thus exacerbating protein aggregation. Moreover, these seeds can also spread between neurons and to other tissues. Regulating HSP-110 can influence disaggregation activity. A tissue specific *hsp-110* depletion showed reduced α-synuclein aggregation and spreading in a *C. elegans* model for Parkinson´s disease (Tittelmeier et al., 2020b). Similarly, one might speculate that systemic *hsp-110* depletion impairs the chaperone-mediated disaggregation also in a $A\beta_{1-42}$ *C. elegans* model. This would result in fewer Aβ seeds and consequentially reduced $A\beta_{1-42}$ aggregation. Conversely, *hsp-110* overexpression could boost disaggregation resulting in more seeds and exacerbating $A\beta_{1-42}$ aggregation. However, an *hsp-110*-mediated effect of $A\beta_{1-42}$ spreading as judged by a change in the accumulation of $A\beta_{1-42}$ in coelomocytes was not detected. The *C. elegans* model used in this study expressed $A\beta_{1-42}$ pan-neuronally and it was shown that $A\beta_{1-42}$ could spread to other tissues than neurons, as coelomocytes and hypodermis (Gallrein et al., 2021). Deleterious effects of the chaperone mediated disaggregation have been determined also for Tau, another amyloidogenic protein associated to Alzheimer´s disease (Nachman et al., 2020). The authors have shown that the human disaggregase HSC70/APG2/DNAJB1 (HSP-1/HSP-110/DNJ-13 in *C. elegans*) generates small oligomeric Tau species in cell culture.

The chaperone activities of HSP-110 are not well understood and the modulation of $A\beta_{1-42}$ aggregation could also arise from yet unknown functions. For instance, *hsp-110* overexpression increases aggregation and simultaneously reduces $A\beta_{1-42}$ aggregate conformation variability. It was demonstrated *in vitro* that the HSP-110 human homolog (HSP105) as well as the fly homolog (HSP110) can bind $A\beta_{1-42}$ (Yakubu and Morano, 2021). HSP110 alone or together with cooperating chaperones might bind $A\beta_{1-42}$ aggregates and remodel them in a specific conformational state.

My data have shown that HSP-110 can influence $A\beta_{1-42}$ deposition and that *hsp-110* depletion reduces $A\beta_{1-42}$ aggregation *C. elegans*. This study contrast with findings from an Alzheimer´s disease mouse model (Eroglu et al., 2010). Here, a HSP110 knockout mouse model overexpressing mutant APP showed early amyloid plaque formation in the brain. Further analyses are needed to clarify such a discrepancy and overexpressing HSP110 mice could be used as a complementary approach. Nevertheless, due to some differences in the experimental scheme, comparison to data obtained in *C. elegans* might be difficult. For instance, the AD mouse model expresses the full amyloid precursor protein instead of the $A\beta_{1-42}$ peptide, resulting in the generation of both $A\beta_{1-40}$ and $A\beta_{1-42}$ from the amyloidogenic processing as well as peptides from the non-amyloidogenic pathway. Therefore, it is challenging to assess the contribution of HSP110 on the $A\beta_{1-42}$ peptide alone. In addition, the model is a mutant of the human APP, which contains point mutations. These results are based on a knockout of one of the three HSP110 genes while in *C. elegans* there is only one HSP-110 homolog and this was knocked down using a RNAi approach. The same study showed also that loss of HSP110 induced accumulation of Tau. This finding contrast with another study on Tau (Nachman et al., 2020). Further experiments are required for a more comprehensive understanding. It might be more appropriate to validate the data obtained from *C. elegans* using a $A\beta_{1-42}$ *Drosophila* model, which has been already successfully established (Finelli et al., 2004). Analogously to *C. elegans*, *Drosophila* expresses also only one HSP110 gene (Easton et al., 2000).

Interestingly, although chaperones have long been considered targets to ameliorate neurodegenerative diseases, more recent studies have also uncovered deleterious consequences caused by chaperones. As mentioned above, the chaperone-mediated disaggregation enhanced α-synuclein aggregation in a Parkinson's diseases *C. elegans* model (Tittelmeier et al., 2020b). Another recent study revealed that a JDP chaperone, homologs to human DNAJA1, drives $A\beta_{1-42}$ toxicity in yeast and fly models. Besides being a co-chaperone of HSP70, DNAJA1, could also function independently. The authors found that DNAJA1 could bind $A\beta_{1-42}$ and translocate it to the mitochondria inducing cell death. Conversely, DNAJA1 depletion decreased $A\beta_{1-42}$ associated toxicity in flies. *In vitro* experiments also showed that DNAJA1 could delay $A\beta_{1-42}$ fibrilization by stabilizing $A\beta_{1-42}$ oligomeric species (Ring et al., 2022).

To conclude, I have shown that high levels of HSP-110 increases $A\beta_{1-42}$ aggregation. This could result from one or a combination of mechanisms mentioned above. Indeed,

HSP-110 seems to affect various aspects of the cellular proteostasis and additional studies are necessary to gain a mechanistic insight. Further investigations in various model organisms are needed to gain a better understanding of the beneficial versus deleterious consequences of chaperones in neurodegenerative diseases.

4.3 Transcriptomic and proteomic analyses of the $A\beta_{1-42}$ *C. elegans* models

I aimed to obtain a comprehensive data set on global changes in RNA and protein levels in the nAβ (JKM2) and mAβ (JKM8) *C. elegans* models.

Transcriptomic and proteomic studies have been conducted in both human brain tissue and animal models to identify biological pathways associated with AD pathogenesis (Bai et al., 2020; Godini et al., 2019; Wan et al., 2020). Interestingly, an increasing number of studies have found poor correlation between transcriptomic and proteomic data in AD. Indeed, only a modest overlap between protein and transcript changes was found in post-mortem human AD brains (Higginbotham et al., 2020; Seyfried et al., 2017). A multi-omics study of human AD brain tissue further corroborated these findings, showing that about half of the perturbed proteins did not correlate with transcriptomic data. It also showed that perturbed protein levels, rather than transcripts, correlated better with cognitive functions (Johnson et al., 2022). Discrepancies between protein and transcript levels were observed not only in human AD brains, but also in AD mouse models (Bai et al., 2020). This further suggested that proteomics may be more suitable than transcriptomic analysis for understanding AD pathology. The mRNA and protein levels do not always correlate, especially in the brain (Sharma et al., 2015), and protein levels could be affected by transcriptional and post-transcriptional processes, such as translational rate and protein half-life (Liu et al., 2016). For example, altered post-translational modifications (PTMs) and/or protein degradation could explain this inconsistency (Lee et al., 2023; Liu et al., 2016; Zecha et al., 2022).

Based on the condition analysed, up to 27 hits were shared between the neuronal and muscle $A\beta_{1-42}$ *C. elegans* models. Distinct proteomic hits for either the neuronal or muscle model could stem from differences in tissue types. Indeed, various tissues could exhibit differential susceptibility to $A\beta_{1-42}$ and could trigger distinct cell

autonomous and non-autonomous processes. Initially, Aβ *C. elegans* models were developed by expressing Aβ in muscle cells (Link, 1995). Subsequentially, neuronal expression of Aβ was achieved to link aggregation and neuronal function (Fong et al., 2016; Gallrein et al., 2021; Wu et al., 2006). A recent single-cell transcriptomic study in non-disease model of *C. elegans* revealed gene expression bifurcation into two main clusters, neuronal and non-neuronal cells (Roux et al., 2023).

Of the hundreds of molecular chaperones, only DNJ-23 and the sHSPs were increased in nAβ and mAβ, respectively. DNJ-23 is a homolog of DNAJC9, although poorly characterized, one study showed that it functions as a histone chaperone (Hammond et al., 2021). This would correlate with higher histone levels seen in the nAβ strain. On the other hand, the increase of sHSPs (such as HSP-16.1, HSP-16.2, HSP-16.48 and HSP-16.41) were detected only for the mAβ strain. Previous muscle Aβ *C. elegans* models have shown an upregulation in *hsp-16.1*, *hsp-16.2* and *hsp-16.48* transcripts (Fonte et al., 2002; Hassan et al., 2015). The same study has shown that overexpression of *hsp-16.2* could suppress Aβ toxicity in *C. elegans* and have suggested that it occurs by interfering with Aβ oligomerization (Fonte et al., 2008). Interestingly, enhanced levels of sHSP proteins, detected in the current work, was specific for the mAβ strain. One might speculate that it is a protective mechanism exerted by muscle cells against Aβ aggregation in *C. elegans*. Conversely, sHSPs were not increase in the nAβ, which would correlate with greater aggregation and proteotoxicity. Indeed, nAβ exhibits stronger Aβ aggregation as measured by FLIM and reduced median lifespan compared to the mAβ strain (Gallrein et al., 2021).

Although there is no exact homolog, human HSPB proteins (such as HSPB1, HSPB6 and HSPB8) share homology with the *C. elegans* sHSPs (such as HSP-25, HSP-12, HSP-16, etc). HSPB1 was found to be one of the most consistently increased proteins among several proteomic studies in human AD brain samples (Askenazi et al., 2023). Other HSPB, such as HSPB6 and HSPB8, were also increased in the brain of AD individuals (NeuroPro database, Askenazi et al., 2023).

This study did not find alterations in the members of the chaperone complex HSP-1, DNJ-13 and HSP-110*,* respectively homologs of HSC70, DNAJB1 and the HSP110 family (HSP105, APG1, APG2) in human. Proteomic studies in human AD brain showed that these chaperones were mostly unchanged in the hippocampus and decreased in the entorhinal cortex (NeuroPro database, Askenazi et al., 2023).

Why are only sHSPs increased? One possible explanation could lie in the ATP-independent function of the sHSPs (Shim et al., 2003). Foldase chaperones, such as HSP-1 and DAF-21 (homologs of human HSC70 and HSP90) are instead ATP-dependent. It was observed that Aβ-expressing *C. elegans* have reduced ATP levels (Fong et al., 2016). Therefore, ATP-independent compensatory mechanisms may be favoured as first line of defence. HSPs have demonstrated beneficial effects in folding/refolding and holding activities to suppress the formation of toxic aggregates in neurodegenerative diseases. However, it is important to consider that for other chaperone-mediated activities, such as disaggregation, the balance between beneficial and detrimental effects in neurodegenerative diseases remains a topic of debate (Tittelmeier et al., 2020a).

A study investigating extracellular proteostasis in *C. elegans*, provided a list of 57 candidate extracellular regulators of protein aggregation (Gallotta et al., 2020). Two of the 57 candidates, C36C5.5 and ULE-1, showed altered protein levels in this study. Protein levels of C36C5.5 were increased in nAβ and decreased in mAβ, while enhanced levels of ULE-1 were seen both in nAβ and mAβ. Although, no direct human homologs for C36C5.5 and ULE-1 have been identified yet, these data suggested an involvement of the extracellular proteostasis network in the aggregation of $A\beta_{1-42}$ in *C. elegans*.

The level of the SQST-1 protein was enhanced in mAβ. The human homolog of SQST-1, p62, was also increased in the brain of AD individuals (NeuroPro database, Askenazi et al., 2023). Increased levels of this protein were suggested to correlate with defective autophagy (Pankiv et al., 2007). The SKR-9 and SKR-14 are ubiquitin-ligase component and belong to the UPS (Yamanaka et al., 2002). Both SKR-9 and SKR-14 proteins were increased in nAβ, while only SKR-14 was enhanced in mAβ. SKP1 is the human homolog of the SKR proteins in *C. elegans*, and it was also increased in the brain of AD individuals (NeuroPro database, Askenazi et al., 2023). These data suggest that UPS and autophagy are affected by $A\beta_{1-42}$. Altered clearing mechanisms have been previously identified in other Aβ *C. elegans* models, AD mouse models and in human AD brain (Feleciano et al., 2019; Naia et al., 2023; Nixon et al., 2005; Ribeiro et al., 2023). In conclusion, these data show that $A\beta_{1-42}$ expression is associated with global proteomic changes and in particular of proteins involved in several nodes of the proteostasis network.

5 Material

5.1 Chemicals and solutions

Product	Company
Acetic acid	VWR, Radnor, USA
β-mercaptoethanol	Sigma Aldrich, St. Louis, USA
2-Propanol	VWR, Radnor, USA
2-Mercaptoethanol	Sigma Aldrich, St. Louis, USA
Agar Agar	Carl Roth, Karlsruhe, Germany
Agarose	Biozym, Oldendorf, Germany
Agarose universal	Bio&SELL, Nürnberg, Germany
Ammonium peroxodisulfate (APS)	SERVA Feinbiochemica, Heidelberg, Germany
Ampicillin	Sigma Aldrich, St. Louis, USA
Bacto Peptone	Carl Roth, Karlsruhe, Germany
Boric acid	Carl Roth, Karlsruhe, Germany
Bovine serum albumin (BSA)	Sigma Aldrich, St. Louis, USA
Bromphenol blue	Merck, Darmstadt, Germany
Calcium chloride	Sigma Aldrich, St. Louis, USA
Chloroform	Sigma Aldrich, St. Louis, USA
Cholesterol	Sigma Aldrich, St. Louis, USA
cOmplete™ protease inhibitor cocktail	Roche, Mannheim, Germany
Coomassie Brilliant Blue G-250	SERVA Feinbiochemica, Heidelberg, Germany
Dithiothreitol	Carl Roth, Karlsruhe, Germany
DMSO	Carl Roth, Karlsruhe, Germany
dNTPs	Thermo Fisher Scientific, Waltham, USA
Erythrosin B	Sigma Aldrich, St. Louis, USA
Ethanol	Chemsolute

Ethidium bromide	Carl Roth, Karlsruhe, Germany
Ethylenediaminetetraacetic acid	Carl Roth, Karlsruhe, Germany
Glycerol	Carl Roth, Karlsruhe, Germany
Glycine	Sigma Aldrich, St. Louis, USA
Glycogen	Thermo Fisher Scientific, Waltham, USA
Hydrochloric acid (37 %)	VWR, Radnor, USA
IPTG (Isopropyl-β-d-thiogalactopyranoside)	Thermo Fisher Scientific, Waltham, USA
LB agar	SERVA Feinbiochemica, Heidelberg, Germany
LB media	Carl Roth, Karlsruhe, Germany
Magnesium Sulfate	Carl Roth, Karlsruhe, Germany
Methanol	VWR, Radnor, USA
Milk powder	Carl Roth, Karlsruhe, Germany
Mono- & dipotassium phosphate	Merck, Darmstadt, Germany
Mono- & disodium phosphate	Carl Roth, Karlsruhe, Germany
Nuclease-Free Wate	Sigma Aldrich, St. Louis, USA
Potassium hydroxide	Merck, Darmstadt, Germany
ROTIPHORESE gel 30 (37.5:1)	Carl Roth, Karlsruhe, Germany
ROTIQuant 5X	Carl Roth, Karlsruhe, Germany
SOC outgrowth medium	New England Biolabs, Ipswich, USA
Sodium acetate	Riedel-de Haen AG
Sodium azide	Carl Roth, Karlsruhe, Germany
Sodium chloride	Carl Roth, Karlsruhe, Germany
Sodium dodecyl sulfate	Carl Roth, Karlsruhe, Germany
Sodium hydroxide	Carl Roth, Karlsruhe, Germany
Tetramethylethylenediamine (TEMED)	Merck, Darmstadt, Germany
Tris(hydroxymethyl)aminomethane	Carl Roth, Karlsruhe, Germany
Triton X-100	Sigma Aldrich, St. Louis, USA
TRIzol	Thermo Fisher Scientific, Waltham, USA
Tryptone	AppliChem, Darmstadt, Germany

Tween 20	SERVA Feinbiochemica, Heidelberg, Germany
Yeast extract	Carl Roth, Karlsruhe, Germany

5.2 Buffers and media

Name	Composition
10x TBS Used for: Western blot	200 mM Tris, 1,5 M NaCl
10x TBS-T Used for: Western blot	200 mM Tris, 1,5 M NaCl, 1 % Tween 20 (v/v)
4 x Laemmli Loading Buffer Used for: SDS-PAGE, nematode lysis by boiling	100 mM Tris-HCl (pH 6.8), 4 % (w/v) SDS, 30 % (v/v) Glycerol, 0.2 % (w/v) Bromophenol blue, 100 mM DTT
5X TBE Used for: Agarose gel electrophoresis	445 mM Tris, 445 mM Boric Acid, 10 mM EDTA
Coomassie staining solution Used for: SDS-PAGE	2.5 % (v/v) Coomassie brilliant blue G-250, 40 % (v/v) Methanol, 10 % (v/v) Acetic acid
Destaining solution Used for: SDS-PAGE	40 % (v/v) Ethanol, 10 % (v/v) Acetic acid

LB agar Used for: bacterial growth	35 g/l LB Agar + 100 mg/l Ampicillin (optional) after autoclaving
LB medium Used for: bacterial growth	25 g/l LB medium + 100 mg/l Ampicillin (optional) after autoclaving
Lysis buffer Used for: nematode lysis	20 mM Tris HCl (pH 7.5), 10 mM β-Mercaptoethanol, 1% (v/v) Triton X-100, + 1X Protease inhibitor cocktail
M9 Buffer Used for: nematode washing	6 g/l Na_2HPO_4,3 g/l KH_2PO_4, 5 g/l NaCl, Autoclave, then add: 1 mL 1 M $MgSO_4$
NGM-Agar / RNAi-Agar Used for: nematode maintenance	50 mM NaCl, 2,5 g/l Bacto Peptone,17 g/l Agar Agar. Autoclave, then add: 5 µg/ml Cholesterol; 1 mM $CaCl_2$; 1 mM $MgSO_4$; 25 mM KH_2PO_4 pH 6 + 100 µg/ml Ampicillin and 1 mM IPTG for RNAi plates
Running buffer (1x) for SDS-PAGE Used for: SDS-PAGE	25 mM Tris-HCl (pH 8.8), 192 mM Glycine, 0.1 % (w/v) SDS
Separation gel buffer for SDS-PAGE Used for: SDS-PAGE	1.5 M Tris-HCl (pH 8.8), 0.04% (w/v) SDS

Stacking gel buffer for SDS-PAGE Used for: SDS-PAGE	0.5 M Tris-HCl (pH 6.8), 0.04% (w/v) SDS
1X Transfer buffer (semi-dry) Used for: Western blot	1X Turbo Transfer Buffer, 20% (v/v) Ethanol
1X Transfer buffer (wet blotting) Used for: Western blot	25 mM Tris, 192 mM Glycine, 20% (v/v) Methanol

5.3 Kits

Product	**Name**	**Company**
Plasmid isolation	NuceloSpin Plasmid Mini	Macherey-Nagel, Düren, Germany
DNase	RNase-Free DNase Set	Qiagen, Hilden, Germany
ECL Detection Kit	Pierce ECL Western Blot Substrate	Thermo Fisher Scientific, Waltham, USA
Gel extraction	GeneJET Gel extraction kit	Thermo Fisher Scientific, Waltham, USA
Nematode genotyping	Phire Tissue Direct PCR Master Mix	Thermo Fisher Scientific, Waltham, USA
PRC purification	QIAquick PRC purification	Qiagen, Hilden, Germany

Precellys lysis kit	Soft tissue homogenization CK014	Bertin instruments, Montigny-le-Bretonneux, France
RNA extraction	RNeasy Mini Kit	Qiagen, Hilden, Germany
WB	Trans-Blot® Turbo™ Mini PVDF/Nitrocellulose Transfer Packs	BioRad, Hercules, USA

5.4 Enzymes

5.4.1 Restriction enzymes

Enzyme	Company
Pst I (+Buffer G)	Thermo Fisher Scientific, Waltham, USA
BamH I fast digest (+Buffer G)	Thermo Fisher Scientific, Waltham, USA
BamHI-HF (+CutSmart buffer)	New England Biolabs, Ipswich, USA
KpnI-HF (+CutSmart buffer)	New England Biolabs, Ipswich, USA

5.4.2 Other enzymes

Enzyme	Company
Phusion High-Fidelity DNA Polymerase + Phusion HF Buffer	New England Biolabs, Ipswich, USA

T4 Ligase + buffer	Thermo Fisher Scientific, Waltham, USA

5.5 Markers and loading dyes

Product	Company
DNA loading dye (6x)	Thermo Fisher Scientific, Waltham, USA
GeneRuler 1kb DNA Ladder	Thermo Fisher Scientific, Waltham, USA
GeneRuler 50bp DNA Ladder	Thermo Fisher Scientific, Waltham, USA
PageRuler™ Plus Prestained Protein Ladder	Thermo Fisher Scientific, Waltham, USA

5.6 Antibodies

5.6.1 Primary antibodies

Primary antibodies	Origin	Dilution	Company
Anti-HSP-110, full length (polyclonal)	rabbit	1:5000	Kirstein lab (Charles River Laboratories)
Anti-HSP-1 (polyclonal)	rabbit	1:5000	Kirstein lab (Charles River Laboratories)

Anti-DNJ-13 (polyclonal)	rabbit	1:5000	Kirstein lab (Charles River Laboratories)
Anti-GFP B34 (monoclonal)	mouse	1:1000	ENZO Life Sciences, Farmingdale, USA (cat.no: ENZ- ABS141-0200)
Anti LGG-1 (polyclonal)	rabbit	1:1000	Kirstein lab (Pineda)
Anti p62 (polyclonal)	rabbit	1:1000	Kirstein lab (Pineda)
Anti-α -tubulin (monoclonal)	mouse	1:2000	Sigma (cat.no: T5168)

5.6.2 Secondary antibodies

Secondary antibodies	Origin	Dilution	Company
Goat IgG anti-rabbit IgG (H+L)-HRPO	goat	1:10000	DIANOVA (cat.no: 111-035-003)
Goat IgG anti-mouse IgG (H+L)-HRPO	goat	1:10000	DIANOVA (cat.no: 115-035-003)

5.7 Plasmids

Plasmid	Insert	Resistance	Source
pPD95_77	GFP	Amp	Fire Lab
pSUMO::*hsp-110*	nematode HSP-110	Amp	Bukau lab
pPD95_77::*rgef-1p::dbn-1::dendra2*	*rgef-1p::dbn-1::dendra2*	Amp	Kirstein lab
pPD95_77::*rgef-1p::hsp-110::gfp*	*rgef-1p::hsp-110::gfp*	Amp	This work

5.8 Primer sequences

The primer sequences are written in 5´ to 3´direction

5.8.1 Primers for cloning

Primer name	Sequence
Pst I_*rgef-1p*_PrimerFor	ACACTGCAGCATGCAAGACTAATTTTCG
BamH I_*rgef-1p*_PrimerRev	ATAGGATCCGTCGTCGTCGTCGAT
BamH I_*hsp-110* _PrimerFor	ATAGGATCCATGTCGGTTCTTGGATTC
Kpn I_*hsp-110*_PrimerRev	ATAGGTACCGAATCGACATCCATCTCTCC

5.8.2 Primers for genotyping

Primer name	Sequence
*eri-1*_PrimerFor	GATAAAACTTCGGAACATATGGGGC
*eri-1*_PrimerRev	ACTGATGGGTAAGGAATCGAAGACG

5.8.3 Primers for sequencing

Primer name	Sequence
Seq_M13_Rev_universal	CAGGAAACAGCTATGAC
Seq_GFP_Rev(SM)	TACAAACTCAAGAAGGACCATGTG
Seq_*hsp-110*_For1	ATGTCGGTTCTTGGATTCG
Seq_*hsp-110*_For2	GAAGAAATTGACGAGATCG
Seq_*hsp-110*_Rev1	GATCACTGAATTTTCGTCCAATC
Seq_GFP_For_universal	GGTCCTTCTTGAGTTTGTAAC
Seq_GFP_Rev_universal	CCATCTAATTCAACAAGAATTGGGACAAC
Seq_*rgef-1p*_For1	TCATGAGAACCTGAATAGCTC
Seq_*rgef-1p*_For2	GAAGGAGTCATTTCTGCTG
Seq_*rgef-1p*_For3	TTCTTTATGGCTACCGCTTG

5.9 Bacterial strains

Strain	Genotype	Application
E. coli DH5α	*dlacZ Delta M15 Delta (lacZY A-argF) U169 recA1 endA1 hsdR17(rK-mK+) supE44 thi-1 gyrA96 relA1*	plasmid preparation/cloning
E. coli OP50	Uracil auxotroph	*C. elegans* food source
E. coli HT115(DE3) – RNAi	*F-, mcrA, mcrB, IN(rrnD-rrnE)1, rnc14::Tn10(DE3) lysogen: lavUV5 promoter -T6 polymerase*	RNAi

HT115 – RNAi clones	Plasmid	Source
control RNAi	L4440- empty vector	Fire Lab
hsp-110 RNAi	L4440- *hsp-110*	Ahringer Library

5.10 *C. elegans* strains

Strain	Genotype	Source
N2 wildtype	*C. elegans* var Bristol	CGC
GR1373	*eri-1(mg366)*	CGC
n hsp-110 (*I* and *II*)	*Is [rgef-1p::hsp-110::gfp]*	Kirstein lab
nAβ (JKM2)	*Is [rgef-1p*::SigPep-Aβ1-42::*hsp-3*IRES::wrmScarlet-Aβ1-42 + *rps-0p*::hygR CeOpt*]*	Kirstein lab (Gallrein et al., 2021)
nmScarlet	*Is [rgef-1p:: hsp-3*IRES*::mScarlet]*	Kirstein lab (Pigazzini et al., 2021)
nAβ x *n hsp-110 I*	*Is [rgef-1p*::SigPep-Aβ1-42::*hsp-3*IRES::wrmScarlet-Aβ1-42 + *rps-0p*::hygR CeOpt*; rgef-1p::hsp-110::gfp]*	This work
nmScarlet x *n hsp-110 I*	*Is [rgef-1p::hsp-3*IRES*::mScarlet; rgef-1p::hsp-110::gfp]*	This work
ZIM1048	*Is [*mzmIs4 (*unc-31p*::NLS-GCaMP5Kf + *unc-122p*::GFP); *lite-1* (ce314) X*]*	Zimmer Lab
nAβ x ZIM1048	*Is [rgef-1p*::SigPep-Aβ1-42::*hsp-3*IRES::wrmScarlet-Aβ1-42 + *rps-0p*::hygR CeOpt; mzmIs4 (*unc-*	Kirstein lab (Gallrein et al., 2021)

	31p::NLS-GCaMP5Kf + *unc-122p*::GFP); *lite-1* (ce314) X*]*	
nAβ x *n hsp-110 I* x ZIM1048	*Is [rgef-1p*::SigPep-Aβ1-42::*hsp-3*IRES::wrmScarlet-Aβ1-42 + *rps-0p*::hygR CeOpt; *rgef-1p::hsp-110::gfp*; mzmIs4 (*unc-31p*::NLS-GCaMP5Kf + *unc-122p*::GFP); *lite-1* (ce314) X*]*	This work
nAβ x *eri-1*	*Is [rgef-1p*::SigPep-Aβ1-42::*hsp-3*IRES::wrmScarlet-Aβ1-42 + *rps-0p*::hygR CeOpt; *eri-1(mg366)]*	Kirstein lab
nmScarlet x *eri-1*	*Is [rgef-1p:: hsp-3*IRES*::mScarlet; eri-1(mg366)]*	This work
mAβ (JKM7)	*Is [myo-3p*::SigPep-Aβ1-42::*hsp-3*IRES::wrmScarlet-Aβ1-42 + *rps-0p*::hygR CeOpt*]*	Kirstein lab (Gallrein et al., 2021)
mmScarlet	*Is [myo-3p*::wrmScarlet_ext + *rps-0p*::hygR CeOpt*]*	Kirstein lab
nmScarlet (JKM3)	*Is [rgef-1p*::wrmScarlet_ext + *rps-0p*::hygR CeOpt*]*	Kirstein lab (Gallrein et al., 2021)

5.11 Consumables

Consumable	Manufacturer
Pipette tips (1000 µL, 200 µL, 10 µL)	Sarstedt Nümbrecht, Germany
96-well Microplate, transparent	Sarstedt, Nümbrecht, Germany
Conical flasks	Schott, Mainz, Germany
CryoPure Tube 2 ml	Sarstedt, Nümbrecht, Germany
Cuvettes	Eppendorf, Hamburg, Germany
Falcon tubes (15 ml, 50 mL)	Sarstedt, Nümbrecht, Germany
Glass Microscopy Cover Slips	Epredia, Braunschweig, Germany
Glass Microscopy Slides	Epredia, Braunschweig, Germany
Graduated cylinders	Vitlab, Großostheim, Germany
Laboratory bottles with cap	Schott Mainz, Germany
Low Binding Tubes 1.5 ml	Sarstedt, Nümbrecht, Germany
Microtubes (1.5 mL, 2 mL)	Sarstedt, Nümbrecht, Germany
Parafilm	Carl Roth, Karlsruhe, Germany
Pasteur pipettes	Brand, Wertheim, Germany

PCR tubes	Sarstedt, Nümbrecht, Germany
Petri dishes (35 mm, 60 mm, 100 mm)	Thermo Fisher Scientific, Waltham, USA
Platinum wire (0.3 mm)	Carl Roth, Karlsruhe, Germany
PVDF membrane 0.45 µm	Carl Roth, Karlsruhe, Germany
Rotilab Blotting paper 0.35 mm	Carl Roth, Karlsruhe, Germany
Serological pipettes (5 mL, 10 mL, 25mL)	Sarstedt, Nümbrecht, Germany
Sterile tube 14 ml round bottom	Greiner Bio-one, Germany

5.12 Equipment

Device	**Name**	**Company**
Centrifuge	Centrifuge 5415 D	Eppendorf, Hamburg, Germany
	Centrifuge 5810 R	Eppendorf, Hamburg, Germany
	Centrifuge MiniSpin®	Eppendorf, Hamburg, Germany
Confocal Laser Scanning Microscope (LSM)	LSM 880 with Airyscan	Zeiss, Oberkochen, Germany

Container (electrophoresis)	Mini PROTEAN® Tetra Cell	Bio-Rad, Hercules, USA
FLIM	Pulsed laser	PicoQuant, Berlin, Germany
Heating Block	Heating-Thermo Shaker MHR 11	Ditabis, Pforzheim, Germany
	Thermomixer Compact	Eppendorf, Hamburg, Germany
Homogenizer	Precellys 24	Bertin instruments, Montigny-le-Bretonneux, France
Incubator	Labwit Ultimate ZWYC-290A	Labwit Scientific, Australia
Magnetic stirrer	Heidolph Magnetic stirrer MR2002	Heidolph, Germany
pH meter		Mettler Toledo, Ohio, USA
Photometer	NanoPhotometer® N60	IMPLEN, Munich, Germany
	BioPhotometer 6131	Eppendorf, Hamburg, Germany
Pipettes	Transferpette	Brand, Wertheim, Germany
Pipettor	Pipetboy	Integra Bioscience, Bibertal, Germany
Plate reader	Infinite® M Plex	Tecan, Männedorf, Switzerland
Power supply	PowerPac™ Basic	Bio-Rad, Hercules, USA

	Delta Elektronika E0300-0.1 Power supply	Delta Elektronika, The Netherlands
Scale	BP 221 S	Sartorius, Göttingen, Germany
	BL 1500	Sartorius, Göttingen, Germany
Shaker (WB)	GFL Shaker 3016	Lauda, Germany
	WT 16	Biometra, Göttingen, Germany
Stereo Microscope	Nikon SMZ745	Nikon, Tokyo, Japan
Stereo Fluorescence Microscope	Leica M165 FC	Leica, Wetzlar, Germany
Thermocycler	C1000 Touch	Bio-Rad, Hercules, USA
UV irradiator	Fluo-Link (TFL-20M, 312nm)	Biometra, Göttingen, Germany
Vortex	Vortex VF2	Janke & Kunkel Labortechnik
WB detection system	ChemoStar Touch ECL	Intas, Göttingen, Germany
WB system (semi-dry)	Trans-Blot Turbo Transfer System	Bio-Rad, Hercules, USA

5.13 Software and online tools

Software/online tool	Company
Microsoft Word 2019	Microsoft Corporation
BioRender	BioRender
Blastn	NCBI, Bethesda, USA
ChemoStarTS	Intas, Göttingen, Germany
Cytoscape 3.10.2	(Shannon et al., 2003)
Fiji v2.3.0	(Schindelin et al., 2012)
FLIMFit 5.1.1	(Warren et al., 2013)
i-control 2.0	Tecan, Männedorf, Switzerland
Microsoft Excel 2019	Microsoft Corporation
Microsoft PowerPoint 2019	Microsoft Corporation
Oasis 2	(Han et al., 2016)
OrthoList 2	(Kim et al., 2018)
Primer3Manager-Bioinformatics	(Untergasser et al., 2012)
Prism 9.0.0	GraphPad
SerialCloner 2.6.1	Serial Basics
SnapGene Viewer	SnapGene

SymPhoTime 64	PicoQuant, Berlin, Germany
Venny 2.1	Oliveros, J.C. (2007-2015) Venny. An interactive tool for comparing lists with Venn's diagrams. https://bioinfogp.cnb.csic.es/tools/venny/index.html
WormBase- WS290	WormBase Consortium, 2000
Zen 2.3 SP1	Zeiss, Oberkochen, Germany
Zen PicoQuant Application	Zeiss, Oberkochen, Germany

6 Methods

6.1 Bacterial transformation by heat shock

50 µl of chemical competent DH5α *E. coli* were thawed on ice for 10 min before adding 100 ng of plasmid or 2-5 µl ligation reaction. The mixture was incubated on ice for additionally 20-30 min and then heat shocked at 42°C for 45 s using a heating block. The tube was again incubated on ice for 2 min before adding 500 µl of preheated SOC medium at 37°C. Bacteria were incubated at 37°C for 1 hour using a heating block and agitation at 750 rpm. 50 µl of bacteria were plated on a LB agar plate containing 100 µg/ml Ampicillin and grown at 37°C overnight.

6.2 Plasmid extraction

A positive DH5α *E. coli* colony was selected from the LB agar plate and transferred into 10-15 ml LB medium containing 100 µg/ml Ampicillin. The bacteria were incubated at 37°C overnight on a rotating mixer. The following day, the plasmid was extracted from 8-10 ml of bacterial culture using the NucleoSpin plasmid purification kit (Macherey-Nagel) and following manufacturer´s instruction. Plasmid was eluted from the column with 50 µl autoclaved ddH_20. After measuring DNA concentration, the plasmid was stored at -20°C. Plasmid sequence was confirmed by DNA sequencing via LGC Genomics.

6.3 Polymerase chain reaction

Polymerase chain reaction (PCR) was employed to amplify specific DNA sequences. The region of interest (ROI) was defined by the binding of a forward primer at the ROI 5´-end (PrimerFor) and a reverse primer at the ROI 3`-end (PrimerRev). Primers were manually designed and contained restriction sites for cloning. Primer features were checked by Primer3Manager and their specificity by Blastn (NCBI). For molecular cloning, the primer sequence had a maximum length of 30 base pairs with a similar melting temperature between primer pairs. For amplification, the Phusion High Fidelity

DNA polymerase was used. The total volume of the reaction mixture was 50 µl and it was assembled on ice by adding nuclease free water, 1X Phusion HF buffer, 200 µM dNTPs, 5 ng plasmid DNA as template, 0.5 µM forward primer, 0.5 µM reverse primer and 1U-2U Phusion DNA polymerase. No $MgCl_2$ was necessary since the Phusion HF buffer already contained 1.5 mM $MgCl_2$ at the final 1X concentration. A tube containing nuclease free water instead of the template was prepared as negative control. All the PCR reactions for molecular cloning were performed with the same settings. The reaction mixture was initially denatured at 98°C for 1 min, followed by 34 cycles of denaturation (98°C for 30 s), annealing (55°C for 30 s) and extension (72°C for 1 min). A final extension at 72°C for 10 min was added after the last cycle. Successful amplification was checked by agarose gel electrophoresis. A PCR from a nematode sample is described in the nematode genotyping section.

6.4 Molecular cloning

The pan-neuronal expression of the nematode *hsp-110* was achieved by cloning the *rgef-1* promoter in the backbone pPD95_77. The pPD95_77 plasmid is used for *C. elegans* protein expression and already contains a GFP tag. The *rgef-1* promoter was amplified by PCR using the pPD95_77::*rgef-1p*::*dbn-1::dendra2* plasmid as template. The primers Pst I_*rgef-1p*_PrimerFor and BamH I_*rgef-1p*_PrimerRev amplified *rgef-1* with the addition of a Pst I restriction site at the 5` and of BamH I restriction site at the 3´. The amplified *rgef-1* fragment was purified by gel extraction from 1% (w/v) agarose gel. 1 µg of the backbone pPD95_77 and 900 ng of the *rgef-1* promoter were digested at 37°C for 1 h with 2 µl Pst I and 1 µl BamH I fast digest restriction enzymes in 1X Buffer G in 30 µl reaction volume. The enzymes were heat inactivated at 80°C for 5 min. The digested *rgef-1* promoter was purified by DNA precipitation while the digested backbone was isolated by gel extraction from 1 % (w/v) agarose gel. The pPD95_77::*rgef-1p* plasmid was obtained by ligation of 50 ng digested pPD95_77 with 1:3 fragment ratio of digested *rgef-1* promoter. Ligation was performed in 10 µl total volume using 1 µl T4 DNA ligase in 1X T4 DNA ligase buffer at 16°C overnight. The next day, DH5α cells were transformed with 2 µl of ligation mixture. Between 5-10 colonies were then separately grown in LB medium and their respective plasmids extracted. Successful cloning of the selected colonies was assessed by restriction

digestion of 500 ng plasmid with Pst I and BamH I in 0.7% (w/v) agarose gel, followed by plasmid sequencing. The nematode *hsp-110* gene was amplified by PCR using the pSUMO *hsp-110* plasmid as template. The primers BamH I_*hsp-110*_PrimerFor and Kpn I_*hsp-110*_PrimerRev inserted a BamH I restriction site at the 5`and a Kpn I at the 3` of the *hsp-110* fragment. The amplified fragment was purified using a spin column. 1 µg of *hsp-110* gene and 1 µg of pPD95_77::*rgef-1p* plasmid were digested at 37°C for 30 min in 20-30 µl total volume by 0.5 µl BamH I HF and 0.5 µl Kpn I HF in 1X CutSmart Buffer. The digested plasmid was purified by gel extraction from a 1% (w/v) agarose gel while the digested *hsp-110* fragment by DNA precipitation. Ligation was performed with T4 ligase as previously described. DH5α was transformed the next day with 5 µl ligation reaction. Successful cloning was monitored by restriction digest of the pPD95_77*:rgef-1p*::*hsp-110::gfp* plasmid with BamH I and Kpn I in 0.7% (w/v) agarose gel, followed by plasmid sequencing.

6.5 Purification of cloning products

DNA products were purified by precipitation, using a spin column, or by extraction from an agarose gel. Clean PCR products were obtained by using the QIAquick PRC purification kit (Qiagen) following manufacturer´s instruction and eluting in 30 µl autoclaved ddH_20. After enzymatic digestion, small fragments were purified by precipitation with 3 M sodium acetate (10% of the initial volume), pure ethanol (2.5 times the initial volume) and 1 µl glycogen. After 10 min, the sample was centrifuged at 4°C for 30 min at 13.000 rpm and the supernatant was discarded. The pellet was washed with 150 µl 70% ethanol, centrifuged again at 4°C for 10 min and the supernatant was discarded again. The sample was incubated for 2-5 min with an open lid to allow residual ethanol to evaporate. The sample was then resuspended in 12 µl autoclaved ddH_20. After PCR or enzymatic digestion, DNA products were also purified by loading the sample on the agarose gel. DNA was then extracted using GeneJET Gel extraction kit (Thermo Fisher Scientific) following manufacturer's instructions and eluted in 30 µl autoclaved ddH_20.

6.6 Agarose gel electrophoresis

Agarose gel electrophoresis separates nucleic acids according to their molecular weight. It was employed during cloning to check for PCR amplification or to purify the region of interest. After cloning, agarose gel was employed also to evaluate the number and the size of the fragments generated from restriction digestion as a proxy for the correctness of the cloning procedure. According to the size of the expected DNA fragments, a 0.7- 3 % (w/v) agarose gel was prepared. Agarose was dissolved in 1X TBE buffer and boiled in a microwave until completely melted. Before casting the gel, 0.5 µg/ml ethidium bromide was added to the solution. The gel was allowed to solidify for 20 min and then moved to the electrophoresis chamber with 1X TBE. Samples were prepared in 20 µl volume by diluting 1 µl PCR reaction or 100-500 ng DNA in autoclaved ddH_20 and 3 µl of 6X sample loading buffer. The GeneRuler marker (1 kB or 50 bp) was also diluted the same way as the samples. Samples and marker were loaded on the gel and separated for 1-1.5 h at 50 V. DNA was visualized using the ChemoStart Touch Imager (Intas).

6.7 DNA/RNA quantification

Nucleic acid concentration was measured using 1-2 µl DNA/RNA sample with a photometer (Biophotometer 6131, Eppendorf) or a nanophotometer device (NanoPhotometer N60, Implen) in nuclease free water.

6.8 Nematode genotyping

Genotyping was necessary when crossing a *C. elegans* strain without a visible marker, such as the GR1373 *eri-1(mg366)* strain. Specific primers for the *eri-1* gene were used to distinguish between homozygous and heterozygous nematodes.
Since the GR1373 strain contains an insertion of 23 nt in the *eri-1* gene, a PCR of homozygous nematodes produces a DNA fragment of a higher molecular weight (193 nt) than of N2 wildtype animals (170 nt). For genotyping, 20 day 4 old nematodes were harvested in a low binding tube containing 1 ml M9 buffer. Nematodes were washed three times in M9 by centrifuging at 2.000 rpm for 2 min and discarding the supernatant.

After the last wash, about 20 µl of M9 buffer was left to prevent nematodes to dry out. The Phire Tissue Direct PCR Master Mix (Thermo Scientific) was used to perform a PCR directly from the nematode sample according to manufacturer´s instruction. In brief, 10 µl of dilution buffer was added to the sample, followed by 0.5 µl DNA Release additive. The sample was briefly vortexed and then centrifuged. It was then incubated for 5 min at room temperature and subsequently subjected to 98°C for 2 min using a heating block. The sample was then centrifuged at 13.000 rpm for 1 min and the supernatant stored at -20°C if not immediately used. The PCR reaction was prepared with 1 µl of sample in a total volume of 20 µl. PCR was performed following the 3-step cycling protocol: initial denaturation at 98°C for 5 min, denaturation at 98°C for 5 s, annealing at 60°C for 10 s, extension at 72°C for 20 s and final extension at 72°C for 1 min. 40 cycles were performed and then 3-5 µl of PCR product was loaded in a 3 % (w/v) agarose gel.

6.9 RNA extraction from nematodes

Total RNA was extracted from day 4 and day 8 old nematodes. For this, nematodes were separated from their progeny daily between day 4 and day 8 by washing them off the plate with M9. Nematodes were harvested in a 15 ml conical tube or 1.5 ml low binding tube and allowed to settle by gravity for 5 min before discarding the supernatant. L1 and L2 larvae remain in the supernatant and can be easily separated from adult animals. Nematodes were washed 3-5 times and the presence of larvae in the supernatant was monitored using a stereomicroscope. The nematodes were mixed with 100 µl M9 and then transferred to a fresh NGM plate and incubated at 20°C.
200 synchronized nematodes were washed off the plate with M9 and harvested in a low binding tube. Animals were washed three times by centrifuging at 2.000 rpm for 2 min, discarding the supernatant and adding fresh M9. After the last wash, about 20 µl M9 were left to prevent animals to dry out and 250 µl cold Trizol was added. The sample was continuously vortexed for 10 min at 4°C and subsequentially incubated on ice for 10 min. This procedure was repeated three times. 50 µl chloroform was added to the sample, manually shaken and incubated at room temperature for 3 min. The sample was centrifuged at 13.000 rpm for 15 min at 4°C. The upper aqueous phase (approximatively 120-150 µl) was collected without disturbing the interphase and

transferred to a new tube. An equal volume of 70% ethanol was added to the aqueous phase and mixed until homogenous. The total RNA was then purified at room temperature using the Qiagen RNeasy extraction kit (Qiagen) according to manufacturer´s instructions. Briefly, the entire mixture was added to the centre of the RNeasy mini spin column and the sample was centrifuged at 13.000 rpm for 1 min. The flow through was discarded, 350 µl of RW1 buffer was added to the column and centrifuged again. 10 µl of DNase I was mixed with 70 µl RDD buffer and added to the centre of the column (Qiagen RNase-free DNase set, Qiagen). The column was incubated at room temperature for 20 min and then washed with 350 µl of RW1 buffer, with 500 µl of RPE buffer and with 500 µl of 80% ethanol. At every washing step, the column was centrifuged for 15 s at 13.000 rpm. The column was then placed in a new collection tube and centrifuged for additionally 2 min to remove residual ethanol. RNA was eluted in a new tube by adding 30 µl of RNase- free water. RNA concentration was measured, and the samples were stored at -80°C.

6.10 Protein extraction from nematodes

Nematodes were lysed either by boiling in Laemmli loading buffer or by bead homogenization.

Total proteins were extracted by boiling. 100-125 synchronized animals of the desired age were picked and transferred in a low binding tube containing 1 ml M9 buffer. Nematodes were pelleted by centrifuging at 2.000 rpm for 2 min and the supernatant was discarded. Fresh M9 buffer was added, and the procedure was repeated at least three time to wash nematodes until the supernatant was clear. After the last wash, 20 µl M9 were left and 30 µl 4X Laemmli loading buffer was added. The sample was boiled at 99°C for 15 min at 1.000 rpm. The sample was then briefly centrifuged at 13.000 rpm for 1 min to collect the evaporated water and was stored at -20°C. For SDS-PAGE, about 10-20 µl of boiled sample was loaded onto the SDS-PAGE gel.

Nematodes were also homogenised using a Precellys device (Bertin technologies). In this case, at least two 60 mm NGM plates of synchronized animals of the desired age were washed off the plates with 2 ml M9 buffer. Nematodes were washed at least three times in M9 buffer in a low binding tube as previously described. After the last wash, about 20 µl of M9 was left and 1 ml of cold lysis buffer was added on top. Lysis Buffer

(20 mM Tris HCl pH 7.5, 10 mM β-Mercaptoethanol, 1% Triton X-100) was kept at 4°C and just before homogenization, fresh 1X Complete Protease inhibitor cocktail (Roche) was added. The sample was centrifuged again at 2.000 rpm for 1 min, supernatant was discarded leaving about 200 µl. The amount of lysis buffer was scaled up if the number of animals was increased (200 µl of lysis buffer was used for about 4 mm nematodes pelleted in 1.5 ml Eppendorf tube). The nematodes in lysis buffer were transferred to a 2 ml Precellys tube containing ceramic beads (Soft tissue homogenization CK014, Bertin technologies). The samples were homogenized at 6.000 rpm for 30 s at room temperature using the Precellys instrument, incubated on ice for 1 min and the procedure was repeated two more times. Successful homogenization was monitored using a stereomicroscope. The lysate was then transferred to a clean tube and centrifuged at 4°C for 15 min at 15.000 g to separate the soluble from the insoluble fraction. After measuring protein concentration by Bradford assay, the soluble fraction was stored at -20°C. About 10 µg protein lysate was subjected to SDS-PAGE.

6.11 Protein quantification

Protein concentration of the soluble fraction was measured by Bradford assay. For that, a 5x Bradford reagent (Roti-Quant) was diluted in dH_20 and 200 µl per well were transferred into a transparent 96-well plate using a multichannel pipette. A BSA calibration series from 0.2 – 3 mg/ml was prepared using a 10 mg/ml stock in the following concentration: 0.2 mg/ml, 0.6 mg/ml, 1 mg/ml, 1.4 mg/ml, 1.8 mg/ml, 2.2 mg/ml, 2.6 mg/ml and 3 mg/ml. For each well, 2 µl of sample or BSA standard were mixed with 200 µl 1X Bradford reagent. The BSA standard measurements were performed in duplicates, while the samples were measured in triplicates. The blank was measured as 2 µl lysis buffer in 1X Bradford reagent in triplicates as well. The 96-well plate was incubated at 37°C for 15 min. The absorbance at 595 nm was measured using a plate reader (Tecan). The protein concentration was quantified by the regression´s equation of the BSA calibration series.

6.12 SDS-PAGE

SDS-PAGE (Bio-Rad) was performed to separate proteins from a nematode lysate according to their molecular weight. SDS-PAGE mini gels of 1.5 mm were cast with 4% stacking gels and 8-12% separating gels based on the molecular weight of the proteins of interested. For detecting HSP-1, GFP and HSP-110, an 8% separating gel was used, for DNJ-13 and p62/SQST-1, a 10%, while for LGG-1 a 12% separating gel. Glass plates were cleaned with 70% ethanol and placed in the casting frame. The separating gel solution was prepared and poured into the gap between the glass plates. To facilitate polymerization and to obtain an even surface, 0.5 ml isopropanol was added on top of the separating gel. After polymerization (20 min), the isopropanol was removed, and the stacking gel solution was poured on top of the separating gel. According to the number of samples loaded, a 10 or 15-well comb was inserted in the stacking gel. The stacking gel was allowed to polymerize for 20 min before being transferred to the Bio-Rad chamber containing 1X SDS-PAGE Running buffer. Samples were prepared in 24 µl total volume by mixing 10 µg of protein lysate, 6 µl of 4X Laemmli loading buffer and ddH_2O. Samples were boiled for 3-5 min at 95°C before loading them onto the gel. 3 µl of protein marker 10-180 kDa (PageRuler^{TM} Prestained protein ladder, Thermo Fisher) was directly added to a free well. Proteins were separated at constant voltage of 60 V until the samples reached the separating gel, then the voltage was increased to 100-120 V.

6.13 Western Blot

SDS-PAGE was followed by western blot for the identification and/or quantification of proteins of interest (i.e. HSP-1, DNJ-13, HSP-110, GFP, LGG-1, p62/SQST-1). The gel was transferred on top of a PDVF membrane, which was prior to its use activated in 100% methanol for about 1 min until the membrane was translucent. All western blots, except for HSP-110, were performed using a semi dry approach using the Trans-Blot Turbo Transfer System (Bio-Rad). For that, a 5X Turbo transfer buffer from the kit was diluted following manufacturer´s instructions to 1X with ddH_20 and ethanol. The activated membrane and two stacks from the transfer pack were equilibrated in 1X semi dry transfer buffer, while the gel was not equilibrated. The sandwich was

assembled in the cassette in this order: one stack, membrane, gel, one stack. The sandwich was rolled with a rolling pin to remove air bubbles. Blotting was performed using the standard settings 25 V up to 1 A for 30 min, only for LGG-1 blotting time was reduced to 15 min. For high molecular weight proteins (i.e. HSP-110), the transfer was performed with a wet approach. For this, a 1X wet transfer buffer was prepared and stored at 4°C. Sponges, 7 X 10 cm cut blotting papers, activated membrane and gel were equilibrated in 1X wet transfer buffer. The sandwich was assembled in the holder cassette from the transparent side in this order: sponge, three layers of blotting papers, membrane, gel, three layers of blotting papers and sponge. The sandwich was rolled with a rolling pin to remove air bubbles. The cassette was transferred to the tank with cold 1X wet transfer buffer and an ice pack. The gel was blotted for 75 min at 100 V. After blotting, the transfer efficiency was checked by staining the gel with Coomassie for 30 min and destained in destaining solution. The membrane was blocked with 3% (w/v) milk in TBS-T for 1 h shaking at room temperature. All the antibodies were diluted in 3% (w/v) milk in TBS-T according to previous experiments. The membrane was incubated overnight while shaking at 4°C with both the antibody for the protein of interest as well as for α-tubulin as internal loading control. The following day, the membrane was washed three times in TBS-T for 10 min and incubated with the secondary antibody against α-tubulin for 1 h while shaking at room temperature. After washing three times for 15 min in TBS-T and once with TBS, α-tubulin was detected via chemiluminescence using ECL-reagent and the ChemoStar device (Intas). The membrane was then incubated with the secondary antibody against the protein of interest for 1 h at room temperature while shaking and the procedure of washing and detection was repeated.

6.14 Western blot quantification with Fiji

Raw western blot images were uploaded in Fiji and converted to 3-3-2 RGB LUT profile for better visualization of the signals. Area, integrated density, mean grey value and min & max grey value were selected in the “Analyze” menu under “set measurement”. Signals were selected with the rectangle drawing tool and the dimensions were kept the same for all the signals, in addition also 5 background regions were measured. The quantification was performed by clicking “Measure” and data were copied to Excel. The

averaged integrated density of the background was calculated and subtracted from the protein band integrated density value. The value for the protein of interest was normalized to the value of α-tubulin for the same sample. Data were displayed as relative values to a control sample (i.e. N2 wildtype or *eri-1*), in this case, signals were divided by the control value.

6.15 *C. elegans* maintenance

C. elegans was maintained on solid nematode growth media (NGM) seeded with live OP50 *E. coli* (Brenner, 1974). Only for RNAi experiments, animals were fed with a different *E. coli* strain as food source (see RNAi treatment section). Nematodes were maintained on 60 mm plates and kept at 20°C in the dark. Every four days, 4-20 nematodes (depending on the strain) were transferred onto fresh plates using a stereomicroscope. For Aβ strains, the brightest nematodes were selected using a fluorescence stereomicroscope to avoid adaptation of the strains. All experiments were performed at 20°C.

6.16 Synchronization

Nematodes were synchronized by egg-laying or by picking L4 animals.
For egg-laying synchronization, 20-40 gravid nematodes were transferred onto a new 60 mm NGM plate. Adult nematodes were kept laying eggs onto the plate for 5-6 h before being removed. Plates with eggs were incubated at 20°C in the dark and after three days showed a well synchronized population of young adult nematodes (referred to as day 4 of life old nematodes).
Aβ pathology leads to developmental defects and results in a highly unsynchronous population. To avoid this, Aβ nematodes were synchronized by selecting L4 (referred to as day 3 of life) from a mixed population plate prepared five days in advance. The L4 nematodes were incubated at 20°C in the dark until next day, when they reached adulthood (day 4).

6.17 Male generation by heat shock

Male nematodes used for genetic crossing were generated by heat shock. 10 L4 nematodes were transferred onto a 60 mm NGM plate. At least 3-5 separate plates were prepared. The plates were then transferred to an incubator set to 30-31°C for 7 hours without stacking the plates on top of each other. Plates were then returned to 20°C. The progeny of the heat shocked nematodes was screened after about 3 days for males. Identified males were transferred to a new plate together with at least 1 L4 hermaphrodite of the same genotype to increase male numbers in the subsequent generation. Once, a sufficient number of males have been obtained, these “male plates” were maintained by selecting 10 males and 2 L4 hermaphrodite (5:1 ratio) of the same genotype.

6.18 Genetic crossing

Crossing two strains with different genotypes generates a hybrid nematode strain. For this, males were produced from one of the two genotypes. 6-7 adult males were then transferred to a 35 mm plate together with 1 L4 hermaphrodite of the other genotype. Using a 35 mm plate instead of larger plates increases mating efficiency. The nematodes were incubated at 20°C for 3-5 days until the progeny (F1 generation) reached L4 larval stage. If the constructs were fluorescently labelled, the F1 generation shows both the fluorescence proteins (fluorescent markers) at low intensity as they are heterozygous. 5-10 L4 hermaphrodites of the F1 generation were singled onto 35 mm plates and let self-fertilize for 3-5 days at 20°C. The progeny (F2 generation) was then scored for homozygous nematodes, which exhibits both fluorescent markers at high intensity. 20 potential homozygous F2 were singled onto 35 mm plates and their F3 progeny screened by fluorescence. If all F3 showed both fluorescent markers at high intensity, the nematodes were homozygous. If only one of the two strains had a fluorescence marker, the genetic cross was performed slightly differently. The two strains were initially crossed as mentioned above. A L4 hermaphrodite from the F1 generation was then transferred to a 35 mm plate together with 6-7 adult males of the parental strain which had not fluorescence marker. This additional step increases the probability to find homozygous for the genotype with no marker. 10-20 fluorescent L4

hermaphrodites of the F2 generation were singled onto 35 mm plates and allowed to self-fertilize. Their F3 progeny was genotyped by PCR to evaluate whether the genotype without marker was homozygous. Once obtained, the selection for homozygosity of the other genotype was based on fluorescence. The brightest fluorescent nematodes were selected, allowed to self-fertilize and the progeny scored for the fluorescence marker.

6.19 UV integration

The extra-chromosomal array (Ex) can be stably integrated (Is) into the genome of the nematode by UV integration.
For that, 150-180 L4/ young adult nematodes carrying the extrachromosomal array were collected in a low binding tube by washing them off the NGM plate with M9 buffer + 0.05% Triton X-100. Nematodes were washed 5 times to remove residual bacteria by centrifuging at 1000 g for 2 min, removing the supernatant and adding fresh M9 + 0.05% Triton X-100. After the last wash, nematodes were transferred to an unseeded 35 mm NGM plate and allowed to crawl for about 20 min. The nematodes were then irradiated with a UV Crosslinker (Fluo Link Biometra) 50 mJ/ cm^2 at 312 nm. Nematodes were separated into groups of five in 20-30 seeded 60 mm NGM plates. After one week at 20°C, the nematodes on the plates were starved and showed plenty of L1 larvae. The NGM agar was chunked onto a fresh 60 mm NGM plates, and the nematodes were allowed to crawl out from the agar for 20-30 min. From every plate, about 10 transgenic L1 larvae were singled onto freshly seeded 35 mm plates, totaling to approximately 300 plates. Nematodes were incubated at 20°C for one week and their progeny was scored. The integration was successful if at least one plate showed only positive offspring for the transgene (e.g., fluorescence marker).

6.20 Backcrossing

To eliminate background mutations generated by UV integration, the strains were backcrossed at least four times using wildtype nematodes. In brief, 6-8 wildtype males were incubated with 1 L4 integrated hermaphrodite (backcross 1x). After 3-4 days at 20°C, the offspring were scored, and 6-8 heterozygous adult males were transferred

to a fresh 35 mm NGM plate together with 1 L4 hermaphrodite wildtype (backcross 2x). 5-10 transgenic offspring were singled on fresh 35 mm NGM plates and let to self-fertilize to generate homozygous nematodes for the transgene. Once homozygous 2x backcrossed were obtained, the procedure was repeated once more to generated 4x backcrossed.

6.21 RNAi treatment

RNA interference (RNAi) was induced systemically in *C. elegans* by feeding. RNAi plates were prepared as NGM plates with the addition of 100 ug/ml Ampicillin and 1 mM IPTG after cooling down to 55°C. Plates were seeded with the *E. coli* HT115 (DE3) bacteria previously grown in LB medium with 100 µg/ml Ampicillin for 16 h at 37°C and later induced with 1 mM IPTG for 2 h at 37°C. Nematodes were cultured for two generations at 20°C on RNAi plates either seeded with HT115 carrying the L4440 empty vector (also called control RNAi) or the *hsp-110* knockdown vector (*hsp-110* RNAi) from the Ahringer library. The nematodes of the second generation were then experimentally investigated.

6.22 Lifespan assay

A lifespan assay evaluates the organismal fitness of the nematodes. Animals were synchronized and 100-180 L4 larvae were transferred in groups of 10-15 animals onto NGM or RNAi plates. For control strains, larger (60 mm) NGM or RNAi plates were preferred to limit the possibility that nematodes crawl off the plates. For compromised nematode lines such as those expressing the Aβ peptide, 35 mm NGM/RNAi plates were used. Nematodes were transferred to fresh plates every other day to separate them from their progeny until the end of their reproductive phase. Every day, alive and dead nematodes were scored. The survival was checked in this sequence until a reaction was observed: first by touching the agar around the nematode with a platinum wire, then by gently touching the tail /mid body/ head of the nematode. Lastly, the agar close to the nematode was touched with a hot platinum wire. If the nematode did not react, it was considered dead and removed from the plate. Animals that crawled off the

plate, died while transferring or exhibited bagging behavior were censored from the analysis. The survival per day (S_i) was calculated as:

$$S_i = \frac{A_i}{N_i} \quad \text{or } S_i = 1 - (\frac{D_i}{N_i})$$

A = alive nematodes per day

D = dead nematodes per day

N = total nematodes as sum of alive and dead per day

And the cumulative survival as:

$$S_{cumulative} = S_1 * S_2 * S_3 * S_{...}$$

The final survival curve is the sum of three independent repeats per strain. Statistical significance was tested with a log-rank test using the online tool Oasis 2 (Online application for survival analysis 2).

6.23 Progeny assay

A progeny assay evaluates the reproductive fitness of the nematodes. For the experiment, animals were synchronized and 30-40 L4 larvae were singled onto 35 mm NGM/RNAi plates. In order to separate the animals from their progeny, nematodes were transferred every day onto fresh plates until they stopped laying eggs. The viable offspring were counted for every nematode. To simplify counting, plates were divided into four quadrants with a marker and offspring were allowed to develop for 2-3 additional days to grow in size.

6.24 Nematode mounting

Confocal imaging of *C. elegans* was performed on alive anesthetized animals. For that, an already prepared 3% (w/v) agarose solution in water was melted at 95°C using a heating block. 200 µl of melted agarose were pipetted on a glass slide and covered with a second glass slide. After the thin agar pad solidified, the second slide was removed by sliding. 20 µl of 250 mM NaN_3 was pipetted on the agar pads as anesthetic. About 20 nematodes were picked from the NGM/RNAi plates and transferred into the drop using a platinum wire. An eye lash was used to remove excess bacteria and

separate each nematode on the slide. A cover slip was applied on top and the slide was then subjected to imaging.

6.25 Confocal microscopy

Confocal images were obtained using a laser-scanning microscope LSM-880 (Zeiss) and nematodes were mounted on glass slides as described in the previous section. The objectives used were either EC Plan-Neofluar 10x/0.3 M27 or Plan-Apochromat 40x/1,4 Oil DIC M27 and a digital zoom between 0.7 to 1.8 was applied. The laser power was kept at 2 %. GFP was excited at 488 nm using an Argon laser, while mScarlet was excited at 543 nm using the HeNe laser. The digital gain was adjusted according to the fluorescent protein, the magnification and the experimental aim. For GFP, the digital gain was 650 or 550 using a 10X objective, while between 370 and 430 for a 40X objective. For mScarlet tagged Aβ, the digital gain was 800 or 900 at 10X and between 460 and 600 for a 40X objective. For mScarlet tagged Aβ detected in the coelomocytes, the digital gain was 800 with a 40X objective. For mScarlet, the digital gain was 1200 with 10X and between 600 and 750 with 40X objective. Transmitted-light images of the nematodes (T-PMT Transmission) were overlayed with the fluorescence image. Pinhole was set between 1.77 and 15.12 AU. Image sizes were 2048 X 2048, 1024 X 1024 or 512 X 512 with a 16 bit depth. The pixel time was either 2.05 µs or 4.10 µs. For quantitative measurements, the parameters were kept the same.

6.26 Fluorescence lifetime imaging microscopy

Protein aggregation was monitored *in vivo* and *in situ* by fluorescence lifetime imaging microscopy (FLIM). The fluorescence lifetime was measured by time correlated single photon counting (TCSPC) using a confocal laser scanning microscope LSM-880 (Zeiss) with a pulsed laser (PicoQuant). The FLIM components consisted of a PDL 828-S Sepia with a diode laser, a Timeharp260 TCSCPC unit and 2 PMS-Hybrid detection unit. Since Aβ was tagged with mScarlet, the fluorescence protein was excited with a 560 nm pulsed laser at 40 MHz with 70% laser intensity. Emission was recorded in the 575 - 625 nm range. Lifetime was monitored in the head neurons by

mounting nematodes on a glass slide (see section mounting nematodes) and focusing on the head with a Plan-Apochromat 40x/1,4 Oil DIC M27 objective. The frame size was set to 512 X 512 with a resolution of 0.231 µm/pixel and a digital zoom of 1.8. Measurements were performed using SymPhoTime 64 Software until the photon count reached 3000 photons in the brightest pixel with a completely open pinhole. An instrumental response function (IRF) was measured using the same settings using Erythrosine B. FLIM data were analyzed using FlimFit (5.1.1) software with pixel wise fitting. The integrated value was set to 30 and the repetition rate to 40MHz. The monoexponentially decay was selected with a time min 1500 ps and time max 4000 ps. The IRF was also loaded for each measurement.

6.27 Fluorescence intensity quantification with Fiji

Raw confocal images were uploaded in Fiji and opened as Hyperstack view and composite colour mode. After choosing the correct channel to quantify, the region of interested (ROI) was selected with the rectangle drawing tool (whole nematode or the head region). Area, integrated density, mean grey and min & max grey value were selected in the analyse menu under “set measurement”. The quantification was performed by clicking “Measure” and data were copied to Excel. Five background regions were also selected and quantified, in this case the dimensions of the rectangle were only kept constant among background regions. The averaged integrated density of the background was calculated and multiplied to the area of the ROI. The value was subtracted from the integrated density of the ROI. Data were displayed as relative values to a control sample. For that, the averaged value for the control sample was calculated and used to normalize the value from the other samples.

6.28 Transcriptomic and proteomic analyses

Significantly up- and downregulated DEGs and DEPs were selected using an FDR cut-off of < 0.05 and are reported with their gene names in section 3.3 of the results. DEPs were analysed using the open-source software Cytoscape 3.10.2. and the Omics visualizer app for data visualisation and the StringApp for STRING and functional enrichment analysis. *Caenorhabditis elegans* was selected as the species and the other settings were used as defaults. Functional enrichment analysis was performed

by selecting GO Biological Process and Genome background. If more than 20 GO terms were retrieved, redundant terms were removed with a cut-off of 0.5. The 50 most up- and downregulated DEPs were manually annotated with a short description from WormBase. Human homologs were obtained from Ortholist 2 and WormBase. Proteomic and transcriptomic data were overlapped using Venn diagrams (Venny 2.1).

6.29 Statistical analysis

Statistical analysis was performed using GraphPad Prism version 9. Student's t-test was performed with Welch´s correction while One/Two-way ANOVA with Bonferroni post hoc test. Significance for lifespan analysis was tested with a log-rank test using Oasis 2 online tool. P-values were selected as: ns = $p > 0.5$; * = $p \leq 0.05$; ** = $p \leq 0.01$; *** = $p \leq 0.001$; **** = $p \leq 0.0001$.

7 References

2023 Alzheimer's disease facts and figures, 2023. Alzheimer's and Dementia 19, 1598–1695. https://doi.org/10.1002/alz.13016

Albert, M.S., DeKosky, S.T., Dickson, D., Dubois, B., Feldman, H.H., Fox, N.C., Gamst, A., Holtzman, D.M., Jagust, W.J., Petersen, R.C., Snyder, P.J., Carrillo, M.C., Thies, B., Phelps, C.H., 2011. The diagnosis of mild cognitive impairment due to Alzheimer's disease: Recommendations from the National Institute on Aging-Alzheimer's Association workgroups on diagnostic guidelines for Alzheimer's disease. Alzheimer's and Dementia 7, 270–279. https://doi.org/10.1016/j.jalz.2011.03.008

Altun, Z.F., Hall, D.H., 2006. WormAtlas Hermaphrodite Handbook - Introduction. WormAtlas.

Alzheimer, A., 1907. Uber eigenartige Erkrankung der Hirnrinde. All Z Psychiatr 64, 146–148.

Antzutkin, O.N., Leapman, R.D., Balbach, J.J., Tycko, R., 2002. Supramolecular structural constraints on Alzheimer's β-amyloid fibrils from electron microscopy and solid-state nuclear magnetic resonance. Biochemistry 41, 15436–15450. https://doi.org/10.1021/bi0204185

Askenazi, M., Kavanagh, T., Pires, G., Ueberheide, B., Wisniewski, T., Drummond, E., 2023. Compilation of reported protein changes in the brain in Alzheimer's disease. Nat Commun 14. https://doi.org/10.1038/s41467-023-40208-x

Ayala Mariscal, S.M., Kirstein, J., 2021. J-domain proteins interaction with neurodegenerative disease-related proteins. Exp Cell Res 399. https://doi.org/10.1016/j.yexcr.2021.112491

Ayala Mariscal, S.M., Pigazzini, M.L., Richter, Y., Özel, M., Grothaus, I.L., Protze, J., Ziege, K., Kulke, M., ElBediwi, M., Vermaas, J. V., Colombi Ciacchi, L., Köppen, S., Liu, F., Kirstein, J., 2022. Identification of a HTT-specific binding motif in DNAJB1 essential for suppression and disaggregation of HTT. Nat Commun 13. https://doi.org/10.1038/s41467-022-32370-5

Bai, B., Wang, X., Li, Y., Chen, P.C., Yu, K., Dey, K.K., Yarbro, J.M., Han, X., Lutz, B.M., Rao, S., Jiao, Y., Sifford, J.M., Han, J., Wang, M., Tan, H., Shaw, T.I., Cho, J.H., Zhou, S., Wang, H., Niu, M., Mancieri, A., Messler, K.A., Sun, X., Wu, Z., Pagala, V., High, A.A., Bi, W., Zhang, H., Chi, H., Haroutunian, V., Zhang, B., Beach, T.G.,

Yu, G., Peng, J., 2020. Deep Multilayer Brain Proteomics Identifies Molecular Networks in Alzheimer's Disease Progression. Neuron 105, 975-991.e7. https://doi.org/10.1016/j.neuron.2019.12.015

Balch, W.E., Morimoto, R.I., Dillin, A., Kelly, J.W., 2008. Adapting Proteostasis for Disease Intervention. Science (1979) 319, 916–919.

Ballatore, C., Lee, V.M.Y., Trojanowski, J.Q., 2007. Tau-mediated neurodegeneration in Alzheimer's disease and related disorders. Nat Rev Neurosci. https://doi.org/10.1038/nrn2194

Becker, W., 2012. Fluorescence lifetime imaging - techniques and applications. J Microsc 247, 119–136. https://doi.org/10.1111/j.1365-2818.2012.03618.x

Ben-Zvi, A., Miller, E.A., Morimoto, R.I., 2009. Collapse of proteostasis represents an early molecular event in Caenorhabditis elegans aging. Proc Natl Acad Sci U S A . 106, 14914–14919. https://doi.org/doi: 10.1073/pnas.0902882106.

Bergström, P., Agholme, L., Nazir, F.H., Satir, T.M., Toombs, J., Wellington, H., Strandberg, J., Bontell, T.O., Kvartsberg, H., Holmström, M., Boreström, C., Simonsson, S., Kunath, T., Lindahl, A., Blennow, K., Hanse, E., Portelius, E., Wray, S., Zetterberg, H., 2016. Amyloid precursor protein expression and processing are differentially regulated during cortical neuron differentiation. Sci Rep 6. https://doi.org/10.1038/srep29200

Bjørkøy, G., Lamark, T., Brech, A., Outzen, H., Perander, M., Øvervatn, A., Stenmark, H., Johansen, T., 2005. p62/SQSTM1 forms protein aggregates degraded by autophagy and has a protective effect on huntingtin-induced cell death. Journal of Cell Biology 171, 603–614. https://doi.org/10.1083/jcb.200507002

Bracher, A., Verghese, J., 2015. The nucleotide exchange factors of Hsp70 molecular chaperones. Front Mol Biosci. https://doi.org/10.3389/fmolb.2015.00010

Brehme, M., Voisine, C., Rolland, T., Wachi, S., Soper, J.H., Zhu, Y., Orton, K., Villella, A., Garza, D., Vidal, M., Ge, H., Morimoto, R.I., 2014. A chaperome subnetwork safeguards proteostasis in aging and neurodegenerative disease. Cell Rep 9, 1135–1150. https://doi.org/10.1016/j.celrep.2014.09.042

Brenner, S., 1974. The genetics of Caenorhabditis elegans. Genetics 77, 71–94. https://doi.org/10.1093/genetics/77.1.71

Brookmeyer, R., Corrada, M.M., Curriero, F.C., Kawas, C., 2002. Survival Following a Diagnosis of Alzheimer Disease, Arch Neurol.

Brothers, H.M., Gosztyla, M.L., Robinson, S.R., 2018. The physiological roles of amyloid-β peptide hint at new ways to treat Alzheimer's disease. Front Aging Neurosci. https://doi.org/10.3389/fnagi.2018.00118

C. elegans Sequencing Consortium, 1998. Genome sequence of the nematode C. elegans: A platform for investigating biology. Science (1979) 282, 2012–2018.

Cabrera, Y., Bernardo-Seisdedos, G., Dublang, L., Albesa-Jové, D., Orozco, N., Rosa Viguera, A., Millet, O., Muga, A., Moro, F., 2022. Fine-tuning of the Hsc70-based human protein disaggregase machinery by the distinctive C-terminal extension of Apg2. J Mol Biol 167841. https://doi.org/10.1016/j.jmb.2022.167841

Cabrera, Y., Dublang, L., Fernández-Higuero, J.A., Albesa-Jové, D., Lucas, M., Viguera, A.R., Guerin, M.E., Vilar, J.M.G., Muga, A., Moro, F., 2019. Regulation of Human Hsc70 ATPase and Chaperone Activities by Apg2: Role of the Acidic Subdomain. J Mol Biol 431, 444–461. https://doi.org/10.1016/j.jmb.2018.11.026

Caldwell, K.A., Willicott, C.W., Caldwell, G.A., 2020. Modeling neurodegeneration in Caenorhabditis elegans. DMM Disease Models and Mechanisms 13. https://doi.org/10.1242/dmm.046110

Chen, G.F., Xu, T.H., Yan, Y., Zhou, Y.R., Jiang, Y., Melcher, K., Xu, H.E., 2017. Amyloid beta: Structure, biology and structure-based therapeutic development. Acta Pharmacol Sin 38, 1205–1235. https://doi.org/10.1038/APS.2017.28

Ciechanover, Brundin, 2003. The Ubiquitin Proteasome System in Neurodegenerative Diseases: Sometimes the Chicken, Sometimes the Egg. Neuron 40, 427–446.

Cohen, S.I.A., Linse, S., Luheshi, L.M., Hellstrand, E., White, D.A., Rajah, L., Otzen, D.E., Vendruscolo, M., Dobson, C.M., Knowles, T.P.J., 2013. Proliferation of amyloid-β42 aggregates occurs through a secondary nucleation mechanism. Proc Natl Acad Sci U S A 110, 9758–9763. https://doi.org/10.1073/pnas.1218402110

Corsi, A.K., 2006. A Biochemist's Guide to C. elegans. Anal Biochem 359, 1–17.

Dikic, 2017. Proteasomal and Autophagic Degradation Systems. Annu Rev Biochem 20, 193–224. https://doi.org/10.1146/annurev-biochem

Djajadikerta, A., Keshri, S., Pavel, M., Prestil, R., Ryan, L., Rubinsztein, D.C., 2020. Autophagy Induction as a Therapeutic Strategy for Neurodegenerative Diseases. J Mol Biol. https://doi.org/10.1016/j.jmb.2019.12.035

Dragovic, Z., Broadley, S.A., Shomura, Y., Bracher, A., Hartl, F.U., 2006. Molecular chaperones of the Hsp110 family act as nucleotide exchange factors of Hsp70s. EMBO Journal 25, 2519–2528. https://doi.org/10.1038/sj.emboj.7601138

Easton, D.P., Kaneko, Y., Subjeck, J.R., 2000. The Hsp110 and Grp170 stress proteins: newly recognized relatives of the Hsp70s, Cell Stress & Chaperones. Cell Stress Society International.

Eroglu, B., Moskophidis, D., Mivechi, N.F., 2010. Loss of Hsp110 Leads to Age-Dependent Tau Hyperphosphorylation and Early Accumulation of Insoluble Amyloid β. Mol Cell Biol 30, 4626–4643. https://doi.org/10.1128/mcb.01493-09

Feleciano, D.R., Juenemann, K., Iburg, M., Brás, I.C., Holmberg, C.I., Kirstein, J., 2019. Crosstalk between chaperone-mediated protein disaggregation and proteolytic pathways in aging and disease. Front Aging Neurosci 11. https://doi.org/10.3389/fnagi.2019.00009

Fernández-Fernández, M.R., Gragera, M., Ochoa-Ibarrola, L., Quintana-Gallardo, L., Valpuesta, J.M., 2017. Hsp70 – a master regulator in protein degradation. FEBS Lett. https://doi.org/10.1002/1873-3468.12751

Finelli, A., Kelkar, A., Song, H.J., Yang, H., Konsolaki, M., 2004. A model for studying Alzheimer's Aβ42-induced toxicity in Drosophila melanogaster. Molecular and Cellular Neuroscience 26, 365–375. https://doi.org/10.1016/j.mcn.2004.03.001

Fong, S., Teo, E., Ng, L.F., Chen, C.B., Lakshmanan, L.N., Tsoi, S.Y., Moore, P.K., Inoue, T., Halliwell, B., Gruber, J., 2016. Energy crisis precedes global metabolic failure in a novel Caenorhabditis elegans Alzheimer Disease model. Sci Rep 6. https://doi.org/10.1038/srep33781

Fonte, V., Kapulkin, J., Taft, A., Fluet, A., Friedman, D., Link, C.D., 2002. Interaction of intracellular amyloid peptide with chaperone proteins.

Fonte, V., Kipp, D.R., Yerg, J., Merin, D., Forrestal, M., Wagner, E., Roberts, C.M., Link, C.D., 2008. Suppression of in vivo β-amyloid peptide toxicity by overexpression of the HSP-16.2 small chaperone protein. Journal of Biological Chemistry 283, 784–791. https://doi.org/10.1074/jbc.M703339200

Fu, Z., Aucoin, D., Davis, J., Van Nostrand, W.E., Smith, S.O., 2015. Mechanism of Nucleated Conformational Conversion of Aβ42. Biochemistry 54, 4197–4207. https://doi.org/10.1021/acs.biochem.5b00467

Gallotta, I., Sandhu, A., Peters, M., Haslbeck, M., Jung, R., Agilkaya, S., Blersch, J.L., Rödelsperger, C., Röseler, W., Huang, C., Sommer, R.J., David, D.C., 2020. Extracellular proteostasis prevents aggregation during pathogenic attack. Nature 2020 584:7821 584, 410–414. https://doi.org/10.1038/s41586-020-2461-z

Gallrein, C., Iburg, M., Michelberger, T., Koçak, A., Puchkov, D., Liu, F., Ayala Mariscal, S.M., Nayak, T., Kaminski Schierle, G.S., Kirstein, J., 2021. Novel amyloid-beta pathology C. elegans model reveals distinct neurons as seeds of pathogenicity. Prog Neurobiol 198. https://doi.org/10.1016/j.pneurobio.2020.101907

Gallrein, C., Williams, A.B., Meyer, D.H., Messling, J.E., Garcia, A., Schumacher, B., 2023. baz-2 enhances systemic proteostasis in vivo by regulating acetylcholine metabolism. Cell Rep 42. https://doi.org/10.1016/j.celrep.2023.113577

Gao, X., Carroni, M., Nussbaum-Krammer, C., Mogk, A., Nillegoda, N.B., Szlachcic, A., Guilbride, D.L., Saibil, H.R., Mayer, M.P., Bukau, B., 2015. Human Hsp70 Disaggregase Reverses Parkinson's-Linked α-Synuclein Amyloid Fibrils. Mol Cell 59, 781–793. https://doi.org/10.1016/j.molcel.2015.07.012

Glenner, G.G., Wong, C.W., 1984. Alzheimer's disease: initial report of the purification and characterization of a novel cerebrovascular amyloid protein. Biochemical and biophysical research communications 120, 885-890

Godini, R., Pocock, R., Fallahi, H., 2019. Caenorhabditis elegans hub genes that respond to amyloid beta are homologs of genes involved in human Alzheimer's disease. PLoS One 14. https://doi.org/10.1371/journal.pone.0219486

Gong, B., Radulovic, M., Figueiredo-Pereira, M.E., Cardozo, C., 2016. The ubiquitin-proteasome system: Potential therapeutic targets for alzheimer's disease and spinal cord injury. Front Mol Neurosci. https://doi.org/10.3389/fnmol.2016.00004

Goode, A., Butler, K., Long, J., Cavey, J., Scott, D., Shaw, B., Sollenberger, J., Gell, C., Johansen, T., Oldham, N.J., Searle, M.S., Layfield, R., 2016. Defective recognition of LC3B by mutant SQSTM1/p62 implicates impairment of autophagy as a pathogenic mechanism in ALS-FTLD. Autophagy 12, 1094–1104. https://doi.org/10.1080/15548627.2016.1170257

Gotoh, K., Nonoguchi, K., Higashitsuji, H., Kaneko, Y., Sakurai, T., Sumitomo, Y., Itoh, K., Subjeck, J.R., Fujita, J., 2004. Apg-2 has a chaperone-like activity similar to Hsp110 and is overexpressed in hepatocellular carcinomas. FEBS Lett 560, 19–24. https://doi.org/10.1016/S0014-5793(04)00034-1

Gouras, G.K., Tsai, J., Naslund, J., Vincent, B., Edgar, M., Checler, F., Greenfield, J.P., Haroutunian, V., Buxbaum, J.D., Xu, H., Greengard, P., Relkin, N.R., 2000. Intraneuronal Aβ42 accumulation in human brain. American Journal of Pathology 156, 15–20. https://doi.org/10.1016/S0002-9440(10)64700-1

Gremer, L., Schölzel, D., Schenk, C., Reinartz, E., Labahn, J., Ravelli, R.B.G., Tusche, M., Lopez-Iglesias, C., Hoyer, W., Heise, H., Willbold, D., Schröder, G.F., 2017. Fibril structure of amyloid- β(1-42) by cryo-electron microscopy. Science 358, 116–119. https://doi.org/doi: 10.1126/science.aao2825

Haass, C., Selkoe, D.J., 2007. Soluble protein oligomers in neurodegeneration: Lessons from the Alzheimer's amyloid β-peptide. Nat Rev Mol Cell Biol. https://doi.org/10.1038/nrm2101

Hammond, C.M., Bao, H., Hendriks, I.A., Carraro, M., García-Nieto, A., Liu, Y., Reverón-Gómez, N., Spanos, C., Chen, L., Rappsilber, J., Nielsen, M.L., Patel, D.J., Huang, H., Groth, A., 2021. DNAJC9 integrates heat shock molecular chaperones into the histone chaperone network. Mol Cell 81, 2533-2548.e9. https://doi.org/10.1016/j.molcel.2021.03.041

Hampel, H., Hardy, J., Blennow, K., Chen, C., Perry, G., Kim, S.H., Villemagne, V.L., Aisen, P., Vendruscolo, M., Iwatsubo, T., Masters, C.L., Cho, M., Lannfelt, L., Cummings, J.L., Vergallo, A., 2021. The Amyloid-β Pathway in Alzheimer's Disease. Mol Psychiatry. https://doi.org/10.1038/s41380-021-01249-0

Hampel, H., Mesulam, M.M., Cuello, A.C., Khachaturian, A.S., Vergallo, A., Farlow, M.R., Snyder, P.J., Giacobini, E., Khachaturian, Z.S., 2019. Revisiting the Cholinergic Hypothesis in Alzheimer's Disease: Emerging Evidence from Translational and Clinical Research. J Prev Alzheimers Dis 6, 2–15. https://doi.org/10.14283/jpad.2018.43

Han, S.K., Lee, D., Lee, H., Kim, D., Son, H.G., Yang, J.-S., Lee, S.-J. V, Kim, S., 2016. OASIS 2: online application for survival analysis 2 with features for the analysis of maximal lifespan and healthspan in aging research. Oncotarget 7, 56147–56152.

Hardy J., Higgins G., 1992. Alzheimer's Disease: The Amyloid Cascade Hypothesis. Science (1979).

Hartl, F.U., Bracher, A., Hayer-Hartl, M., 2011. Molecular chaperones in protein folding and proteostasis. Nature. https://doi.org/10.1038/nature10317

Hashimoto, T., Serrano-Pozo, A., Hori, Y., Adams, K.W., Takeda, S., Banerji, A.O., Mitani, A., Joyner, D., Thyssen, D.H., Bacskai, B.J., Frosch, M.P., Spires-Jones, T.L., Finn, M.B., Holtzman, D.M., Hyman, B.T., 2012. Apolipoprotein e, especially apolipoprotein E4, increases the oligomerization of amyloid β peptide. Journal of Neuroscience 32, 15181–15192. https://doi.org/10.1523/JNEUROSCI.1542-12.2012

Hassan, W.M., Dostal, V., Huemann, B.N., Yerg, J.E., Link, C.D., 2015. Identifying Aβ-specific pathogenic mechanisms using a nematode model of Alzheimer's disease. Neurobiol Aging 36, 857–866. https://doi.org/10.1016/j.neurobiolaging.2014.10.016

Henricson, A., Sonnhammer, E.L.L., Baillie, D.L., Gomes, A.V., 2004. Functional characterization in Caenorhabditis elegans of transmembrane worm-human orthologs. BMC Genomics 5. https://doi.org/10.1186/1471-2164-5-85

Higginbotham, L., Ping, L., Dammer, E.B., Duong, D.M., Zhou, M., Gearing, M., Hurst, C., Glass, J.D., Factor, S.A., Johnson, E.C.B., Hajjar, I., Lah, J.J., Levey, A.I., Seyfried, N.T., 2020. Integrated proteomics reveals brain-based cerebrospinal fluid biomarkers in asymptomatic and symptomatic Alzheimer's disease, Sci. Adv.

Hipp, M.S., Kasturi, P., Hartl, F.U., 2019. The proteostasis network and its decline in ageing. Nat Rev Mol Cell Biol. https://doi.org/10.1038/s41580-019-0101-y

Huang, Y.R., Liu, R.T., 2020. The toxicity and polymorphism of β-amyloid oligomers. Int J Mol Sci. https://doi.org/10.3390/ijms21124477

Jack, C.R., Bennett, D.A., Blennow, K., Carrillo, M.C., Dunn, B., Haeberlein, S.B., Holtzman, D.M., Jagust, W., Jessen, F., Karlawish, J., Liu, E., Molinuevo, J.L., Montine, T., Phelps, C., Rankin, K.P., Rowe, C.C., Scheltens, P., Siemers, E., Snyder, H.M., Sperling, R., Elliott, C., Masliah, E., Ryan, L., Silverberg, N., 2018. NIA-AA Research Framework: Toward a biological definition of Alzheimer's disease. Alzheimer's and Dementia. https://doi.org/10.1016/j.jalz.2018.02.018

Jack, C.R., Knopman, D.S., Jagust, W.J., Shaw, L.M., Aisen, P.S., Weiner, M.W., Petersen, R.C., Trojanowski, J.Q., 2010. Hypothetical model of dynamic biomarkers of the Alzheimer's pathological cascade. Lancet Neurol. https://doi.org/10.1016/S1474-4422(09)70299-6

Johnson, E.C.B., Carter, E.K., Dammer, E.B., Duong, D.M., Gerasimov, E.S., Liu, Y., Liu, J., Betarbet, R., Ping, L., Yin, L., Serrano, G.E., Beach, T.G., Peng, J., De Jager, P.L., Haroutunian, V., Zhang, B., Gaiteri, C., Bennett, D.A., Gearing, M., Wingo, T.S., Wingo, A.P., Lah, J.J., Levey, A.I., Seyfried, N.T., 2022. Large-scale deep multi-layer analysis of Alzheimer's disease brain reveals strong proteomic disease-related changes not observed at the RNA level. Nat Neurosci 25, 213–225. https://doi.org/10.1038/s41593-021-00999-y

Kamath, R.S., Ahringer, J., 2003. Genome-wide RNAi screening in Caenorhabditis elegans. Methods 30, 313–321. https://doi.org/10.1016/S1046-2023(03)00050-1

Kaminski Schierle, G.S., Bertoncini, C.W., Chan, F.T.S., Van Der Goot, A.T., Schwedler, S., Skepper, J., Schlachter, S., Van Ham, T., Esposito, A., Kumita, J.R., Nollen, E.A.A., Dobson, C.M., Kaminski, C.F., 2011. A FRET sensor for non-invasive imaging of amyloid formation in vivo. ChemPhysChem 12, 673–680. https://doi.org/10.1002/cphc.201000996

Kampinga, H.H., Bergink, S., 2016. Heat shock proteins as potential targets for protective strategies in neurodegeneration. Lancet Neurol 15, 748-759

Kampinga, H.H., Craig, E.A., 2010. The HSP70 chaperone machinery: J proteins as drivers of functional specificity. Nat Rev Mol Cell Biol. https://doi.org/10.1038/nrm2941

Kampinga, H.H., Hageman, J., Vos, M.J., Kubota, H., Tanguay, R.M., Bruford, E.A., Cheetham, M.E., Chen, B., Hightower, L.E., 2009. Guidelines for the nomenclature of the human heat shock proteins. Cell Stress Chaperones. https://doi.org/10.1007/s12192-008-0068-7

Kaneko, Y., Kimura, T., Kishishita, M., Noda, Y., Fujita, J., 1997a. Cloning of apg-2 encoding a novel member of heat shock protein 110 family, J. Biol. Chem.

Kaneko, Y., Nishiyama, H., Nonoguchi, K., Higashitsuji, H., Kishishita, M., Fujita, J., 1997b. A Novel hsp110-related Gene, apg-1, That Is Abundantly Expressed in the Testis Responds to a Low Temperature Heat Shock Rather than the Traditional Elevated Temperatures*, The journal of biological chemistry.

Kennedy Scott, Wang Duo, Ruvkun Gary, 2004. A conserved siRNA-degrading RNase negatively regulates RNA interference in C.elegans. Nature 427, 640–645. https://doi.org/10.1038/nature02320

Kim, Underwood, Greenwald, Shaye, D., 2018. OrthoList 2: A New Comparative Genomic Analysis of Human and Caenorhabditis elegans Genes. https://doi.org/10.1534/genetics.118.301307

Kim, Y., Park, Y., Hwang, J., Kwack, K., 2018. Comparative genomic analysis of the human and nematode Caenorhabditis elegans uncovers potential reproductive genes and disease associations in humans. Physiol Genomics 50, 1002–1014. https://doi.org/10.1152/physiolgenomics.00063.2018.-Reproduction

Kirstein, J., Arnsburg, K., Scior, A., Szlachcic, A., Guilbride, D.L., Morimoto, R.I., Bukau, B., Nillegoda, N.B., 2017. In vivo properties of the disaggregase function of J-proteins and Hsc70 in Caenorhabditis elegans stress and aging. Aging Cell 16, 1414–1424. https://doi.org/10.1111/acel.12686

Kityk, R., Vogel, M., Schlecht, R., Bukau, B., Mayer, M.P., 2015. Pathways of allosteric regulation in Hsp70 chaperones. Nat Commun 6. https://doi.org/10.1038/ncomms9308

Klaips, C.L., Jayaraj, G.G., Hartl, F.U., 2018. Pathways of cellular proteostasis in aging and disease. Journal of Cell Biology. https://doi.org/10.1083/jcb.201709072

Knopman, D.S., Amieva, H., Petersen, R.C., Chételat, G., Holtzman, D.M., Hyman, B.T., Nixon, R.A., Jones, D.T., 2021. Alzheimer disease. Nat Rev Dis Primers 7. https://doi.org/10.1038/s41572-021-00269-y

Kosik, K.S., Joachim, C.L., Selkoe, D.J., 1986. Microtubule-associated protein tau (T) is a major antigenic component of paired helical filaments in Alzheimer disease (cytoskeleton/neurofibrillary tangles/neuronal degeneration), Proc. Nati. Acad. Sci. USA.

Kuo, Y., Ren, S., Lao, U., Edgar, B.A., Wang, T., 2013. Suppression of polyglutamine protein toxicity by co-expression of a heat-shock protein 40 and a heat-shock protein 110. Cell Death Dis 4. https://doi.org/10.1038/cddis.2013.351

Labbadia, J., Morimoto, R.I., 2015. The Biology of Proteostasis in Aging and Disease. Annu Rev Biochem 84, 435–464. https://doi.org/10.1146/annurev-biochem-060614-033955

Labbadia, J., Morimoto, R.I., 2014. Proteostasis and longevity: when does aging really begin? https://doi.org/10.12703/P6-7

LaFerla, F.M., Green, K.N., Oddo, S., 2007. Intracellular amyloid-β in Alzheimer's disease. Nat Rev Neurosci. https://doi.org/10.1038/nrn2168

Lai, C., Chou, C., Ch'ang, L., Liu, C., Lin, W., 2000. Identification of Novel Human Genes Evolutionarily Conserved in Caenorhabditis elegans by Comparative Proteomics. Genome Res 10, 703–713. https://doi.org/doi:10.1101/gr.10.5.703

Laine, R.F., Sinnige, T., Ma, K.Y., Haack, A.J., Poudel, C., Gaida, P., Curry, N., Perni, M., Nollen, E.A.A., Dobson, C.M., Vendruscolo, M., Kaminski Schierle, G.S., Kaminski, C.F., 2019. Fast Fluorescence Lifetime Imaging Reveals the Aggregation Processes of α-Synuclein and Polyglutamine in Aging Caenorhabditis elegans. ACS Chem Biol 14, 1628–1636. https://doi.org/10.1021/acschembio.9b00354

Lambert, M.P., Barlow, A.K., Chromy, B.A., Edwards, C., Freed, R., Liosatos, M., Morgan, T.E., Rozovsky, I., Trommer, B., Viola, K.L., Wals, P., Zhang, C., Finch, C.E., Krafft ¶, G.A., Klein, W.L., 1998. Diffusible, nonfibrillar ligands derived from

A 1-42 are potent central nervous system neurotoxins. Proc. Natl. Acad. Sci. 95, 6448–6453.

Lee, J.M., Hammarén, H.M., Savitski, M.M., Baek, S.H., 2023. Control of protein stability by post-translational modifications. Nat Commun. https://doi.org/10.1038/s41467-023-35795-8

Lee-Yoon, D., Easton, D., Murawski, M., Burd, R., Subjeck11, J.R., 1995. Identification of a Major Subfamily of Large hsp70-like Proteins through the Cloning of the Mammalian 110-kDa Heat Shock Protein*. J Biol Chem 270, 15725–15733.

Ling, D., Song, H.J., Garza, D., Neufeld, T.P., Salvaterra, P.M., 2009. Abeta42-induced neurodegeneration via an age-dependent autophagic-lysosomal injury in Drosophila. PLoS One 4. https://doi.org/10.1371/journal.pone.0004201

Link, C.D., 1995. Expression of human β-amyloid peptide in transgenic Caenorhabditis elegans, Neurobiology.

Linse, S., 2019. Mechanism of amyloid protein aggregation and the role of inhibitors, in: Pure and Applied Chemistry. De Gruyter, pp. 211–229. https://doi.org/10.1515/pac-2018-1017

Liu, P.P., Xie, Y., Meng, X.Y., Kang, J.S., 2019. History and progress of hypotheses and clinical trials for alzheimer's disease. Signal Transduct Target Ther. https://doi.org/10.1038/s41392-019-0063-8

Liu, Y., Beyer, A., Aebersold, R., 2016. On the Dependency of Cellular Protein Levels on mRNA Abundance. Cell. https://doi.org/10.1016/j.cell.2016.03.014

Mack, H.I.D., Heimbucher, T., Murphy, C.T., 2018. The nematode Caenorhabditis elegans as a model for aging research. Drug Discov Today Dis Models. https://doi.org/10.1016/j.ddmod.2018.11.001

Malinverni, D., Zamuner, S., Rebeaud, M.E., Barducci, A., Nillegoda, N.B., Rios, P.D.L., 2023. Data-driven large-scale genomic analysis reveals an intricate phylogenetic and functional landscape in J-domain proteins. Proc Natl Acad Sci U S A 120. https://doi.org/10.1073/pnas.2218217120

Maragos, W.F., Greenamyre, J.T., Penney, J.B., Young, A.B., 1987. Glutamate dysfundion in Alzheimer's disease: an hypothesis. Trends Neurosci 65–68.

Markaki, M., Tavernarakis, N., 2010. Modeling human diseases in Caenorhabditis elegans. Biotechnol J. https://doi.org/10.1002/biot.201000183

Mattoo, R.U.H., Sharma, S.K., Priya, S., Finka, A., Goloubinoff, P., 2013. Hsp110 is a bona fide chaperone using ATP to unfold stable misfolded polypeptides and

reciprocally collaborate with Hsp70 to solubilize protein aggregates. Journal of Biological Chemistry 288, 21399–21411. https://doi.org/10.1074/jbc.M113.479253

McKhann, G.M., Knopman, D.S., Chertkow, H., Hyman, B.T., Jack, C.R., Kawas, C.H., Klunk, W.E., Koroshetz, W.J., Manly, J.J., Mayeux, R., Mohs, R.C., Morris, J.C., Rossor, M.N., Scheltens, P., Carrillo, M.C., Thies, B., Weintraub, S., Phelps, C.H., 2011. The diagnosis of dementia due to Alzheimer's disease: Recommendations from the National Institute on Aging-Alzheimer's Association workgroups on diagnostic guidelines for Alzheimer's disease. Alzheimer's and Dementia 7, 263–269. https://doi.org/10.1016/j.jalz.2011.03.005

Menzies, F.M., Fleming, A., Rubinsztein, D.C., 2015. Compromised autophagy and neurodegenerative diseases. Nat Rev Neurosci. https://doi.org/10.1038/nrn3961

Mukai, H., Kunoa, T., Tanaka, H., Hiratab, D., Miyakawab, T., Tanakaa, C., 1993. Isolation and characterization of SSEl and SSE2, new members of the yeast HSP70 multigene family. Gene 132, 57–66.

Müller, U.C., Deller, T., Korte, M., 2017. Not just amyloid: Physiological functions of the amyloid precursor protein family. Nat Rev Neurosci. https://doi.org/10.1038/nrn.2017.29

Nachman, E., Wentink, A.S., Madiona, K., Bousset, L., Katsinelos, T., Allinson, K., Kampinga, H., McEwan, W.A., Jahn, T.R., Melki, R., Mogk, A., Bukau, B., Nussbaum-Krammer, C., 2020. Disassembly of Tau fibrils by the human Hsp70 disaggregation machinery generates small seeding-competent species. Journal of Biological Chemistry 295, 9676–9690. https://doi.org/10.1074/JBC.RA120.013478

Nagy, M., Fenton, W.A., Li, D., Furtak, K., Horwich, A.L., 2016. Extended survival of misfolded G85R SOD1-linked ALS mice by transgenic expression of chaperone Hsp110. Proc Natl Acad Sci U S A 113, 5424–5428. https://doi.org/10.1073/pnas.1604885113

Naia, L., Shimozawa, M., Bereczki, E., Li, X., Liu, J., Jiang, R., Giraud, R., Leal, N.S., Pinho, C.M., Berger, E., Falk, V.L., Dentoni, G., Ankarcrona, M., Nilsson, P., 2023. Mitochondrial hypermetabolism precedes impaired autophagy and synaptic disorganization in App knock-in Alzheimer mouse models. Mol Psychiatry 28, 3966–3981. https://doi.org/10.1038/s41380-023-02289-4

Nakamura, J., Fujimoto, M., Yasuda, K., Takeda, K., Akira, S., Hatayama, T., Takagi, Y., Nozaki, K., Hosokawa, N., Nagata, K., 2008. Targeted disruption of Hsp110/105

gene protects against ischemic stress. Stroke 39, 2853–2859. https://doi.org/10.1161/STROKEAHA.107.506188

Nasreddine, Z., Garibotto, V., Kyaga, S., Padovani, A., 2023. The Early Diagnosis of Alzheimer's Disease: A Patient-Centred Conversation with the Care Team. Neurol Ther. https://doi.org/10.1007/s40120-022-00428-7

Nikolaidis, N., Nei, M., 2004. Concerted and Nonconcerted Evolution of the Hsp70 Gene Superfamily in Two Sibling Species of Nematodes. Mol Biol Evol 21, 498–505. https://doi.org/10.1093/molbev/msh041

Nillegoda, N.B., Kirstein, J., Szlachcic, A., Berynskyy, M., Stank, A., Stengel, F., Arnsburg, K., Gao, X., Scior, A., Aebersold, R., Guilbride, D.L., Wade, R.C., Morimoto, R.I., Mayer, M.P., Bukau, B., 2015. Crucial HSP70 co-chaperone complex unlocks metazoan protein disaggregation. Nature 524, 247–251. https://doi.org/10.1038/nature14884

Nilsson, P., Loganathan, K., Sekiguchi, M., Matsuba, Y., Hui, K., Tsubuki, S., Tanaka, M., Iwata, N., Saito, T., Saido, T.C., 2013. Aβ Secretion and Plaque Formation Depend on Autophagy. Cell Rep 5, 61–69. https://doi.org/10.1016/j.celrep.2013.08.042

Nixon, R.A., Wegiel, J., Kumar, A., Yu, W.H., Peterhoff, C., Cataldo, A., Cuervo, A.M., 2005. Extensive Involvement of Autophagy in Alzheimer Disease: An Immuno-Electron Microscopy Study, J Neuropathol Exp Neurol.

Nonoguchi, K., Itoh, K., Xue, J.-H., Tokuchi, H., Nishiyama, H., Kaneko, Y., Tatsumi, K., Okuno, H., Tomiwa, K., Fujita, J., 1999. Cloning of human cDNAs for Apg-1 and Apg-2, members of the Hsp110 family, and chromosomal assignment of their genes, Gene.

Oh, H.J., Chen, X., Subjeck, J.R., 1997. hsp110 protects heat-denatured proteins and confers cellular thermoresistance. Journal of Biological Chemistry 272, 31636–31640. https://doi.org/10.1074/jbc.272.50.31636

Pankiv, S., Clausen, T.H., Lamark, T., Brech, A., Bruun, J.A., Outzen, H., Øvervatn, A., Bjørkøy, G., Johansen, T., 2007. p62/SQSTM1 binds directly to Atg8/LC3 to facilitate degradation of ubiquitinated protein aggregates by autophagy*[S]. Journal of Biological Chemistry 282, 24131–24145. https://doi.org/10.1074/jbc.M702824200

Papaevgeniou, N., Chondrogianni, N., 2014. The ubiquitin proteasome system in Caenorhabditis elegans and its regulation. Redox Biol. https://doi.org/10.1016/j.redox.2014.01.007

Parsen, D.A., Kowalt, A.S., Singer, M.A., Lindquist, S., 1994. Protein disaggregation mediated by heat-shock protein Hsp104. Nature 372, 475–478.

Paul J. Muchowski and Jennifer L. Wacker, 2005. MODULATION OFNEURODEGENERATION BYMOLECULAR CHAPERONES. https://doi.org/10.1038/nrn1587

Peter, E., Candido, M., 2002. Caenorhabditis elegans: Structure, Regulation and Biology. Prog. Mol. Subcell. Biol 28, 61–78.

Pigazzini, M.L., Gallrein, C., Iburg, M., Schierle, G.K., Kirstein, J., 2020. Characterization of amyloid structures in aging C. Elegans using fluorescence lifetime imaging. Journal of Visualized Experiments 2020. https://doi.org/10.3791/61004

Pigazzini, M.L., Lawrenz, M., Margineanu, A., Kaminski Schierle, G.S., Kirstein, J., 2021. An Expanded Polyproline Domain Maintains Mutant Huntingtin Soluble in vivo and During Aging. Front Mol Neurosci 14. https://doi.org/10.3389/fnmol.2021.721749

Pohl, C., Dikic, I., 2019. Cellular quality control by the ubiquitin-proteasome system and autophagy. Science (1979) 366, 818–822.

Pras, A., Houben, B., Aprile, F.A., Seinstra, R., Gallardo, R., Janssen, L., Hogewerf, W., Gallrein, C., De Vleeschouwer, M., Mata-Cabana, A., Koopman, M., Stroo, E., Vries, M., Louise Edwards, S., Kirstein, J., Vendruscolo, M., Falsone, S.F., Rousseau, F., Schymkowitz, J., Nollen, E.A.A., 2021. The cellular modifier MOAG-4/SERF drives amyloid formation through charge complementation. EMBO J. https://doi.org/10.15252/EMBJ.2020107568

Puzzo, D., Privitera, L., Leznik, E., Fà, M., Staniszewski, A., Palmeri, A., Arancio, O., 2008. Picomolar amyloid-β positively modulates synaptic plasticity and memory in hippocampus. Journal of Neuroscience 28, 14537–14545. https://doi.org/10.1523/JNEUROSCI.2692-08.2008

Rampelt, H., Kirstein-Miles, J., Nillegoda, N.B., Chi, K., Scholz, S.R., Morimoto, R.I., Bukau, B., 2012. Metazoan Hsp70 machines use Hsp110 to power protein

disaggregation. EMBO Journal 31, 4221–4235. https://doi.org/10.1038/emboj.2012.264

Raulin, A.C., Doss, S. V., Trottier, Z.A., Ikezu, T.C., Bu, G., Liu, C.C., 2022. ApoE in Alzheimer's disease: pathophysiology and therapeutic strategies. Mol Neurodegener. https://doi.org/10.1186/s13024-022-00574-4

Ravikumar, B., Vacher, C., Berger, Z., Davies, J.E., Luo, S., Oroz, L.G., Scaravilli, F., Easton, D.F., Duden, R., O'Kane, C.J., Rubinsztein, D.C., 2004. Inhibition of mTOR induces autophagy and reduces toxicity of polyglutamine expansions in fly and mouse models of Huntington disease. Nat Genet 36, 585–595. https://doi.org/10.1038/ng1362

Raviol, H., Bukau, B., Mayer, M.P., 2006. Human and yeast Hsp110 chaperones exhibit functional differences. FEBS Lett 580, 168–174. https://doi.org/10.1016/j.febslet.2005.11.069

Ribeiro, F.C., Cozachenco, D., Heimfarth, L., Fortuna, J.T.S., de Freitas, G.B., de Sousa, J.M., Alves-Leon, S. V., Leite, R.E.P., Suemoto, C.K., Grinberg, L.T., De Felice, F.G., Lourenco, M. V., Ferreira, S.T., 2023. Synaptic proteasome is inhibited in Alzheimer's disease models and associates with memory impairment in mice. Commun Biol 6. https://doi.org/10.1038/s42003-023-05511-9

Ring, J., Tadic, J., Ristic, S., Poglitsch, M., Bergmann, M., Radic, N., Mossmann, D., Liang, Y., Maglione, M., Jerkovic, A., Hajiraissi, R., Hanke, M., Küttner, V., Wolinski, H., Zimmermann, A., Domuz Trifunović, L., Mikolasch, L., Moretti, D.N., Broeskamp, F., Westermayer, J., Abraham, C., Schauer, S., Dammbrueck, C., Hofer, S.J., Abdellatif, M., Grundmeier, G., Kroemer, G., Braun, R.J., Hansen, N., Sommer, C., Ninkovic, M., Seba, S., Rockenfeller, P., Vögtle, F., Dengjel, J., Meisinger, C., Keller, A., Sigrist, S.J., Eisenberg, T., Madeo, F., 2022. The HSP40 chaperone Ydj1 drives amyloid beta 42 toxicity. EMBO Mol Med 14. https://doi.org/10.15252/emmm.202113952

Rosati, A., Graziano, V., De Laurenzi, V., Pascale, M., Turco, M.C., 2011. BAG3: A multifaceted protein that regulates major cell pathways. Cell Death Dis. https://doi.org/10.1038/cddis.2011.24

Rosenzweig, R., Nillegoda, N.B., Mayer, M.P., Bukau, B., 2019. The Hsp70 chaperone network. Nat Rev Mol Cell Biol. https://doi.org/10.1038/s41580-019-0133-3

Ross, C.A., Poirier, M.A., 2004. Protein aggregation and neurodegenerative disease. Nat Med 10, S10. https://doi.org/10.1038/nm1066

Roux, A.E., Yuan, H., Podshivalova, K., Hendrickson, D., Kerr, R., Kenyon, C., Kelley, D., 2023. Individual cell types in C. elegans age differently and activate distinct cell-protective responses. Cell Rep 42, 112902. https://doi.org/10.1016/j.celrep.2023.112902

Schaeffer, V., Lavenir, I., Ozcelik, S., Tolnay, M., Winkler, D.T., Goedert, M., 2012. Stimulation of autophagy reduces neurodegeneration in a mouse model of human tauopathy. Brain 135, 2169–2177. https://doi.org/10.1093/brain/aws143

Schiavi, A., Cirotti, C., Gerber, L.-S., Di Lauro, G., Maglioni, S., Shibao, P.Y.T., Montresor, S., Kirstein, J., Petzsch, P., Köhrer, K., Schins, R.P.F., Wahle, T., Barilà, D., Ventura, N., 2023. Abl depletion via autophagy mediates the beneficial effects of quercetin against Alzheimer pathology across species. Cell Death Discov 9. https://doi.org/10.1038/s41420-023-01592-x

Schindelin, J., Arganda-Carreras, I., Frise, E., Kaynig, V., Longair, M., Pietzsch, T., Preibisch, S., Rueden, C., Saalfeld, S., Schmid, B., Tinevez, J.Y., White, D.J., Hartenstein, V., Eliceiri, K., Tomancak, P., Cardona, A., 2012. Fiji: An open-source platform for biological-image analysis. Nat Methods. https://doi.org/10.1038/nmeth.2019

Scior, A., Buntru, A., Arnsburg, K., Ast, A., Iburg, M., Juenemann, K., Pigazzini, M.L., Mlody, B., Puchkov, D., Priller, J., Wanker, E.E., Prigione, A., Kirstein, J., 2018. Complete suppression of Htt fibrilization and disaggregation of Htt fibrils by a trimeric chaperone complex. EMBO J 37, 282–299. https://doi.org/10.15252/embj.201797212

Seyfried, N.T., Dammer, E.B., Swarup, V., Nandakumar, D., Duong, D.M., Yin, L., Deng, Q., Nguyen, T., Hales, C.M., Wingo, T., Glass, J., Gearing, M., Thambisetty, M., Troncoso, J.C., Geschwind, D.H., Lah, J.J., Levey, A.I., 2017. A Multi-network Approach Identifies Protein-Specific Co-expression in Asymptomatic and Symptomatic Alzheimer's Disease. Cell Syst 4, 60-72.e4. https://doi.org/10.1016/j.cels.2016.11.006

Shankar, G.M., Li, S., Mehta, T.H., Garcia-Munoz, A., Shepardson, N.E., Smith, I., Brett, F.M., Farrell, M.A., Rowan, M.J., Lemere, C.A., Regan, C.M., Walsh, D.M., Sabatini, B.L., Selkoe, D.J., 2008. Amyloid-β protein dimers isolated directly from Alzheimer's brains impair synaptic plasticity and memory. Nat Med 14, 837–842. https://doi.org/10.1038/nm1782

Shannon, P., Markiel, A., Ozier, O., Baliga, N.S., Wang, J.T., Ramage, D., Amin, N., Schwikowski, B., Ideker, T., 2003. Cytoscape: A software Environment for integrated models of biomolecular interaction networks. Genome Res 13, 2498–2504. https://doi.org/10.1101/gr.1239303

Sharma, A., Shah, O.P., Sharma, L., Gulati, M., Behl, T., Khalid, A., Mohan, S., Najmi, A., Zoghebi, K., 2023. Molecular Chaperones as Therapeutic Target: Hallmark of Neurodegenerative Disorders. Mol Neurobiol. https://doi.org/10.1007/s12035-023-03846-2

Sharma, K., Schmitt, S., Bergner, C.G., Tyanova, S., Kannaiyan, N., Manrique-Hoyos, N., Kongi, K., Cantuti, L., Hanisch, U.K., Philips, M.A., Rossner, M.J., Mann, M., Simons, M., 2015. Cell type- and brain region-resolved mouse brain proteome. Nat Neurosci 18, 1819–1831. https://doi.org/10.1038/nn.4160

Shim, J., Im, S.H., Lee, J., 2003. Tissue-specific expression, heat inducibility, and biological roles of two hsp16 genes in Caenorhabditis elegans. FEBS Lett 537, 139–145. https://doi.org/10.1016/S0014-5793(03)00111-X

Shorter, J., 2011. The mammalian disaggregase machinery: Hsp110 synergizes with Hsp70 and Hsp40 to catalyze protein disaggregation and reactivation in a cell-free system. PLoS One 6. https://doi.org/10.1371/journal.pone.0026319

Song, Y., Nagy, M., Ni, W., Tyagi, N.K., Fenton, W.A., López-Giráldez, F., Overton, J.D., Horwich, A.L., Brady, S.T., 2013. Molecular chaperone Hsp110 rescues a vesicle transport defect produced by an ALS-associated mutant SOD1 protein in squid axoplasm. Proc Natl Acad Sci U S A 110, 5428–5433. https://doi.org/10.1073/pnas.1303279110

Soto, C., 2003. Unfolding the role of protein misfolding in neurodegenerative diseases. Nat Rev Neurosci 4, 49–60. https://doi.org/10.1038/nrn1007

Sperling, R.A., Aisen, P.S., Beckett, L.A., Bennett, D.A., Craft, S., Fagan, A.M., Iwatsubo, T., Jack, C.R., Kaye, J., Montine, T.J., Park, D.C., Reiman, E.M., Rowe, C.C., Siemers, E., Stern, Y., Yaffe, K., Carrillo, M.C., Thies, B., Morrison-Bogorad, M., Wagster, M. V., Phelps, C.H., 2011. Toward defining the preclinical stages of Alzheimer's disease: Recommendations from the National Institute on Aging-Alzheimer's Association workgroups on diagnostic guidelines for Alzheimer's disease. Alzheimer's and Dementia 7, 280–292. https://doi.org/10.1016/j.jalz.2011.03.003

Stricher, F., Macri, C., Ruff, M., Muller, S., 2013. HSPA8/HSC70 chaperone protein: Structure, function, and chemical targeting. Autophagy. https://doi.org/10.4161/auto.26448

Sweeney, P., Park, H., Baumann, M., Dunlop, J., Frydman, J., Kopito, R., McCampbell, A., Leblanc, G., Venkateswaran, A., Nurmi, A., Hodgson, R., 2017. Protein misfolding in neurodegenerative diseases: Implications and strategies. Transl Neurodegener 6. https://doi.org/10.1186/s40035-017-0077-5

Taguchi, Y. V, Gorenberg, E.L., Nagy, M., Thrasher, D., Fenton, W.A., Volpicelli-Daley, L., Horwich, A.L., Chandra, S.S., 2019. Hsp110 mitigates α-synuclein pathology in vivo. https://doi.org/10.1073/pnas.1903268116

Tan, J.Z.A., Gleeson, P.A., 2019. The role of membrane trafficking in the processing of amyloid precursor protein and production of amyloid peptides in Alzheimer's disease. Biochim Biophys Acta Biomembr. https://doi.org/10.1016/j.bbamem.2018.11.013

Taylor, R.C., Dillin, A., 2011. Aging as an event of proteostasis collapse. Cold Spring Harb Perspect Biol 3, 1–17. https://doi.org/10.1101/cshperspect.a004440

Tittelmeier, J., Nachman, E., Nussbaum-Krammer, C., 2020a. Molecular Chaperones: A Double-Edged Sword in Neurodegenerative Diseases. Front Aging Neurosci. https://doi.org/10.3389/fnagi.2020.581374

Tittelmeier, J., Sandhof, C.A., Ries, H.M., Druffel-Augustin, S., Mogk, A., Bukau, B., Nussbaum-Krammer, C., 2020b. The HSP110/HSP70 disaggregation system generates spreading-competent toxic α-synuclein species. EMBO J 39. https://doi.org/10.15252/embj.2019103954

Törnquist, M., Michaels, T.C.T., Sanagavarapu, K., Yang, X., Meisl, G., Cohen, S.I.A., Knowles, T.P.J., Linse, S., 2018. Secondary nucleation in amyloid formation. Chemical Communications 54, 8667–8684. https://doi.org/10.1039/c8cc02204f

Townsend, M., Shankar, G.M., Mehta, T., Walsh, D.M., Selkoe, D.J., 2006. Effects of secreted oligomers of amyloid β-protein on hippocampal synaptic plasticity: A potent role for trimers. Journal of Physiology 572, 477–492. https://doi.org/10.1113/jphysiol.2005.103754

Untergasser, A., Cutcutache, I., Koressaar, T., Ye, J., Faircloth, B.C., Remm, M., Rozen, S.G., 2012. Primer3-new capabilities and interfaces. Nucleic Acids Res 40. https://doi.org/10.1093/nar/gks596

Vilchez, D., Saez, I., Dillin, A., 2014. The role of protein clearance mechanisms in organismal ageing and age-related diseases. Nat Commun. https://doi.org/10.1038/ncomms6659

Walsh, D.M., Lomakin, A., Benedek, G.B., Condron, M.M., Teplow, D.B., 1997. Amyloid β-protein fibrillogenesis: Detection of a protofibrillar intermediate. Journal of Biological Chemistry 272, 22364–22372. https://doi.org/10.1074/jbc.272.35.22364

Wan, Y.W., Al-Ouran, R., Mangleburg, C.G., Perumal, T.M., Lee, T. V., Allison, K., Swarup, V., Funk, C.C., Gaiteri, C., Allen, M., Wang, M., Neuner, S.M., Kaczorowski, C.C., Philip, V.M., Howell, G.R., Martini-Stoica, H., Zheng, H., Mei, H., Zhong, X., Kim, J.W., Dawson, V.L., Dawson, T.M., Pao, P.C., Tsai, L.H., Haure-Mirande, J.V., Ehrlich, M.E., Chakrabarty, P., Levites, Y., Wang, X., Dammer, E.B., Srivastava, G., Mukherjee, S., Sieberts, S.K., Omberg, L., Dang, K.D., Eddy, J.A., Snyder, P., Chae, Y., Amberkar, S., Wei, W., Hide, W., Preuss, C., Ergun, A., Ebert, P.J., Airey, D.C., Mostafavi, S., Yu, L., Klein, H.U., Carter, G.W., Collier, D.A., Golde, T.E., Levey, A.I., Bennett, D.A., Estrada, K., Townsend, T.M., Zhang, B., Schadt, E., De Jager, P.L., Price, N.D., Ertekin-Taner, N., Liu, Z., Shulman, J.M., Mangravite, L.M., Logsdon, B.A., 2020. Meta-Analysis of the Alzheimer's Disease Human Brain Transcriptome and Functional Dissection in Mouse Models. Cell Rep 32. https://doi.org/10.1016/j.celrep.2020.107908

Wang, J., Farr, G.W., Hall, D.H., Li, F., Furtak, K., 2009. An ALS-Linked Mutant SOD1 Produces a LocomotorDefect Associated with Aggregation and SynapticDysfunction When Expressed in Neurons ofCaenorhabditis elegans. PLoS Genet 5, 1000350. https://doi.org/10.1371/journal.pgen.1000350

Wang, X., Su, B., Lee, H.G., Li, X., Perry, G., Smith, M.A., Zhu, X., 2009. Impaired balance of mitochondrial fission and fusion in Alzheimer's disease. Journal of Neuroscience 29, 9090–9103. https://doi.org/10.1523/JNEUROSCI.1357-09.2009

Warren, S.C., Margineanu, A., Alibhai, D., Kelly, D.J., Talbot, C., Alexandrov, Y., Munro, I., Katan, M., Dunsby, C., French, P.M.W., 2013. Rapid Global Fitting of Large Fluorescence Lifetime Imaging Microscopy Datasets. PLoS One 8. https://doi.org/10.1371/journal.pone.0070687

Webb, J.L., Ravikumar, B., Atkins, J., Skepper, J.N., Rubinsztein, D.C., 2003. α-synuclein Is Degraded by Both Autophagy and the Proteasome. Journal of Biological Chemistry 278, 25009–25013. https://doi.org/10.1074/jbc.M300227200

Wei, Y., Zhou, J., Wu, J., Huang, J., 2019. ERβ promotes Aβ degradation via the modulation of autophagy. Cell Death Dis 10. https://doi.org/10.1038/s41419-019-1786-8

Wentink, A.S., Nillegoda, N.B., Feufel, J., Ubartaitė, G., Schneider, C.P., De Los Rios, P., Hennig, J., Barducci, A., Bukau, B., 2020. Molecular dissection of amyloid disaggregation by human HSP70. Nature 587, 483–488. https://doi.org/10.1038/s41586-020-2904-6

Winklhofer, K.F., Tatzelt, J., Haass, C., 2008. The two faces of protein misfolding: Gain- and loss-of-function in neurodegenerative diseases. EMBO Journal. https://doi.org/10.1038/sj.emboj.7601930

Wirths, O., Multhaup, G., Czech, C., Ronique Blanchard, V.Â., Moussaoui, S., Nter Tremp, G.È., Pradier, L., Beyreuther, K., Bayer, Thomas A, Bayer, T A, 2001. Intraneuronal Ab accumulation precedes plaque formation in b-amyloid precursor protein and presenilin-1 double-transgenic mice. Neurosci Lett 18, 76–82.

World Alzheimer Report 2023 Reducing dementia risk: never too early, never too late, n.d.

Wu, Y., Wu, Z., Butko, P., Christen, Y., Lambert, M.P., Klein, W.L., Link, C.D., Luo, Y., 2006. Amyloid-β-induced pathological behaviors are suppressed by Ginkgo biloba extract EGB 761 and ginkgolides in transgenic Caenorhabditis elegans. Journal of Neuroscience 26, 13102–13113. https://doi.org/10.1523/JNEUROSCI.3448-06.2006

Wyatt, A.R., Yerbury, J.J., Ecroyd, H., Wilson, M.R., 2013. Extracellular chaperones and proteostasis. Annu Rev Biochem. https://doi.org/10.1146/annurev-biochem-072711-163904

Xu, X., Sarbeng, E.B., Vorvis, C., Kumar, D.P., Zhou, L., Liu, Q., 2012. Unique peptide substrate binding properties of 110-kDa heat-shock protein (Hsp110) determine its distinct chaperone activity. Journal of Biological Chemistry 287, 5661–5672. https://doi.org/10.1074/jbc.M111.275057

Yakubu, U.M., Morano, K.A., 2021. Suppression of aggregate and amyloid formation by a novel intrinsically disordered region in metazoan Hsp110 chaperones. Journal of Biological Chemistry 296. https://doi.org/10.1016/j.jbc.2021.100567

Yakubu, U.M., Morano, K.A., 2018. Roles of the nucleotide exchange factor and chaperone Hsp110 in cellular proteostasis and diseases of protein misfolding. Biol Chem. https://doi.org/10.1515/hsz-2018-0209

Yamanaka, Yada, Imaki, Koga, Ohshima, Nakayama, 2002. Multiple Skp1-Related Proteins in Caenorhabditis elegans: Diverse Patterns of Interaction with Cullins and F-Box Proteins. Current Biology 12, 267–275.

Yang, Y., Arseni, D., Zhang, W., Huang, M., Lövestam, S., Schweighauser, M., Kotecha, A., Murzin, A.G., Peak-Chew, S.Y., Macdonald, J., Lavenir, I., Garringer, H.J., Gelpi, E., Newell, K.L., Kovacs, G.G., Vidal, R., Ghetti, B., Ryskeldi-Falcon, B., W Scheres, S.H., Goedert, M., 2022. Cryo-EM structures of amyloid-b 42 filaments from human brains. Science (1979) 375, 167–172. https://doi.org/doi: 10.1126/science.abm7285

Yasuda, K., Nakai, A., Hatayama, T., Nagata, K., 1995. Cloning and expression of murine high molecular mass heat shock proteins, HSP105. Journal of Biological Chemistry 270, 29718–29723. https://doi.org/10.1074/jbc.270.50.29718

Yasumoto, T., Takamura, Y., Tsuji, M., Watanabe-Nakayama, T., Imamura, K., Inoue, H., Nakamura, S., Inoue, T., Kimura, A., Yano, S., Nishijo, H., Kiuchi, Y., Teplow, D.B., Ono, K., 2019. High molecular weight amyloid β1-42 oligomers induce neurotoxicity via plasma membrane damage. FASEB Journal 33, 9220–9234. https://doi.org/10.1096/fj.201900604R

Yu, L., Edalji, R., Harlan, J.E., Holzman, T.F., Lopez, A.P., Labkovsky, B., Hillen, H., Barghorn, S., Ebert, U., Richardson, P.L., Miesbauer, L., Solomon, L., Bartley, D., Walter, K., Johnson, R.W., Hajduk, P.J., Olejniczak, E.T., 2009. Structural characterization of a soluble amyloid β-peptide oligomer. Biochemistry 48, 1870–1877. https://doi.org/10.1021/bi802046n

Zecha, J., Gabriel, W., Spallek, R., Chang, Y.C., Mergner, J., Wilhelm, M., Bassermann, F., Kuster, B., 2022. Linking post-translational modifications and protein turnover by site-resolved protein turnover profiling. Nat Commun 13. https://doi.org/10.1038/s41467-021-27639-0

Zhang, Y., Chen, H., Li, R., Sterling, K., Song, W., 2023. Amyloid β-based therapy for Alzheimer's disease: challenges, successes and future. Signal Transduct Target Ther. https://doi.org/10.1038/s41392-023-01484-7

8 Supplementary figures

Figure S. 1: Whole body confocal images of the *C. elegans* nAβ, *n hsp-110 I*, nmScarlet and the crosses

a) Confocal fluorescent images of the parental strains (nAβ, *n hsp-110 I*) and the cross (nAβ x *n hsp-110 I*). The whole body of day 4 old animals are depicted as merge, Aβ fluorescence (magenta) and HSP-110 fluorescence (cyan). Images are 100-fold magnified (scale bar is 200 µm). The white dashed line shows the outline of the nematode. Close-up images are depicted for nAβ and nAβ x *n hsp-110 I* on the right of the respective Aβ fluorescence images for better visualisation (scale bar is 200 µm).

b) Confocal fluorescent images of the parental control strain (nmScarlet) and the cross (nmScarlet x *n hsp-110 I*). The whole body of day 4 old animals are depicted as merge, mScarlet fluorescence (magenta), and HSP-110 fluorescence (cyan). Images are 100-fold magnified (scale bar is 200 µm). The white dashed line shows the outline of the nematode.

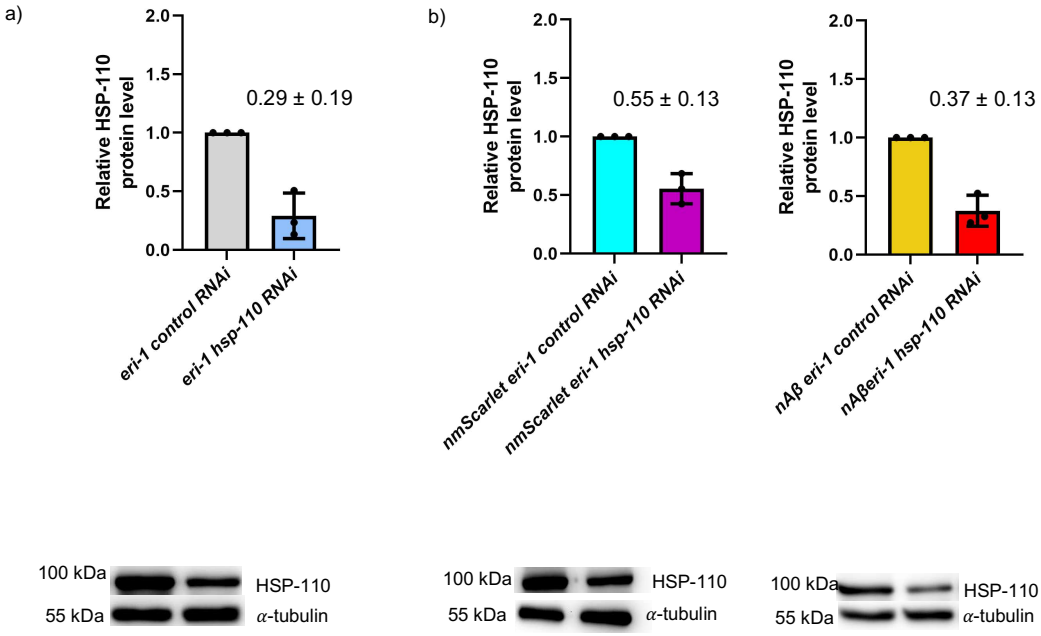

Figure S. 2: Validation of the knockdown efficiency of *hsp-110* by RNAi.

a) Quantification of HSP-110 in *eri-1* nematodes after systemic *hsp-110* depletion by RNAi. The strain was fed for two generations with *E. coli* HT115 (DE3) carrying the L4440 empty vector (also control RNAi) or the vector with *hsp-110* (*hsp-110* RNAi). Three biological replicates of day 4 old animals were tested by blotting the total lysates and quantifying HSP-110 using rabbit anti-nematode HSP-110 antibody. Signal intensities were normalized to α-tubulin. The scatter dot plot shows the relative abundance of HSP-110 in *eri-1* control RNAi animals (grey) and in *eri-1 hsp-110* RNAi animals (light

blue). Data are displayed as mean fluorescence intensity ± SD. Representative western blots are shown on the bottom.

b) Quantification of HSP-110 in nmScarlet *eri-1* and nAβ *eri-1* nematodes after systemic *hsp-110* depletion by RNAi as in a). Scatter dot plots show the relative abundance of HSP-110 in *hsp-110* RNAi condition relative to control RNAi animals. On the left, quantified HSP-110 levels are shown for nmScarlet *eri-1* control RNAi (cyan) and nScarlet *eri-1 hsp-110* RNAi (purple). On the right, quantified HSP-110 levels are shown for nAβ *eri-1* control RNAi animals (yellow) and nAβ *eri-1 hsp-110* RNAi animals (red). Data are displayed as mean fluorescence intensity ± SD. Representative western blots are shown on the bottom.

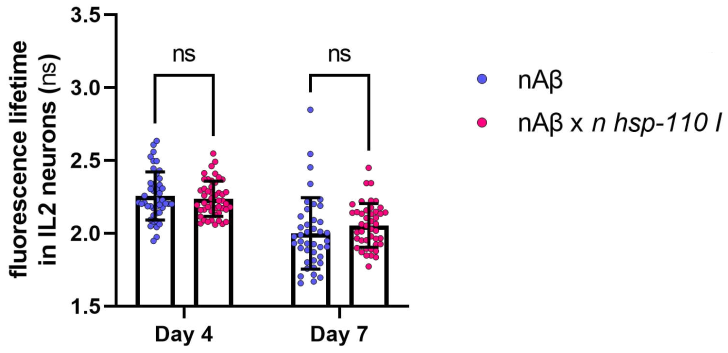

Figure S. 3 Pan-neuronal overexpression of *hsp-110* does not alter Aβ$_{1-42}$ aggregation in the IL2 neurons

Scatter dot plot of the average fluorescence lifetime in nanoseconds (ns) of mScarlet in nAβ and nAβ x *n hsp-110 I* nematodes in the IL2 neurons. Data display the average fluorescence lifetime ± SD for day 4 (left side) and day 7 old (right side) nAβ (blue) and nAβ x *n hsp-110 I* (magenta) animals. Every dot represents the average fluorescence lifetime of mScarlet of nAβ and nAβ x *n hsp-110 I* in the IL2 neurons of one single nematode. Three independent cohorts of 13-20 animals were analyzed. Significance was tested by two-way ANOVA + Bonferroni post hoc test (ns = $p > 0.05$).

9 List of abbreviations

°C	Degree Celsius
AD	Alzheimer's Disease
ADP	Adenosine diphosphate
AICD	APP intracellular domain
ALS	Amyotrophic lateral sclerosis
ANOVA	Analysis of variance
APOE	Apolipoprotein E
APP	Amyloid precursor protein
APS	Ammoniumperoxodisulfat
AS	Acidic sequence
a-syn	a-synuclein
ATP	Adenosine triphosphate
au	Arbitrary units
Aβ	Amyloid beta
BACE1	β-secreatase 1
BAG	Bcl-2 associated anthanogene
BP	Biological process
bp	Base pairs
BSA	Bovine serum albumin
C. elegans	*Caenorhabditis elegans*
CGC	Caenorhabditis genetic center
CS	Citrate synthase
C-terminal	Carboxy-terminal
DEG	Differentially expressed gene
DEP	Differentially expressed protein
DMSO	Dimethyl sulfoxide
DNA	Deoxyribonucleic acid
DNase	Deoxyribonuclease
dNTP	Deoxynucleotide triphosphate
DTT	Dithiothreitol
E. coli	*Escherichia coli*

ECL	Enhanced chemiluminescence
EDTA	Ethylenediaminetetraacetic acid
ER	Endoplasmic reticulum
Ex	Extra-chromosomal array
F0, F1, F2	Parent generation, first progeny generation, second progeny generation
FDR	False discovery rate
FLIM	Fluorescence lifetime imaging microscopy
For	Forward
g (µg, mg)	gram (microgram, milligram) or Gravitational force equivalent
GFP	Green fluorescent protein
GO	Gene ontology
h	Hour
HD	Hintington´s disease
hsp /HSP	Heat shock protein, gene: *hsp*, protein: HSP
HTT	Huntingtin
Hz	Hertz
IDR	Intrinsically disordered region
IL2	Inner labial sensilla 2 (set of six ciliated neurons)
IPTG	Isopropyl b-D-1-thiogalactopyranoside
IRES	Internal ribosome entry site
IRF	Instrument response function
Is	Integrated strain
J	Joule
JDP	J-domain protein

kb	Kilobase
KD	Knockdown
kDa	Kilodalton
KO	Knockout
l, (µl, ml)	Liter (microliter, milliliter)
L1 – L4	Nematode larval stages 1 to 4
LB	Luria broth
LSM	Laser scanning microscope
m	Muscular
M (pM, nM, µM, mM)	Molar (picomolar, nanomolar, micromolar, millimolar)
mRNA	Messenger RNA
MS	Mass spectrometry
myo-3	Myosin heavy chain structural gene
n	Neuronal
NBD	Nucleotide binding domain
NCBI	National Center for Biotechnology Information
NEB	New England Biolabs
NEF	Nucleotide exchange factor
NFTs	Neurofibrillary tangles
NGM	Nematode growth media
ns	Nanoseconds or non significant
N-terminal	Amino-terminal
PCR	Polymerase chain reaction
PD	Parkinson´s Disease
PE	Phosphatidylethanolamine
PN	Proteostasis network

PPI	Protein-protein interaction
PSEN	Presenilin
PVDF	Polyvinylidene fluoride
Rev	Reverse
rgef-1	Rap Guanine nucleotide Exchange Factor homolog (gene)
RNA	Ribonucleic acid
RNAi	RNA interference
RNase	Ribonuclease
ROI	Region of interest
ROS	Reactive oxygen species
rpm	Revolutions per minute
RT	Room temperature (approx. 20°C)
s / sec	Second
sAPPα	Soluble APP α protein
sAPPβ	Soluble APP beta protein
SBD	Substrate binding domain
SD	Standard deviation
SDS	Sodium dodecyl sulphate
SDS-PAGE	SDS-polyacrylamide gel electrophoresis
sHSP	Small heat shock protein
SOD1	Superoxide dismutase 1
Tau	Tau protein
tau or τ	Fluorescence lifetime
TBE	Tris-borate-EDTA
TBS-(T)	Tris-buffered saline (with Tween 20)
TEMED	Tetramethylethylenediamine
Tm	Melting temperature

Tris	Tris(hydroxymethyl)aminomethane
UPS	Ubiquitin-Proteasome System
UTR	Untranslated region
UV	Ultraviolet
V	Volt
v/v	Volume per volume
w/v	Weight per volume
WB	Western blot
wt	Wildtype

10 List of figures

Introduction

Results

Supplementary figures

11 List of tables

Results

12 Declaration

Universität Bremen | Fachbereich 02 | Postfach 33 04 40, 28334 Bremen

Universität Bremen
Fachbereich 2
Prüfungsamt Chemie
z. Hd. Frau Frauke Ernst
Leobener Straße

28359 Bremen
Deutschland

Prüfungsamt
Chemie

Frauke Ernst
Geschäftsstelle
Fachbereich 02
Leobener Str. / NW2
D-28359 Bremen

Verwaltungspavillon 06
Tel. 0421 218-62802
Fax 0421 218-9862802
frauke.ernst@uni-bremen.de
www.fb2.uni-bremen.de

Versicherung an Eides Statt

Name, Vorname	Montresor, Sabrina
Matrikel-Nr.	
Straße	
Ort, PLZ	Bremen

Ich, Sabrina Montresor

versichere an Eides Statt durch meine Unterschrift, dass ich die vorstehende Arbeit selbständig und ohne fremde Hilfe angefertigt und alle Stellen, die ich wörtlich dem Sinne nach aus Veröffentlichungen entnommen habe, als solche kenntlich gemacht habe, mich auch keiner anderen als der angegebenen Literatur oder sonstiger Hilfsmittel bedient habe.
Ich versichere an Eides Statt, dass ich die vorgenannten Angaben nach bestem Wissen und Gewissen gemacht habe und dass die Angaben der Wahrheit entsprechen und ich nichts verschwiegen habe.
Die Strafbarkeit einer falschen eidesstattlichen Versicherung ist mir bekannt, namentlich die Strafandrohung gemäß § 156 StGB bis zu drei Jahren Freiheitsstrafe oder Geldstrafe bei vorsätzlicher Begehung der Tat bzw. gemäß § 161 Abs. 1 StGB bis zu einem Jahr Freiheitsstrafe oder Geldstrafe bei fahrlässiger Begehung.

Ort, Datum / Unterschrift

13 Acknowledgement

Firstly, I would like to express my deepest gratitude to my supervisor, Prof. Dr. Janine Kirstein, for her encouragement and her invaluable guidance throughout the PhD journey.

I am grateful to Prof. Dr. Olivia Masseck for accepting to be the second reviewer of this thesis.

Thanks to the Sawarkar lab and the Savitski lab for their collaboration on the transcriptomic and proteomic analyses. Special thanks are extended to Mira Sleiman, Sudarson Baskaran, Govinda Adhikari, Dr. Maria Lucia Pigazzini and all the students for their significant contributions to the HSP110 work. I am grateful to Dr. Annette Peter for her guidance in microscopy, for the insightful discussions and for her support throughout the research process. Your kind words have been a source of motivation.

I am thankful to Merve Özel and Dr. Yasmin Richter, who have been by my side since day one in this journey. Thank you for all your support, I consider myself fortunate to have shared this experience with you. I would also like to thank Franziska Hirsch for the engaging worm discussions, it was a pleasure to share the office with you. Special thanks are due to Dr. Priscila Yumi Tanaka Shibao, Verena Fischer, Regina Nahrstedt as well as former and current lab members for always lending a helping hand.

My biggest thanks to my family, who have been my rock, always by my side despite the distance. Thank you for your constant support!

Lastly, I would like to thank all my friends for being there for me in good and bad times. Thank you for the smiles, the fun and the light you have brought into my life.